Spring 2019

FAULT MAPPING IN 3D SEISMIC REFLECTION DATA USING SEISMIC ATTRIBUTES AND VELOCITY ANISOTROPY: EXAMPLE FROM WEST VIRGINIA

Megan Valdez

FAULT MAPPING IN 3D SEISMIC REFLECTION DATA USING SEISMIC ATTRIBUTES AND VELOCITY ANISOTROPY: EXAMPLE FROM WEST VIRGINIA

by

Megan Valdez

A thesis submitted in partial fulfillment of the
requirements for the degree of

Masters of Science in Geoscience:
Geophysical Engineering Option

Montana Tech

2019

Abstract

Fracture characterization is highly important in the oil and gas industry. Knowing the location of fractures allows for the assessment of reservoir quality, aids in well placement and planning, and helps identify locations of possible traps. Fracture locations can be determined using seismic data for attribute calculations and anisotropy analysis. Attribute calculations, such as coherence and curvature, identify subtle changes in the dataset that conventional seismic data interpretation might overlook. Anisotropy analysis looks at directionally dependent variations in the wave propagation velocity. Fractures slow the propagation velocity of a wave if the fractures are perpendicular to the wave direction. A combination of attribute calculations, and anisotropy data can predict locations of faults within a region.

The study region for this thesis project is within Greenbrier and Nicholas Counties, West Virginia. A 36 fold, 128 square miles (333 km^2) seismic survey, conducted in 2011, spans two lease regions, the Mead West Vaco, and the Plum Creek South Fork. Ten wells are within the two lease regions, drilled prior to the completion of the seismic survey. Of the 10 wells, a core analysis focusing on the Marcellus Formation utilized data from four wells. In addition, a microseismic analysis used data from three wells.

The Marcellus Formation is the target of the seismic study and the wells. The Marcellus is a middle Devonian, black, shale interbedded with limestone. The formation spans approximately 95,000 mi^2 (246,048 km^2) in the northeastern United States with thicknesses varying from 50-200 ft (15-61 m). Deposition of the Marcellus occurred in a deep-water, oxygen-deprived environment, which resulted in the accumulation of hydrocarbons. The interbedding of limestone with shale, within the formation, created many traps for hydrocarbons resulting in the reservoirs today. The low permeability of the formation lends to the use of hydraulic fracturing for well completion making the knowledge of the fault systems crucial.

Attribute calculations including semblance, dip steered semblance, and curvature gave information of the potential locations of fractures. Azimuthal anisotropy data mapped at various depths showed the correlation of the velocities with the potential fault locations taken from the attribute results. Results of the mean and dip curvature calculation provided the clearest evidence of faults.

Azimuthal anisotropy is another useful tool in fault characterization. Fractures, when perpendicular to wave direction, slow the rate of propagation of a seismic wave. Methods such as amplitude versus azimuth (AVAz) and velocity variations with azimuth (VVAz) use amplitude and velocity as a function of azimuth. However, migration of data removes the needed azimuthal information. Offset vector tiling (OVT) processing is a solution to the migration problem. OVT groups seismic data by common offsets and common azimuth, which allows the saving of azimuthal information in the migration process.

Attributes, such as dip curvature and mean curvature provide insight to fault locations; however, combining OVT anisotropy data, horizontal slice attribute calculations, and horizon attribute calculations improves the confidence in fault locations. The results of this study show that azimuthal anisotropy maps are in agreement with the major fault locations determined initially from the attribute calculations. OVT anisotropy data shows the fault orientations across the region, with an overall trend of faults in the NE-SW direction.

Keywords: Marcellus, Anisotropy, Attributes, Curvature, Semblance, Coherency

Dedication

I would like to say a huge thank you to my parents, my sisters, and all my family for supporting me.

Acknowledgements

I thank Bluescape Resources for providing the data and Seisware Inc. for the use of their software for this research. I also thank the members of my committee Marvin Speece, Scott Rosenthal, and Xiaobing Zhou.

Table of Contents

List of Tables

List of Figures

List of Symbols, Abbreviations, and Nomenclature

^{o}	Degree
α	Compressional-wave Velocity
β	Shear-wave Vertical velocity
ρ	Bulk density
2D	Two Dimensional
3D	Three Dimensional
AVA	Amplitude Variation with Angle
AVAz	Amplitude Variation with Azimuth
AVO	Amplitude Variation with Offset
CDP	Common Depth Point
CMP	Common Mid-point
COV	Common Offset Vector
Datum	2000 ft
ft	Feet
GRI	Gas Research Institute
HTI	Horizontal Transverse Isotropy
km	Kilometer
m	Meter
mi	Mile
ms	Millisecond
MWV	Mead West Vaco
NMO	Normal Moveout
OVT	Offset Vector Tiling
OXY	Occidental Petroleum
%	Percent
PCSF	Plum Creek South Fork
PSTM	Pre-stack Time Migration
PSDM	Post-stack Depth Migration
P-wave	Compressional Wave
QC	Quality Control
RMS	Root Mean Square
s	Second
S-wave	Shear Wave
TD	Total Depth
TOC	Total Organic Carbon
TVD	True Vertical Depth
V_{FAST}	Fast Velocity for HTI
V_P	P-wave Velocity
V_S	S-wave Velocity
V_{SLOW}	Slow Velocity for HTI
VTI	Vertical Transverse Isotropy
VVAz	Velocity Variation with Azimuth

1. Introduction

In the ever-growing oil and gas industry, the need for knowledge of fault and fracture systems is essential. Being able to determine the location of fractures, especially those subtle enough to be missed in traditional seismic, is particularly important because it aids in reservoir characterization, well planning, and well placement. The term fracture refers to a number of geologic discontinuities such as faults, and joints, which may or may not present any displacement (Chopra, 2011). In addition, assessing the quality of a reservoir is possible with the knowledge of regional fault systems

Seismic attributes are components of seismic data and are useful in determining fracture/fault locations. The first attribute calculations were single trace instantaneous attributes introduced in 1979 (Taner et al., 1979). In 1996, attributes expanded to 2D and 3D surveys (Barnes, 1996). Coherency-type attributes were introduced in 1995 as a cross correlation between neighboring traces (Bahorich and Farmer, 1995), and then in 1998 a multi-trace semblance based coherency algorithm was introduced (Marfurt et al., 1998). A class of surface related attributes, known as curvature attributes, enhance subtle features of conventional data were introduced in 2001 (Roberts, 2001).

Attributes calculations fall into two main classes, physical attributes and geometric attributes. Geometric attributes respond to changes in both subsurface structure and stratigraphy allowing for identification of discontinuities. Dip magnitude, dip azimuth, and similarity are some of the attributes calculations that fall within the class of geometric attributes. Another class of attributes commonly used for fracture detection is the curvature attributes. Curvature attributes bring out subtle features sometimes missed by other geometric attributes, allowing for the location of less distinct faults (Jones and Roden, 2012).

Another method of fault and fracture characterization is the use of azimuthal anisotropy. Subsurface fractures create anisotropy because the mechanical discontinuities with preferred orientation change the wave propagation velocity (Pyrak-Nolte, 2007). Anisotropy can be an effective tool in the identification of lithology, fractures, cracks, and pore spaces, as well as identifying the possible presence of gas in shales (Gargouri, 2012). Fractures introduce anisotropy that manifests as azimuthal variations. Methods like amplitude versus azimuth (AVAz) can characterize smaller, local fracture distributions and orientations (Abousetta et al., 2106). Another method is the velocity variations with azimuth (VVAz), similar to AVAz, but can handle more sparse data sets (Wang et al., 2007), and uses the base of the target instead of the top.

Traditional methods of processing seismic data remove azimuthal information required by both AVAz and VVAz. Offset vector tiling (OVT) is a method of sectoring data into sub-volumes of common azimuth and offset (Vermeer, 2002). OVT's method of sectoring data preserves the azimuth data that conventional seismic processing removes (Al Dulaijan, 2017). Many 3D land surveys fit the criteria of full coverage, orthogonal, wide azimuth, and large offset needed for OVT. In addition to the benefit of preserving azimuth information, OVT provides improved illuminations, image quality, and multiple elimination (Yue et al., 2016).

For this study, I completed attribute calculations on seismic data from West Virginia targeting the Marcellus Formation. Attribute calculations include semblance, dip-steered semblance, median, trace mix, trace mix triangulation, dip azimuth, mean curvature, Gaussian curvature, maximum curvature, minimum curvature, most positive/negative curvature, dip curvature, and strike curvature. In addition, I compared OVT azimuthal anisotropy data to attribute methods for fracture orientation.

2. Background

2.1. Geology

2.1.1. Geological History

The geological history of the West Virginia begins with the deposition of lava in the eastern region of the state 1,100 to 800 million years ago. After the deposition of lava, a trough formed in the eastern region of the United States, which allowed for a seaway to form, and the beginning of deposition of sediments. As time progressed, the sea continued to transgress, eventually covering a majority of the state's region in the Cambrian period (Cardwell, 1977). Throughout the Cambrian and into the Ordovician period marine deposition occurred. At the conclusion of the Ordovician the Taconic Orogeny occurred. The Taconic formed high mountains in the eastern region of West Virginia creating a new source for sediments for the succeeding periods (Allaby, 2008). Deposition of clastic and carbonate sediments occurred in a mixture of marine and non-marine environments; however, the deposition of clastic sediments was predominately in the more eastern regions.

The Acadian Orogeny marked the beginning of the Devonian period in the region. The uplift in the northeast areas of West Virginia characterizes the Acadian Orogeny. The Acadian Orogeny was the result of oblique convergence along a strike-slip fault zone (Otto, 2013). At this time, a long, narrow seaway connected to the Atlantic covered most of the state. As time progressed, shorelines retreated, and the dominating seaway became shallower. Deposition of dark, marine shales with intermittent siltstones and sandstone layers marks the middle of the Devonian period. The deposition of the Marcellus Formation occurs at this point in the period in the Appalachian foreland basin (Stevenson, 2015). The Marcellus is a fissile shale that ranges from 200 to 500 ft (60 to 152 m) in thickness, and has a low carbon content (Enomoto et al.,

2011). The shales formed in the southern regions became highly fractured as time progressed, creating ideal conditions for oil and gas reservoirs.

As the Devonian period ended, a sea covered much of West Virginia a final time. The predominately limestone, Greenbrier Formation was deposited in the southern areas of West Virginia. The deposition of the Greenbrier was the last significant marine deposit in the state, being the thickest and most widespread (Englund, 1985). As the end of the Mississippian approached, the sea retreated from the region, and by the end of the period, West Virginia became almost entirely land surface that was subject to erosion. At the end of the Mississippian, deposition of the Mauch Chunk Group took place. The Mauch Chunk consists mainly of clastic sedimentary rocks, mainly conglomerates with some sandstones and siltstones (Pazzaglia, 2006). The Mauch Chunk also contains the gas producing Ravencliff Formation.

At the beginning of the Pennsylvania period, the sea regressed. The soft sediments from the Devonian eroded into channels, creating unconformities in the stratigraphic record. Subsidence of the region began, but the deposition of sediments from the Appalachians occurred at a similar rate causing the creation of low swampy regions near sea level. The extensive carboniferous swamp forests that now dominated the region created ideal conditions for peat deposits that, after years of pressure and heat, would turn to coal deposits. As deposition of peat occurred, intermittent layers of sandstones acted as reservoirs for oil and gas production.

The Appalachian Orogeny occurred 270 to 225 million years ago, marking the start of the Permian. In the eastern part of the state, the orogeny caused extensive folding and faulting. The sandstones, siltstones, and shales created in this period are very similar to those created in the Pennsylvanian suggesting a similar environment. Fossils found in formations from this period

appear to be fresh-water in origin. However, the presence of some brackish water fossils indicate the lowest regions of the basin had subsided to below sea level (Cardwell, 1977).

The sea over the Appalachian region had regressed at the beginning of the Mesozoic. The Mesozoic marked the end of an almost continuous era of marine deposition that had begun more than 500 million years prior. The rock formations in the Mesozoic era consist of igneous intrusions and dikes of diabase.

Notable igneous activity began in the eastern regions of West Virginia in the Cenozoic era, and igneous bodies intruded the Paleozoic sediments. The only sediments from this era were a few lake deposits and alluvial deposits of gravel, sand, and clay along existing streams. The glaciers prominent in the Cenozoic did not extend into the state, but were the cause of changes in drainage patterns that lead to the deposition of important lake deposits (Cardwell, 1977). Figure 1 shows a geological map of West Virginia.

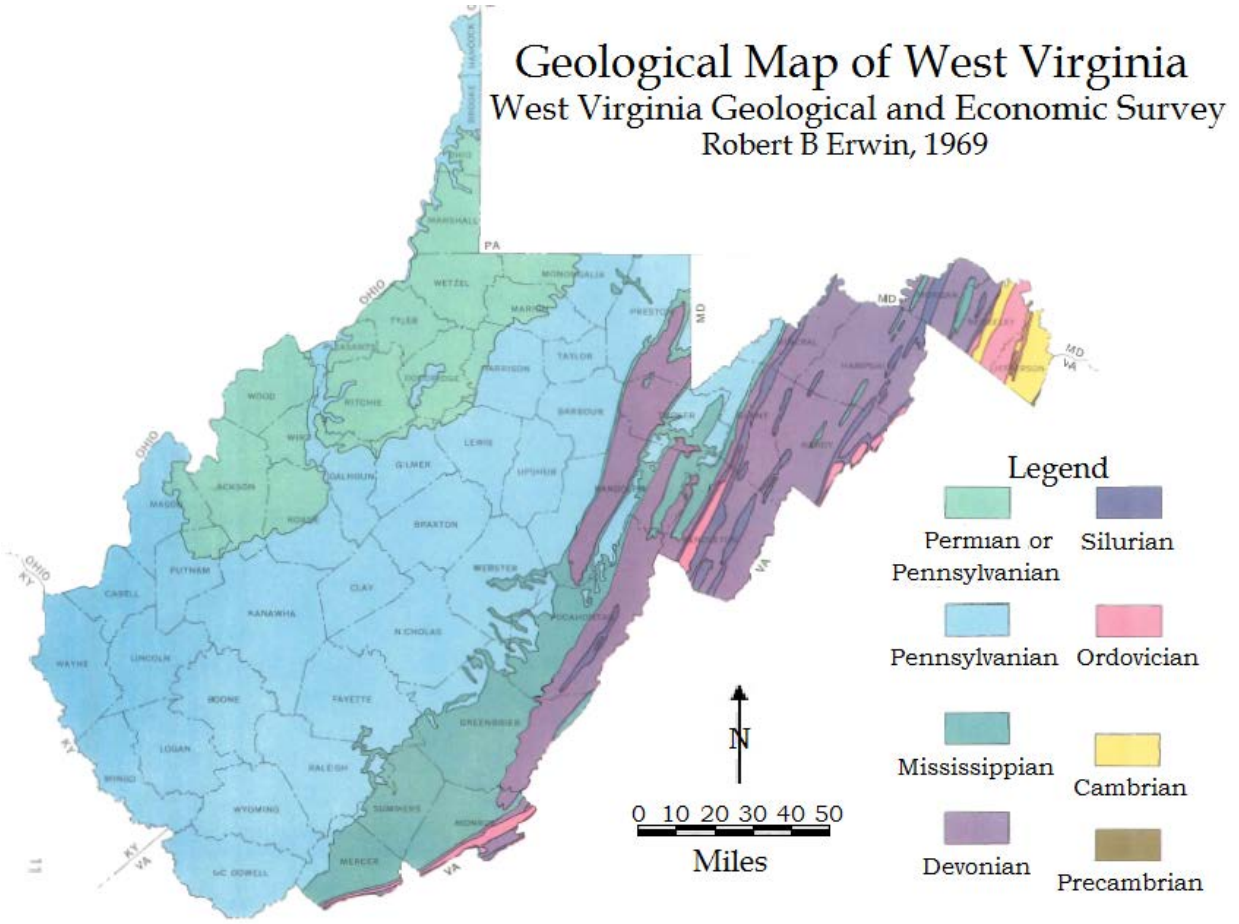

Figure 1: Geological map of West Virginia adapted from Cardwell, 1977.

The multiple orogeny's that affected the area created structural complexity. Basin compression because of the Alleghenian orogeny caused the strikes of the major folds and faults in the region to be northeast to southwest. Thrust faults are common in the region due to the compressional loading environment combined with the vertical variance in rigidity lead to the formation of duplex structures (Shin, 2016). A generalized map of faulting and folding within the Appalachian region is in Figure 2.

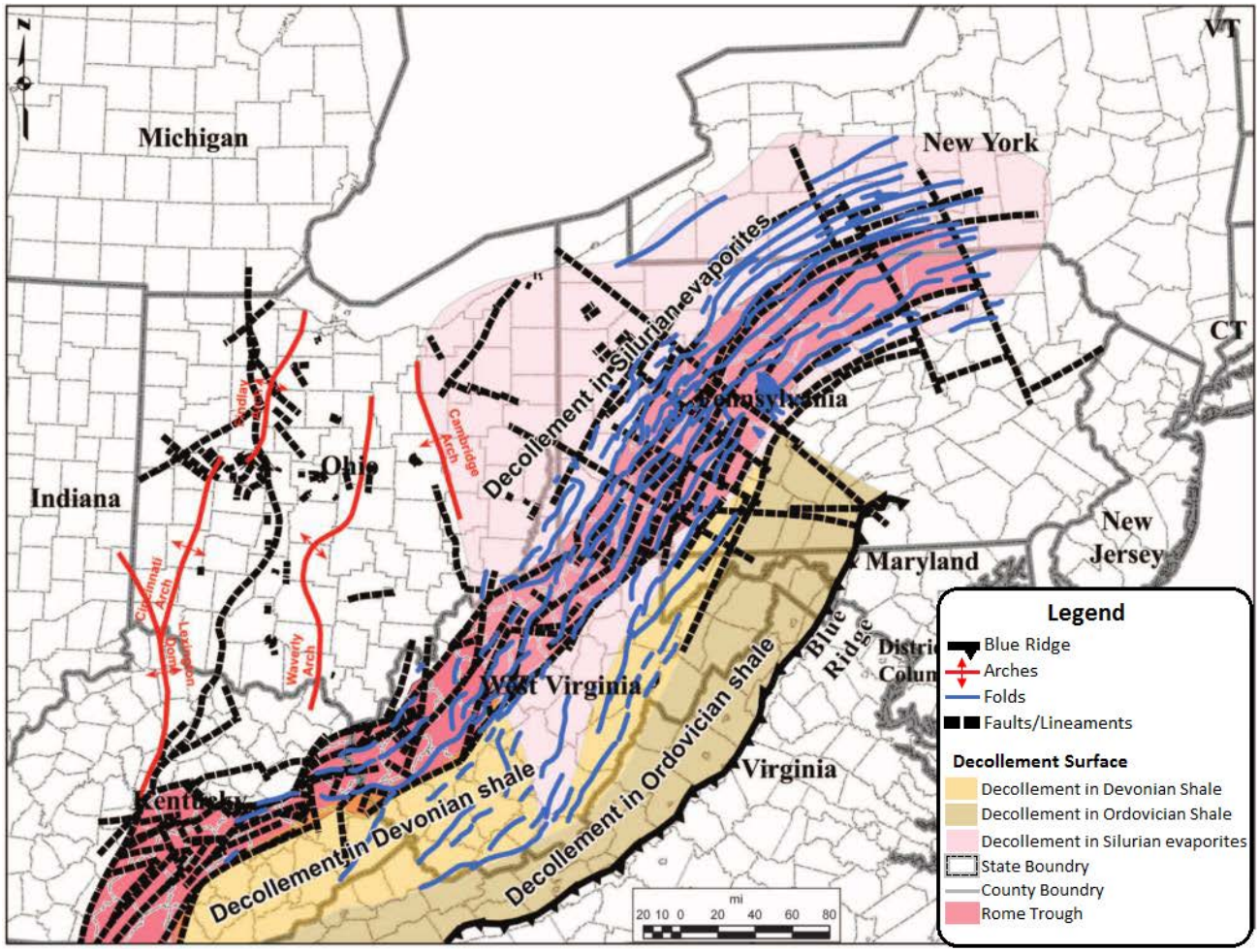

Figure 2: Map of general faulting and folding trends in the Marcellus Shale where blue lines represent folds, and dashed black line indicate faults. The regional trend of folds and faults is NE-SW (Zagorski et al., 2012).

2.1.1. Marcellus Shale

The Marcellus Formation (or the Marcellus Shale) is the primary target of this research. The Marcellus Formation is a middle Devonian, organic-rich, black shale interbedded with limestone. The interbedding of shale with limestone within the formation is the result of an oscillating sea level at the time of deposition. The Marcellus extends from New York down to Tennessee and from Ohio east to New York (Figure 3). The boundaries of the formation are limited in extent due to tectonically driven sea level variations (Inks et al., 2015). The Marcellus Formation spans approximately 95,000 square miles (246,048 km^2) (Figure 3), with depths

ranging from 4,000 to 8,500 ft (1219 to 2591 m). The thickness of the formation ranges from 50 to 200 ft (15 to 61 m) with an average thickness of 135 ft (41 m) (Osholake et al., 2011). Transitional strike-slip and reverse faulting characterize the stress state of the Marcellus Formation (Alalli and Zoback, 2018).

Figure 3: Extent of the Marcellus Formation, shown in pink, in Northeastern United States. The Marcellus Formation spans from New York south to Tennessee, and from Ohio east to New York (adapted from Soeder et al., 2014).

The Marcellus is comprised of two parts, the Oatka Creek Shale (upper) and the Union Springs (lower). The Cherry Valley Limestone divides the upper and lower portions of the Marcellus. The total organic carbon (TOC) ranges from 3-12% within the formation, with an

average of 6-8% within the lower Marcellus (Alalli and Zoback, 2018). Stratigraphically, the formation is the oldest of the Hamilton Group shown in Figure 4.

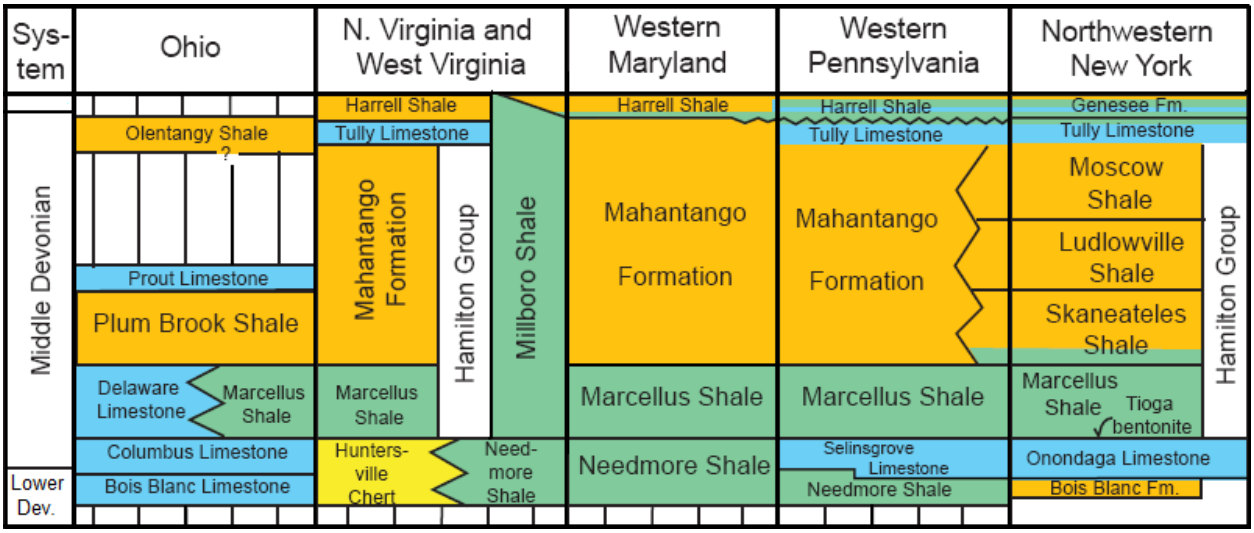

Figure 4: Partial stratigraphic column showing the Middle Devonian Marcellus Shale, which is the oldest of the Hamilton group (adapted from Milici and Swezey, 2006).

Deposition of the Marcellus occurred in a deep-water, oxygen-free environment, which aided in the accrual of hydrocarbons without breakdown (Koesoemadinata et al., 2011). The rapid filling of the depositional basin prevented seawater from escaping the fine grain matrix of the formation. With the organic content, and the continuous temperature and pressure increase, hydrocarbons built up. The interbedded limestone acts as a seal within the Marcellus allowing for the trapping of natural gas (Gargouri, 2012).

2.2. Research Description

2.2.1. Seismic Study

In 2011, Bluescape Resources/OXY contracted a seismic survey targeting the lower Marcellus Shale. The prospect, named Mountaineer, was located in Greenbrier and Nicholas counties, West Virginia. Aram Systems Ltd. completed the survey spanning 128.5 sq. mi (333 km^2), with 36 fold. The grid size used was 82.5 ft (25 m) inline by 165 ft (50 m) crossline.

Parameters of the sources and receivers used in the study are in Table I. The prospect spans two lease regions, the Mead West Vaco (MWV) and the Plum Creek South Fork (PCSF). Ten wells, drilled prior to the study, are located within the two lease regions. Figure 5 shows an outline of the seismic survey, as well as the locations of the wells.

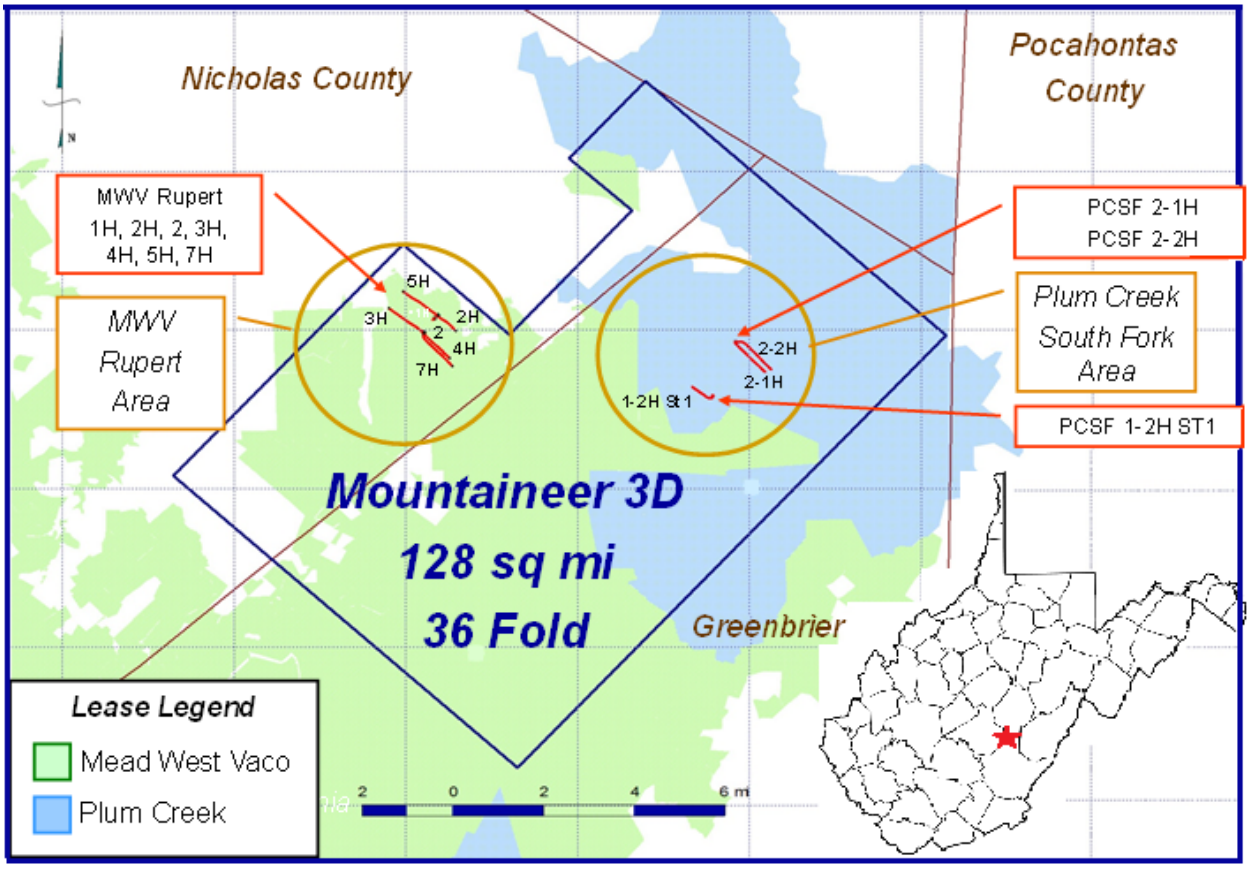

Figure 5: The Mountaineer prospect was the target of a seismic study completed in 2011 for Bluescape Resources/OXY. The seismic study spans 128.5 square miles (333 km^2). The acquisition grid is 82.5 by 165 ft (25 by 50 m). Two lease regions make up the study area. The area contains 10 wells, drilled prior to the seismic study. Wells are in the circled regions. The red star indicates the location of the study in West Virginia (adapted from Quantum Reservoir Impact, LLC., 2014).

Table I: Source and receiver parameters for the Mountaineer 3D survey.

Source		**Receiver**	
Line Interval	1320 ft (402 m)	Line Interval	990 ft (302 m)
Line Bearing	132.5°	Line Bearing	42.5°
Station Interval	330 ft (101 m)	Station Interval	165 ft (50 m)
Total Sources	8,239	Total Receivers	22,352
Sources per square	64.12	Receivers per square	173.95
Line Pattern	Orthogonal	Line Pattern	Parallel

Table II shows the field recording parameters of the survey. The seismic source for this survey was 3 lb (1.4 kg) charges placed at a depth of 20 ft (6 m).

Table II: Field recording parameters of the seismic study of Mountaineer 3D prospect conducted by Bluescape/OXY.

Instrument Settings	
Sample rate	2 ms
Record Length	6000 ms
Low Cut	3 Hz
High Cut	137 Hz
Preamp gain	30 dB
Source	
Charge size	3 lb (1.4 kg)
Hole Depth	20 ft (6 m)
Receiver	
Manufacturer	Input Output Inc.
Model	SM-24
Receiver interval	216.5 ft (66 m)
Receiver Frequency	10 Hz
Maximum Offset	
Inline	13117 ft (3998 m)
Crossline	9817 ft (2992 m)

The receiver array utilized SM-24 geophones manufactured by Input Output Inc. with a frequency of 10 Hz. The SM-24 geophone is a low distortion geophone that allows a full bandwidth sampling at 2 ms intervals. The record length was 6000 ms.

2.2.1.1. Processing

The flow chart of processing of the acquired data is in Figure 6. Highlighting the region of the Marcellus was a goal of the processing, so that the resolution of the data would allow for better interpretation. Ion Geophysical completed the processing of the data set.

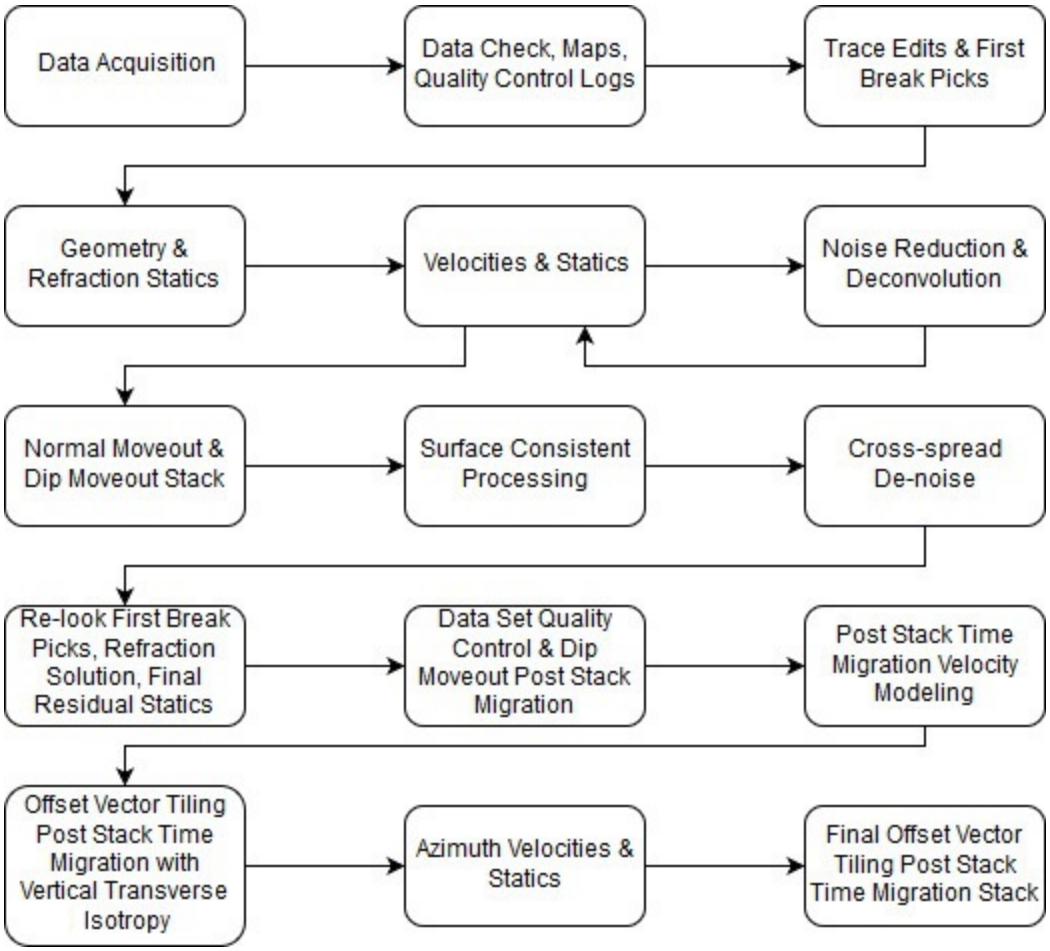

Figure 6: Processing flow completed on the Mountaineer seismic dataset by Ion Geophysical (Stewart, 2013).

2.2.2. Well Core Analysis

Each of the wells in the study region had a log of formation tops, however only a few of the wells has a core analysis. Four wells were selected for a core study, these wells were the PCSF 2-1 H, Rupert #2, Rupert 3H, and Rupert 4H. The core analysis found the Marcellus Formation within the region to be dark grey to black, slabby, massive, faintly laminated, mainly non-calcareous, organic-rich shale. The formation of this shale occurred in anoxic conditions in a basinal setting. Thickness of the formation averages 52.8 ft (16 m) from the analysis, with an average 6.28 % TOC.

In addition to the core analysis of the Marcellus Formation, a microseismic analysis, utilizing a vertical geophone array, looked at the facture azimuths of the Rupert 3H ST2, Rupert 4H, and Rupert 7H ST3 wells. The average fracture azimuth is N 52^{o} E for the three wells. Results of the fracture azimuths from the microseismic analysis are in Figure 7, and the locations of the wells used in the study are in Figure 8

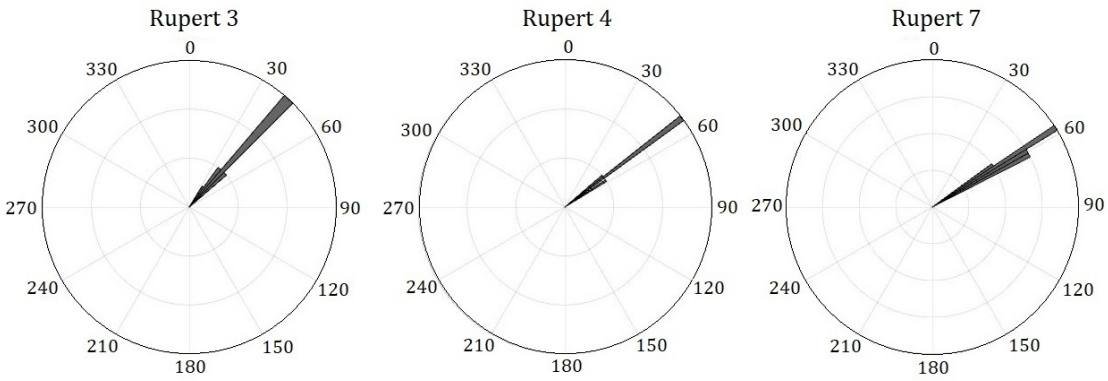

Figure 7: Results of the microseismic analysis of fracture azimuths for Rupert 3H ST2, Rupert 4H and Rupert 7H ST3 found using a vertical geophone array (Pinnacle, 2012).

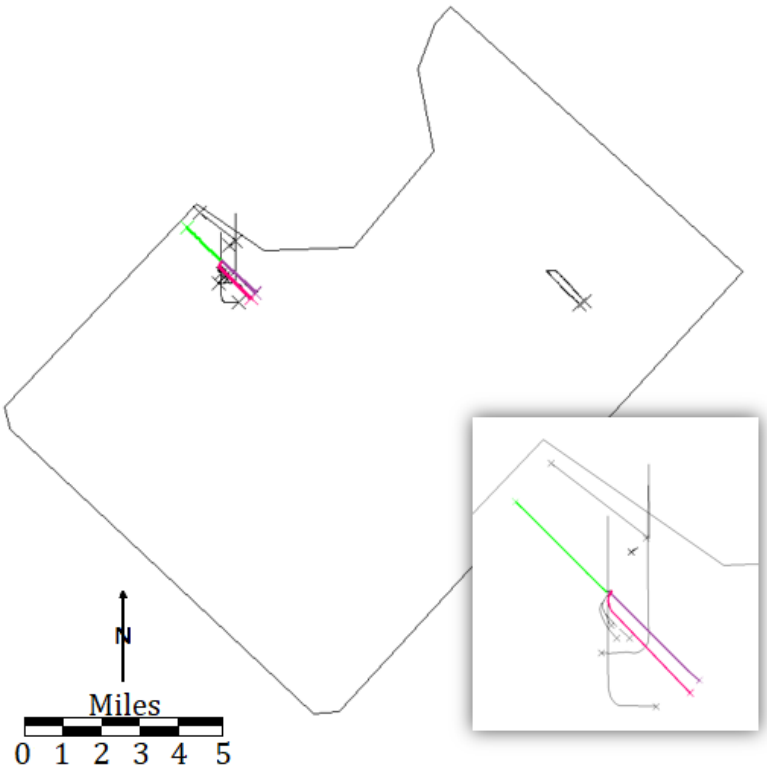

Figure 8: Highlighted locations of the wells used for the microseismic study. Rupert 3H is in green, Rupert 4H is in purple, and Rupert 7H is in pink

2.3. Seismic Attributes

Seismic attributes are components of seismic data that can highlight the more subtle features that may go unnoticed in traditional data. Certain attribute calculations aid in the mapping of discontinuities. These attributes include edge sensitive attributes, such as coherence and curvature. This attribute group enhances subtle discontinuities that can be less obvious in conventional seismic data (Gargouri, 2012).

The resolution of seismic data may cause the overlooking of certain subsurface features that attributes can resolve. Two categories make up the resolvable limits of seismic data, vertical and horizontal. Vertical resolution deals with the thinness of a layer and if that layer can have a

distinguishable top and bottom, whereas horizontal resolution is the ability to distinguish two features in close lateral proximity to one another (Dorn et al., 2017).

Attributes fall into two main classes, physical attributes and geometric attributes (Subrahmanyan, and Rao, 2008). The attribute type focused on here are geometric attributes, including semblance, coherency, similarity, and curvature. The interpretive use of geometric attributes is for the detection of faults, fractures, folds, anisotropy, and stress fields (Roden, 2015).

2.3.1. Semblance

Semblance is a discontinuity calculation that shows the similarity between adjacent traces in post-stack seismic data. Discontinuity attributes are able to detect faults, but can also pick up more subtle stratigraphic features (Kington, 2015). The equation for semblance is the square of the sums divided by the sum of the squares, Equation (1) (Seisware 10.0, 2018):

$$Semblance = \frac{\sum_{k=-K}^{K}\left[\frac{1}{J}\sum_{j=1}^{J} u_j\left(t + k\Delta t - px_j - qy_j\right)\right]^2}{\sum_{k=-K}^{K}\frac{1}{J}\sum_{j=1}^{J}\left[u_j\left(t + k\Delta t - px_j - qy_j\right)\right]^2} \quad , \qquad (1)$$

where K defines a smoothing window, J is number of traces, u_j is the shot record, t is time, Δt is change in time. And p and q define the apparent dip in x_j, and y_j directions.

Semblance – Dip Steered

The dip-steered semblance equation is similar to the semblance equation, but this semblance algorithm uses multiple cubes in the dip steering window, and uses the best semblance from all the dip cubes. Each of these dip steering cubes contains the local dip, and azimuth at each sample position. The steering cube moves trace-to-trace moving one inline or crossline position at a time shown in Figure 9.

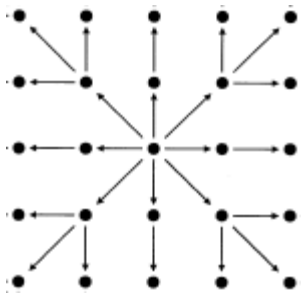

Figure 9: Seismic traces as seen from above showing how the dip steering method move trace to trace, one inline/crossline position at a time (Tingdahl and De Groot, 2003).

2.3.2. Average, Median, and Dip Azimuth Attributes

Attributes for the average and median run simple calculations across traces in the data set. The trace mix attribute calculates an average value across L number of lines, M number of traces, and N number of data samples. The trace mix triangulation attribute, is similar to the trace mix attribute. Trace mix triangulation runs a weighted average across L number of lines, M number of traces, and N number of data samples. The median calculates a median value over L number of lines, M number of traces, and N number of data samples.

The dip azimuth utilizes the dip-steered semblance. Starting with the dip-steered semblance, dip azimuth calculates the azimuth of the dip from the curve with the best semblance, and returns the direction of the most prominent dip at a location. Dip azimuth returns the azimuth of dip of seismic reflectors making this attribute useful in determining fault orientations (Jaglan et al., 2015).

2.3.3. Curvature

Curvature is used to describe the two-dimensional property of a curve related to how deviated from a straight line the curve is (Figure 10).

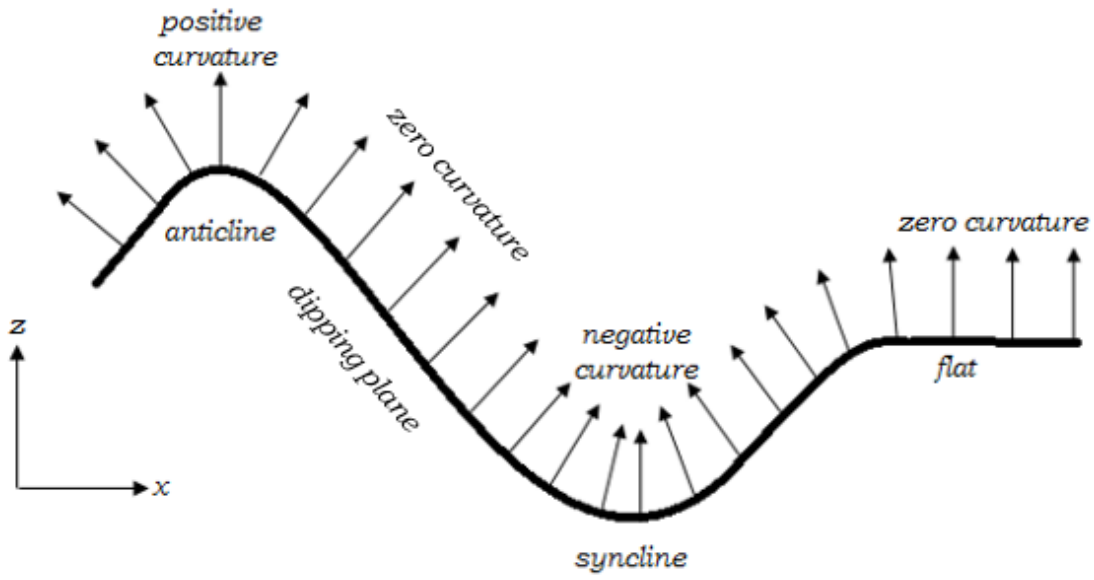

Figure 10: 2-D curvature showing the sign conventions adapted from Roberts, 2011.

While curvature of a surface is dependent on the two-dimensional cross section, a three-dimensional form of curvature is obtainable by combining the many 2D curvatures. Equation (2), below, shows the curvature equation:

$$K = \frac{d\omega}{dS} = \frac{2\pi}{2\pi R} = \frac{1}{R} \quad , \tag{2}$$

where dω is the rate of change of the angle, dS is the arc length, and R is the radius of curvature. The curvature equation in terms of derivatives is below in Equation (3):

$$K = \frac{\frac{d^2y}{dx}}{\left(1 + \left(\frac{dy}{dx}\right)^2\right)^{3/2}} \quad , \tag{3}$$

where x and y define the horizontal and vertical location of a point on a curve. Curvature is very susceptible to noise, especially high-frequency noise, therefore an application of multiple iterations of curvature calculations is necessary. Even with the removal of high-frequency noise, the interpretation of curvature attributes is very dependent on the aperture. A small aperture is desirable, if the goal is to view local surface detail, while a large aperture is ideal for looking for

regional trends. In addition to aperture size, the color scheme selected for interpretation can vary the results because some color combinations will highlight different features in the results.

Equation (4) shows the least-squares equation of the combination of an ellipsoid and plane utilized in obtaining the equations for the curvature attributes:

$$y = ax^2 + by^2 + cxy + dx + ey + f \quad , \tag{4}$$

where Equations (5), (6), (7), (8), (9), and (10) show the terms used in the least-squares equations found from a map grid of the seismic surface (Roberts, 2011). Figure 11 shows the map grid used to derive the coefficients of the least-squares equation.

$$a = \frac{1}{2}\frac{\partial^2 z}{\partial x^2} = \frac{(z_1 + z_3 + z_4 + z_6 + z_7 + z_9)}{12\Delta x^2} - \frac{(z_2 + z_5 + z_8)}{6\Delta x^2} \quad , \tag{5}$$

$$b = \frac{1}{2}\frac{\partial^2 z}{\partial x y^2} = \frac{(z_1 + z_2 + z_3 + z_7 + z_8 + z_9)}{12\Delta x^2} - \frac{(z_4 + z_5 + z_6)}{6\Delta x^2} \quad , \tag{6}$$

$$c = \frac{\partial^2 z}{\partial x \partial y} = \frac{(z_3 + z_7 - z_1 + z_9)}{4\Delta x^2} \quad , \tag{7}$$

$$d = \frac{\partial z}{\partial x} = \frac{(z_3 + z_6 + z_9 - z_1 - z_4 - z_7)}{6\Delta x} \quad , \tag{8}$$

$$e = \frac{\partial z}{\partial y} = \frac{(z_1 + z_2 + z_3 - z_7 - z_8 - z_9)}{6\Delta x} \quad , \tag{9}$$

$$f = \frac{2(z_2 + z_4 + z_6 + z_8) - (z_1 + z_3 + z_7 + z_9) + 5z_5}{9} \quad . \tag{10}$$

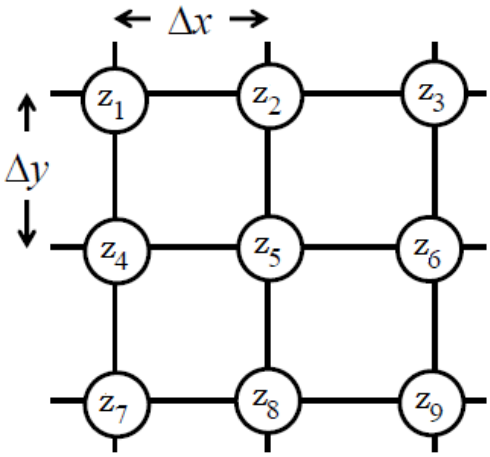

Figure 11: Map grid of 3D surface used to derive the coefficients in Equations (5), (6), (7), (8), (9), and (10) of the least squares equation (4) where z represents points on the map grid.

2.3.3.1. Mean Curvature

Mean curvature, K_m, is the average of two curvatures through any one point. Maximum curvature tends to dominate the mean curvature. This curvature calculation is not a particularly useful visual attribute for interpretation, but is required in the calculations of other attributes. The equation for mean curvature shown in Equation (11) takes any two pairs of orthogonal curvatures, K_1 and K_2 (Roberts, 2001):

$$K_m = \frac{K_1 + K_2}{2} = \frac{a(1+e^2) - cde + b(1+d^2)}{(1+d^2+e^2)^{3/2}} \quad . \tag{11}$$

2.3.3.2. Gaussian Curvature

Gaussian curvature, K_g, is the product of the principal curvatures, sometimes referred to as the total curvature. This curvature takes the product of the minimum and maximum curvatures shown below in Equation (12):

$$K_g = K_{min}K_{max} = \frac{4ab - c^2}{(1+d^2+e^2)^2} \quad , \tag{12}$$

where K_{min} is the minimum curvature and K_{max} is the maximum curvature at a point on a surface. Due to the rapid sign changes from the minimum curvature fluctuating about zero, it is not ideal for delineating faults. However, the absolute Gaussian curvature resolves the issue that arises from the minimum curvature fluctuations and can thus be useful in fault characterization. Even with the absolute calculation, the Gaussian curvature only has limited application to mapped surfaces (Roberts, 2001).

2.3.3.3. Maximum Curvature

The maximum curvature, K_{max}, is the one curve from an infinite number of curves at a single point, which has the absolute largest curvature. The equation for maximum curvature is below in Equation (13):

$$K_{max} = K_m + \sqrt{K_m^2 + K_g} \quad , \tag{13}$$

where K_m is the mean curvature and K_g is the Gaussian curvature. The maximum curvature is effective at delineating faults and fault geometries while defining the orientation. Positive results represent a fault with up-throw, while negative results represent a down-throw (Hardeep et al., 2015).

2.3.3.4. Minimum Curvature

Minimum curvature, K_{min}, is the one curve from an infinite number of curves that has the absolute smallest curvature and is perpendicular to the maximum curvature. The equation for minimum curvature is below in Equation (14), where K_m is the mean curvature and K_g is the Gaussian curvature:

$$K_{min} = K_m - \sqrt{K_m^2 - K_g} \quad . \tag{14}$$

The surface lacks fractures when the results of this curvature are zero or near zero, while large values indicate non-isometric distortion such as faulting and fracturing. Minimum and maximum curvatures are the most useful in highlighting subtle flexures and folds (Chopra et al., 2009).

2.3.3.5. Most Positive and Most Negative Curvature

Most positive and most negative curvatures are able to resolve information contained in the maximum curvature by using an edge type display, these curvatures search normal curvatures for the most positive and most negative values (Chopra and Marfurt, 2006). The equations for most positive curvature and most negative curvature are below in Equations (15) and (16) respectively, where K_+ is the most positive curvature, and K_- is the most negative curvature:

$$K_+ = (a+b) + \sqrt{(a-b)^2 + c^2} \quad , \tag{15}$$

$$K_- = (a+b) - \sqrt{(a-b)^2 + c^2} \quad , \tag{16}$$

where a, b, and c are from Equations (5),(6), and (7) respectively.

Lineaments in these curvature attributes take on a polygonal appearance, but the shape information of the lineament is not preserved. These attributes exaggerate linear features in 3D data, which can be helpful when identifying faults and smaller linear features. One problem with the most positive and negative attributes are processing and acquisition footprints can affect the most positive and most negative curvature, but are avoidable by utilizing multiple normal curvature orientations (Roberts, 2011).

2.3.3.6. Dip Curvature

Dip curvature, K_s, also known as profile curvature, is the curvature measured in the direction of maximum dip, meaning it measures the rate of change of the dip in the maximum dip direction. Dip curvature can preserve the magnitude and direction of a fault, but has a tendency

to exaggerate any local relief. The exaggeration can be beneficial however, when looking at compacted features such as debris flows and channelized bodies. Equation (17) shows the dip curvature equation (Roberts, 2011):

$$K_s = \frac{2(ae^2 - cde + bd^2)}{(d^2 + e^2)(1 + d^2 + e^2)^{\frac{1}{2}}} \quad , \tag{17}$$

where a, b, c, d, and e are from Equations (5), (6), (7), (8), and (9) respectively

2.3.3.7. Strike curvature

Strike curvature is the curvature taken normal to the dip curvature, and is referred to as the tangential curvature. This curvature, unlike many others, can describe the shape of a surface. The most common use for strike curvature is terrain analysis where it can be helpful in understanding regional migration pathways of hydrocarbons (Roberts, 2001).

2.3.4. Similarity

Similarity is a coherency attribute. Coherency attributes, proposed in 1995, measure the variance in seismic data, allowing for the location of discontinuities (Gargouri, 2012). Like curvature, similarity is a post-stack attribute. Similarity calculates the coherence of amplitudes on adjacent trace using cross correlation, meaning similarity measures the lateral changes in the waveform (Chopra and Marfurt, 2008). Similarity uses a 3D cube I_1 x I_2 x I_3 where subscripts represent dimensions in time/depth, inline, and crossline for calculating variance. Coherency type attributes are most beneficial in the highlighting of structural and stratigraphic discontinuities such as faults, fractures, or channels (Alaudah and AlRegib, 2017)

2.4. Anisotropy

Seismic anisotropy refers to the variations in the directionally dependent elastic wave propagation velocity. The study of anisotropy has many applications such as studying mantle

convection, subduction zones, plate boundaries, continental and lithospheric structure, monitoring of CO_2 storage and the exploration and extraction of hydrocarbons. Many factors can contribute to anisotropy including aligned fractures, solid or liquid filled inclusions, sedimentary deposition and layering, and alignment of crystals by solid-state deformation (Walker and Wookey, 2012). The method of azimuthal anisotropy analysis, in this case, utilizes the idea that fractures create anisotropy that can appear in data as azimuthal variations (Coulombe et al., 2013).

Shales, such as those in the Marcellus Formation, exhibit strong intrinsic anisotropy (Chapman et al., 2015). A number of factors attribute to the intrinsic anisotropy of shales such as orientation of clay, micro-cracks, fine layering, fluid filled porosity, and anisotropy induced by stress (Cholach and Schmitt, 2003). Anisotropy data in shales is useful for determining possible indicators of oil and gas traps created by fracturing. Fracturing causes the wave propagation velocity through a media to be slower when the direction of the wave is perpendicular to the alignment direction of the fractures.

Many of the fracture detection methods use an azimuthal amplitude variation with offset (AVO) and quantitative azimuthal inversion (Dorn and Dominquez, 2017). Two of the main methods utilized are velocity variations with azimuth (VVAz), which uses P-wave interval velocity as a function of azimuth, and the AVAz that uses the change in reflectivity/amplitude as a function of azimuth. The VVAz and the AVAz methods are both useful in the detection of fracture intensity and orientation, but can require considerable amounts of time for data conditioning and analysis (Chopra, 2011).

Unlike the AVAz method, VVAz uses the base of the target for analysis and not the top. An ellipse in the horizontal plane can estimate azimuthal variations if the medium is arbitrarily

anisotropic, travel times increase with offset, and travel times exist for all offsets. Using an interval velocity analysis is beneficial because it is less sensitive to effects of the overburden (Al Dulaijan and Margrave, 2015)

Migration removes the azimuthal information many seismic anisotropy methods require. A common method used for preserving azimuths in seismic anisotropy analysis is offset vector tiling (OVT). OVT methods are convenient for improving imaging of fractured reservoirs by providing better illumination, imaging quality, and multiple elimination. OVT, proposed in 1998 by Vermeer (Calvert et al., 2008), works with many land surveys because these surveys fit the criteria of orthogonal, full coverage, wide azimuth, and large offset (Yue et al., 2016). The binning process creates a number of sub-volumes, or offset vector tiles, containing the same offset and azimuth using the x- and y-offset. Since migration is necessary for both the VVAz and AVAz method to remove dip dependency, the use of OVT data is beneficial because it allows for the application of migration on each of the sub-volumes while preserving the azimuth information (Al Dulaijan, 2017). Azimuthal fast direction of velocity from VVAz with OVT processing is used in this research.

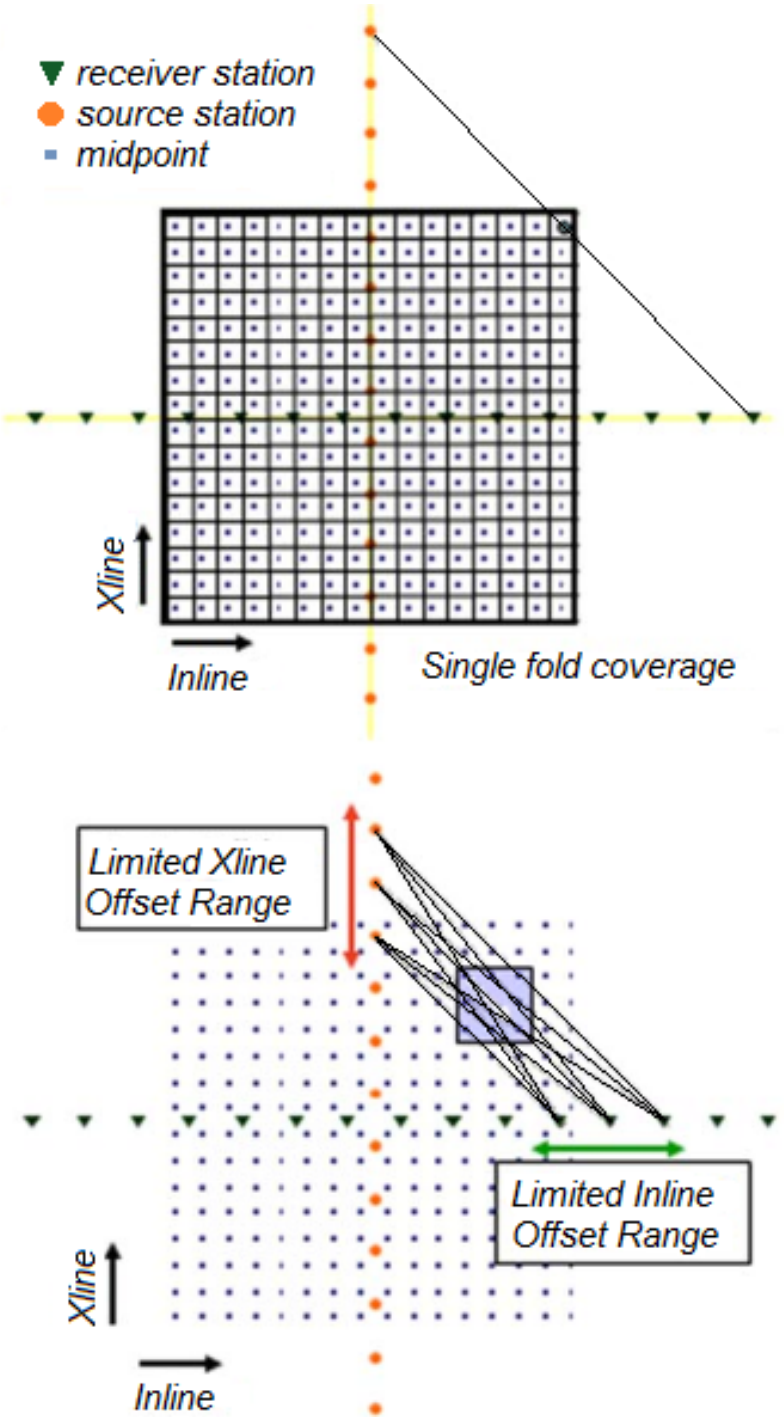

Figure 12: Common offset tiles use traces from specified inline and crossline offsets. Full single fold coverage of a region, with bins of similar offset and azimuth, is achievable by selecting tiles sizes to match the source and receiver line spacing (Valler et al., 2012).

3. Results

3.1. Geological Horizons

Mapping the geological horizons began by first utilizing the formation tops provided from the well logs. Table III shows all of the formations encountered by the wells within the study region. Of the formations encountered by the wells, the formations included in mapping were the Rhinestreet, the Marcellus (lower), and the Newberg.

Table III: List of formations mentioned in well logs across the study region.

Weir	Gordon	Juniata	Onondanga	Squaw
Berea	Greenbrier	Lake Erie	Oriskany SS	Sycamore
Big Lime	Helderberg	Lower Marcellus	Point Pleasant	Trenton
Cherry Valley	Huntersville	Mahantango	Ravencliff	Tully Limestone
Elk	Huron	Mckenzie	Rhinestreet	Tuscarora
Geneso	Injun	Newberg	Rose Hill	Upper Marcellus

Figure 13 shows the well paths of Rupert 2H, Rupert 4H, and Rupert 7H ST 1, 2, and 3 with formation tops of the Rhinestreet, upper and lower divisions of Marcellus.

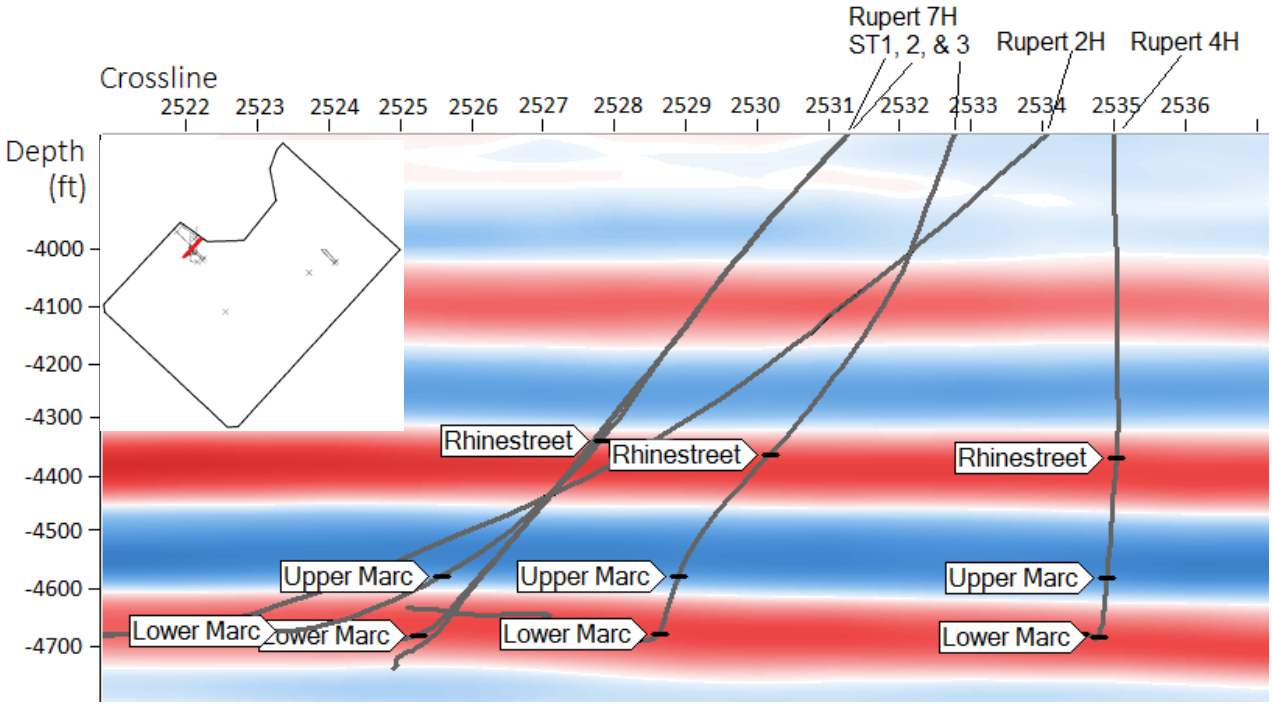

Figure 13: Zoomed in section of seismic on inline 1083 showing well paths of Rupert 2H, Rupert 4H, and Rupert 7H stages 1, 2, and 3. Well paths, shown in gray, indicate where the formation tops are, using information from the well logs. Shown are the tops for the upper and lower sections of the Marcellus and Rhinestreet Formations. Insert map of region shows, in red, the section of inline 1083.

After mapping horizons on lines intersecting wells, the mapping of every 50th crossline, and then every 50th inline created a grid (Figure 14) for an auto-picker to interpolate the horizon locations over the region. The auto-picker function in Seisware 10.0 is a single seed auto-picker; the use of multiple seed lines improves the performance of the auto-pick function. I completed a line-by-line review of the study region to check the accuracy of the auto-picker.

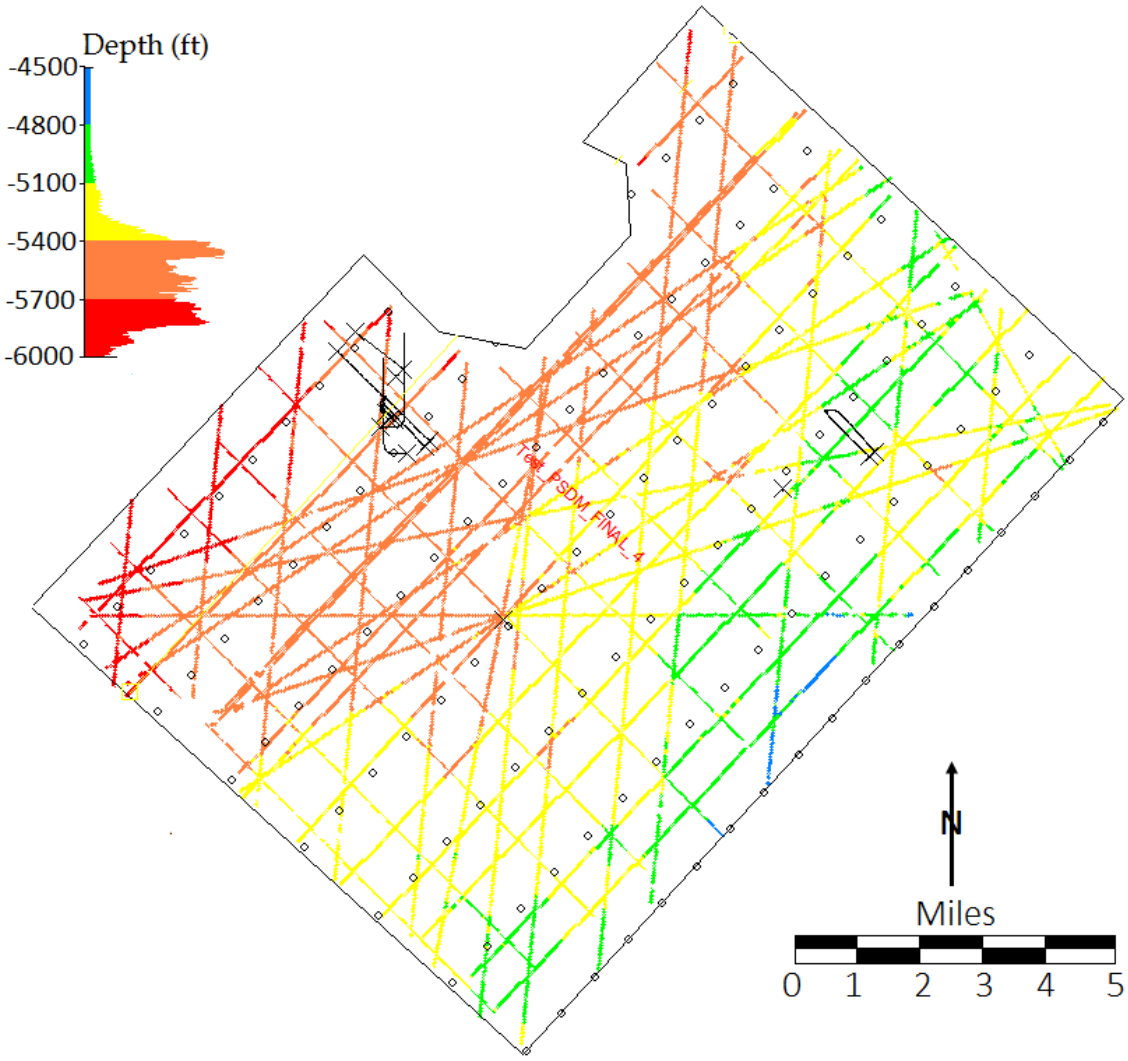

Figure 14: Seismic study region with colored lines representing the seed lines used for selecting the Newberg Formation horizon before running the Seisware auto-picker to extrapolate picks across the region. The color of the lines represents the depth of the geologic horizon at that location.

3.1.1. Rhinestreet

Of the formation horizons mapped, the Rhinestreet Formation is the shallowest. The mapping of this formation is beneficial because this formation contains a duplexing feature across the study area. The duplex feature suggests faulting and folding occurring across the formation and is in the cross-section in Figure 15.

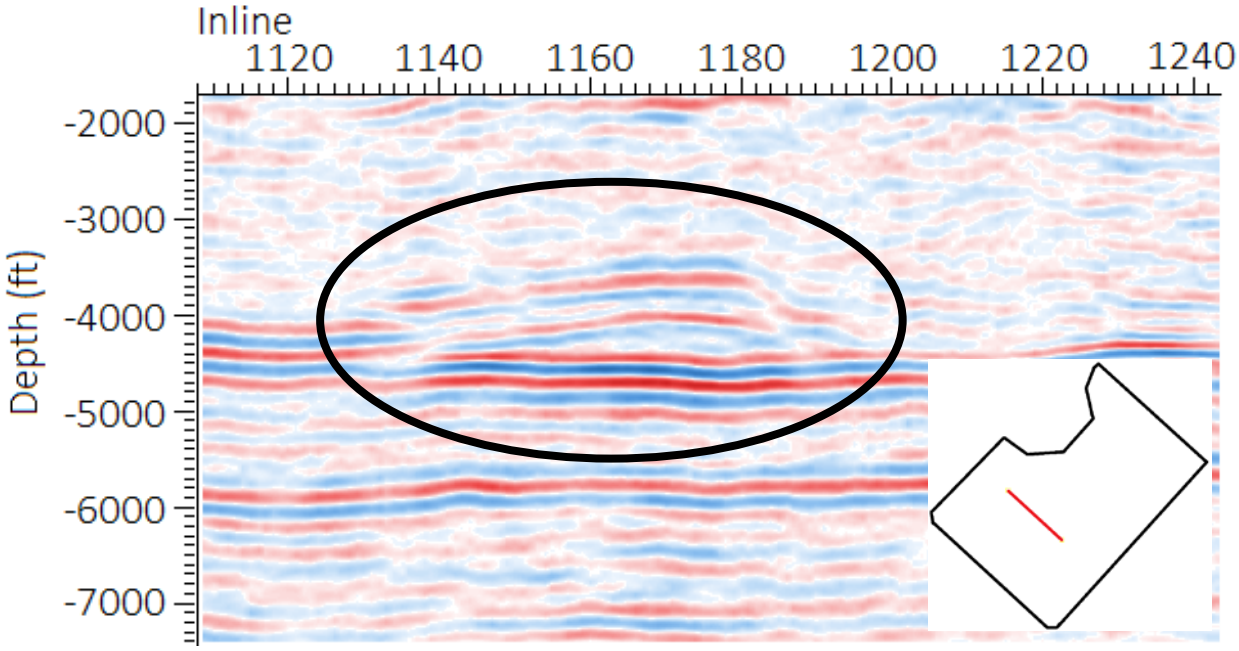

Figure 15: The duplexing feature present within the region in cross section along crossline 2438. Crossline 2438 is in red on the inset map of the region.

Figure 16 shows a grid and surface contour map of the Rhinestreet Formation with depths ranging from 3500 to 5000 ft (1067 to 1524 m).

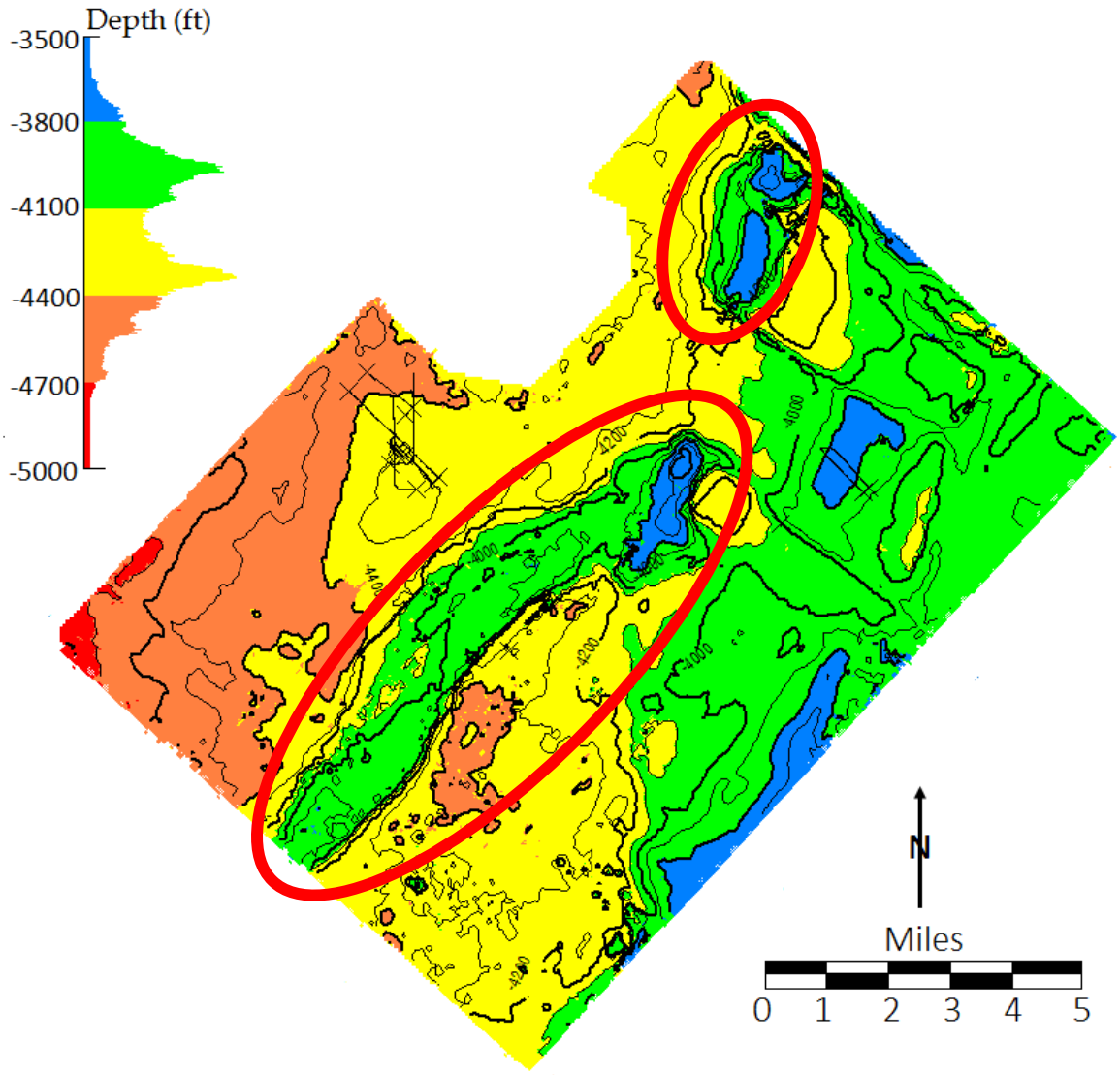

Figure 16: Rhinestreet Formation surface horizon contour map depths ranging from 3500 ft to 5000 ft (1067 to 1524 m). The duplexing feature trends from the southwest to northeast, circled in red. A duplex feature trends from SW-NE across the study area. The deepest regions of the formation horizon are in red, while the shallowest are in blue.

3.1.2. Marcellus Formation

The horizon of the lower Marcellus Formation is important to map because it is the producing shale and the target of the wells. The lower Marcellus Formation was the horizon mapped of the two Marcellus divisions (upper and lower). The depth of the lower Marcellus

Formation ranges from 4000 ft to 5000 ft (1219 to 1524 m) across the study region. A surface contour map of the lower Marcellus is in Figure 17.

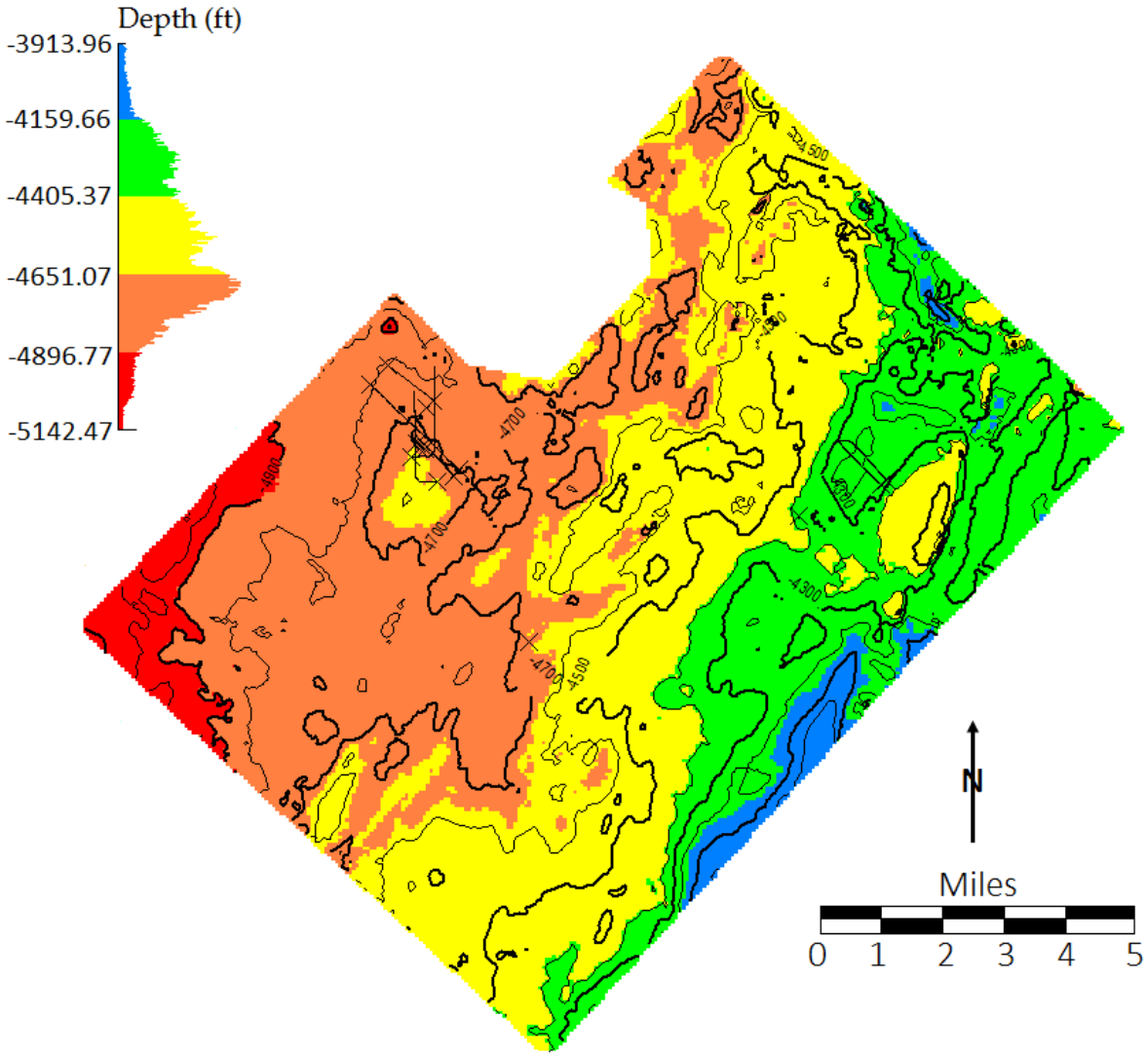

Figure 17: Lower Marcellus Formation horizon surface contour map across the region of study with depths to the formation ranging from 4000 ft to 5000 ft (1219 to 1524 m), with the deepest section being in the western edge of the region. The deepest regions of the formation horizon are in red, while the shallowest are in blue.

3.1.3. Newberg Formation

The deepest and last horizon mapped was the Newberg Formation. The mapping of the Newberg aided in the editing of horizon picks for the other two horizons. Depths of the

formation range from 4500 ft to 6000 ft (1372 to 1829 m). Figure 18 shows a surface contour map of the Newberg horizon.

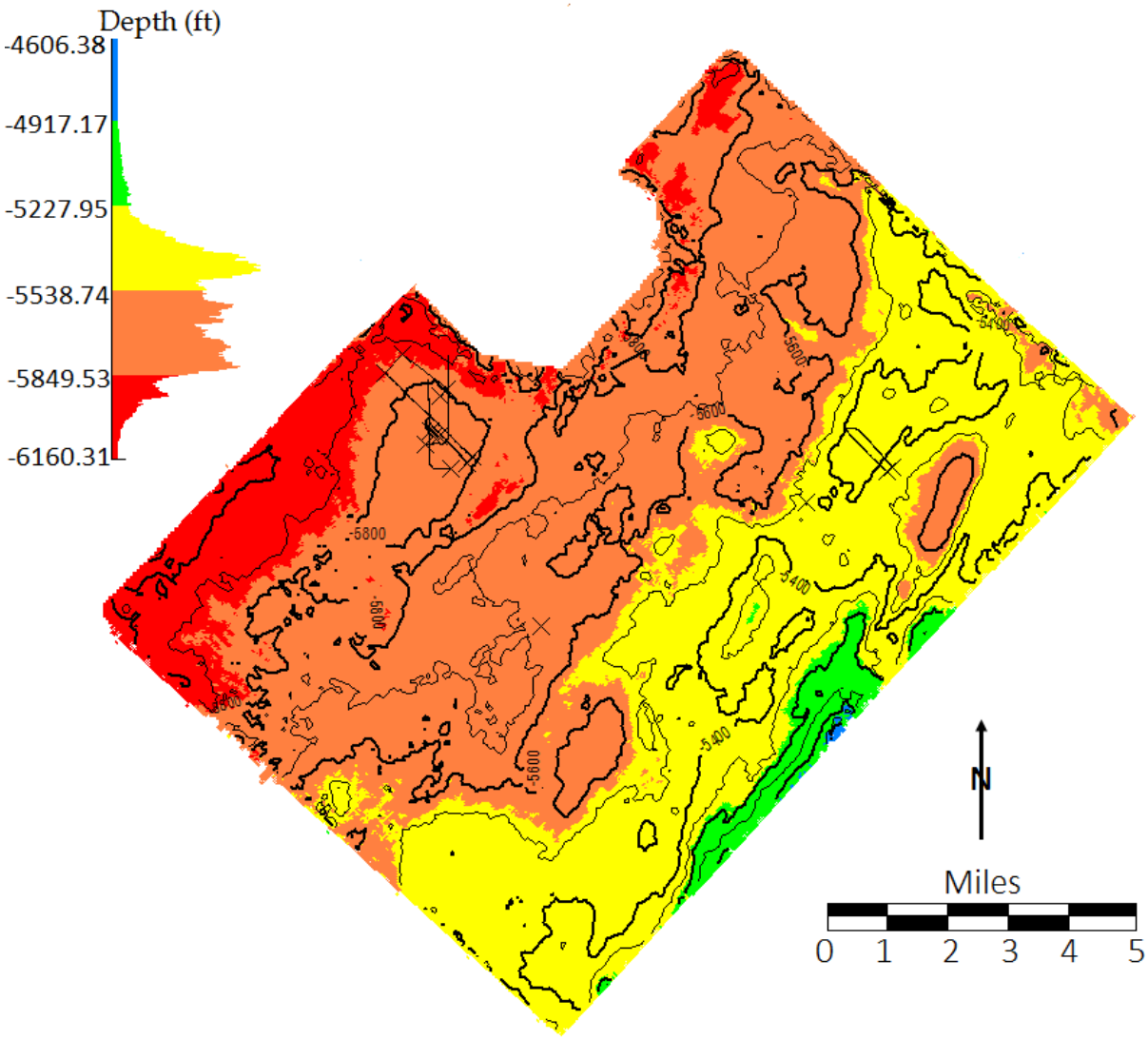

Figure 18: Newberg Formation horizon surface contour map with depths ranging from 4500 ft to 6000 ft (1372 to 1829 m). The deepest regions of the formation horizon are in red, while the shallowest are in blue.

3.2. Seismic Attributes

3.2.1. Regional Attributes

The Rhinestreet, lower Marcellus, and Newberg Formation horizons are all within the attribute calculation window of 3000 to 6000 ft (914 to 1829 m) that I used for this study. Figure

19 shows a cross section of the post-stack migrated seismic data, with a wiggle trace overlay of the semblance attribute calculation.

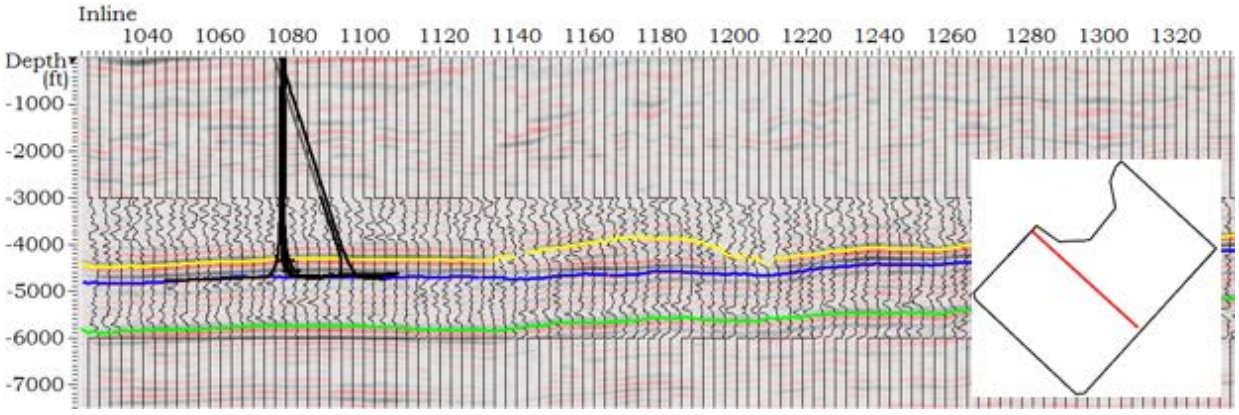

Figure 19: Seismic cross section of the post-stack depth migrated data (interpolated density display) with an overlay of the results of the semblance attribute calculation (wiggle display) at the crossline 2541. Well paths for the MWV are black, the top of the Rhinestreet formation horizon is yellow, the top of Marcellus formation horizon is blue, and the top of Newberg formation horizon is green. Crossline 2541 is in red on the inset map of the region.

Figure 20, Figure 21, and Figure 22 show horizontal slices of the results of the dip azimuth, mean curvature, and dip curvature at a depth of 4350 ft (1326 m). The depth of 4350 ft (1326 m) intersects the Marcellus Formation. The result of dip azimuth highlights the orientation of features within the region. Mean curvature, like the other curvature attributes, shows the major faulting within the region; however, mean curvature shows more of the subtle features than the results of minimum, maximum, most positive, and most negative curvature. Dip curvature highlights potential faults across the region, as well as the orientation trend of the area. The results of the semblance, dip-steered semblance, trace mix, trace mix triangulation, median, Gaussian curvature, maximum curvature, minimum curvature, most positive curvature, most negative curvature, strike and dip attribute calculations are shown in Appendix A. I judged the attribute results based on the number of faults that could be located within a region. Fault counts for each attribute in the selected region are in Appendix B.

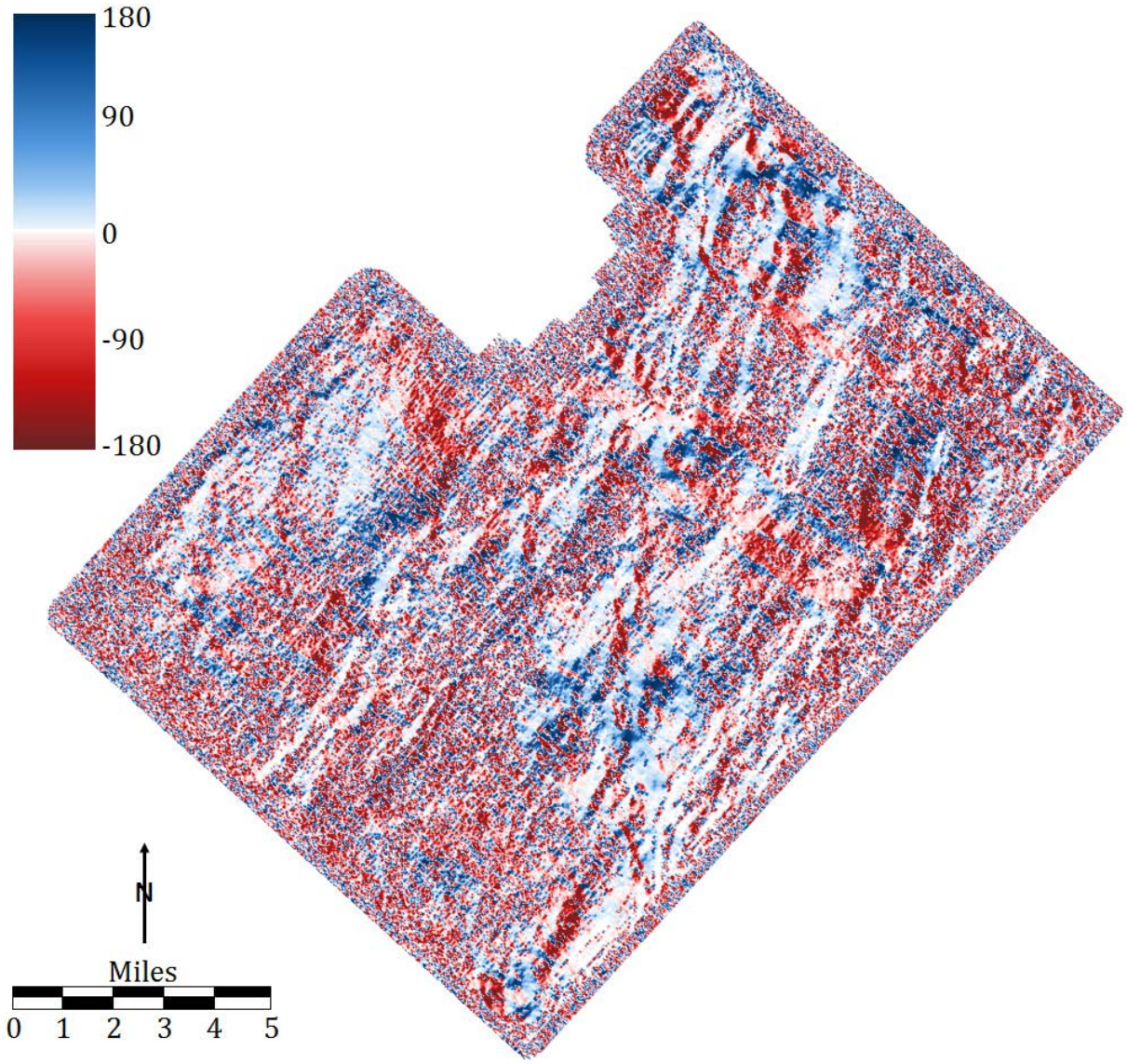

Figure 20: Results of the dip azimuth attribute calculation at a depth of 4350 ft (1326 m).

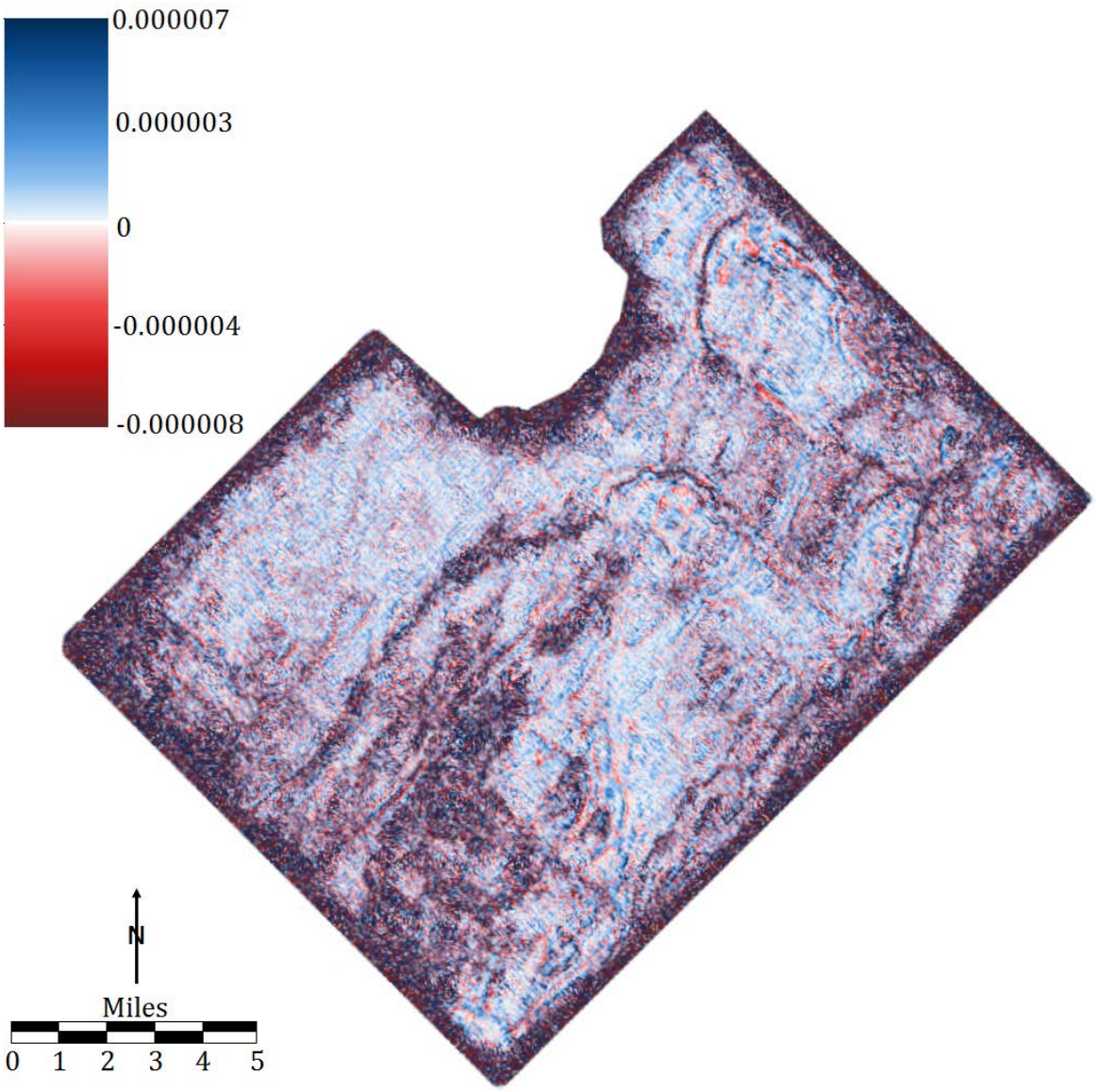

Figure 21: Results of the mean curvature attribute calculation at a depth of 4350 ft (1326 m).

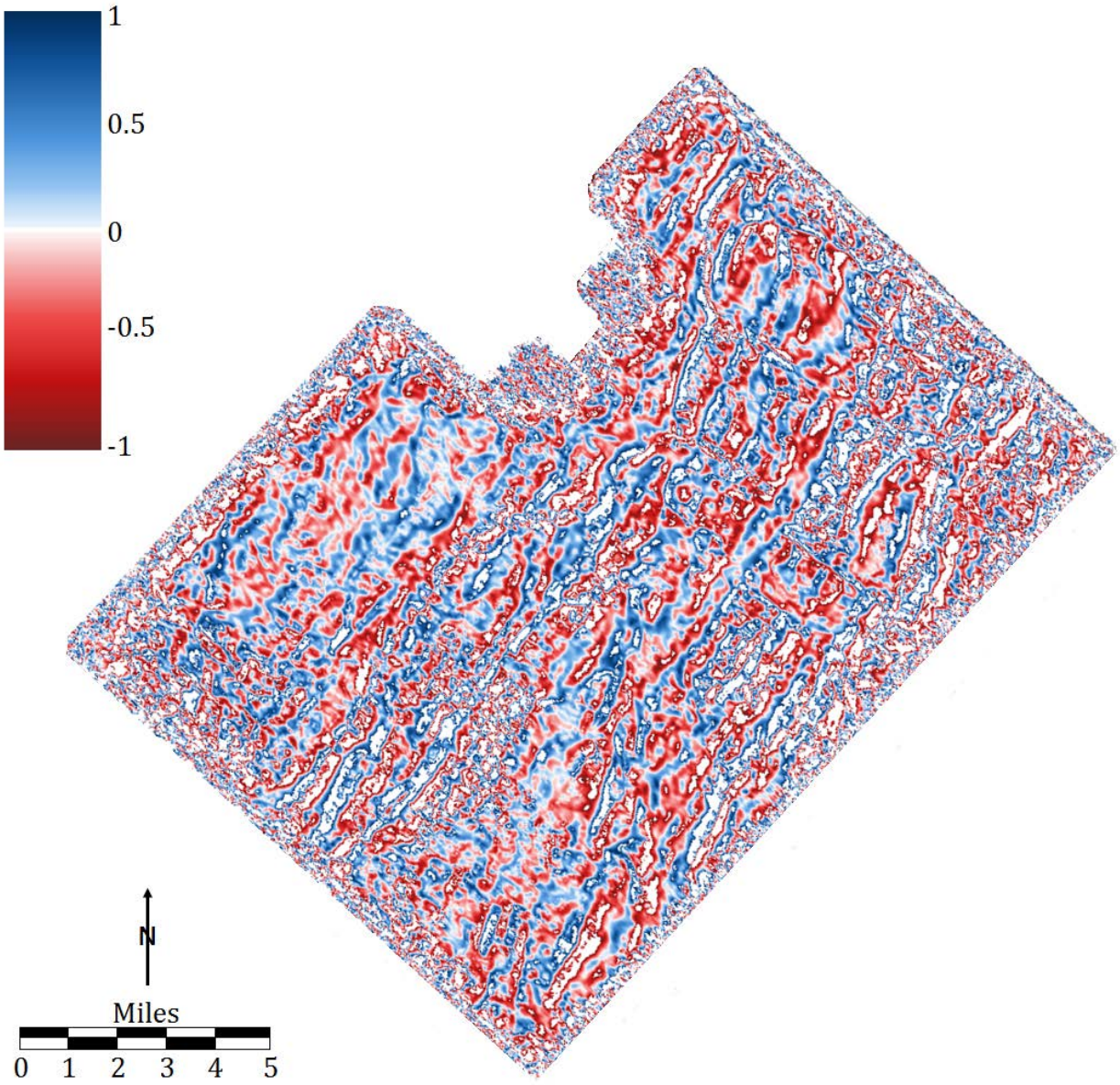

Figure 22: Results of the dip curvature attribute calculation at a depth of 4350 ft (1326 m).

3.2.2. Horizon Attributes

Attributes calculated along the lower Marcellus horizon supplement the attribute calculations at 4350 ft (1326 m) depth. Lower Marcellus horizon attributes use the same calculations as attributes for the 4350 ft (1326 m) depth slice; however, the calculation is directly

along the lower Marcellus horizon. Results of the calculation for mean curvature and dip curvature are in Figure 23 and Figure 24 respectively.

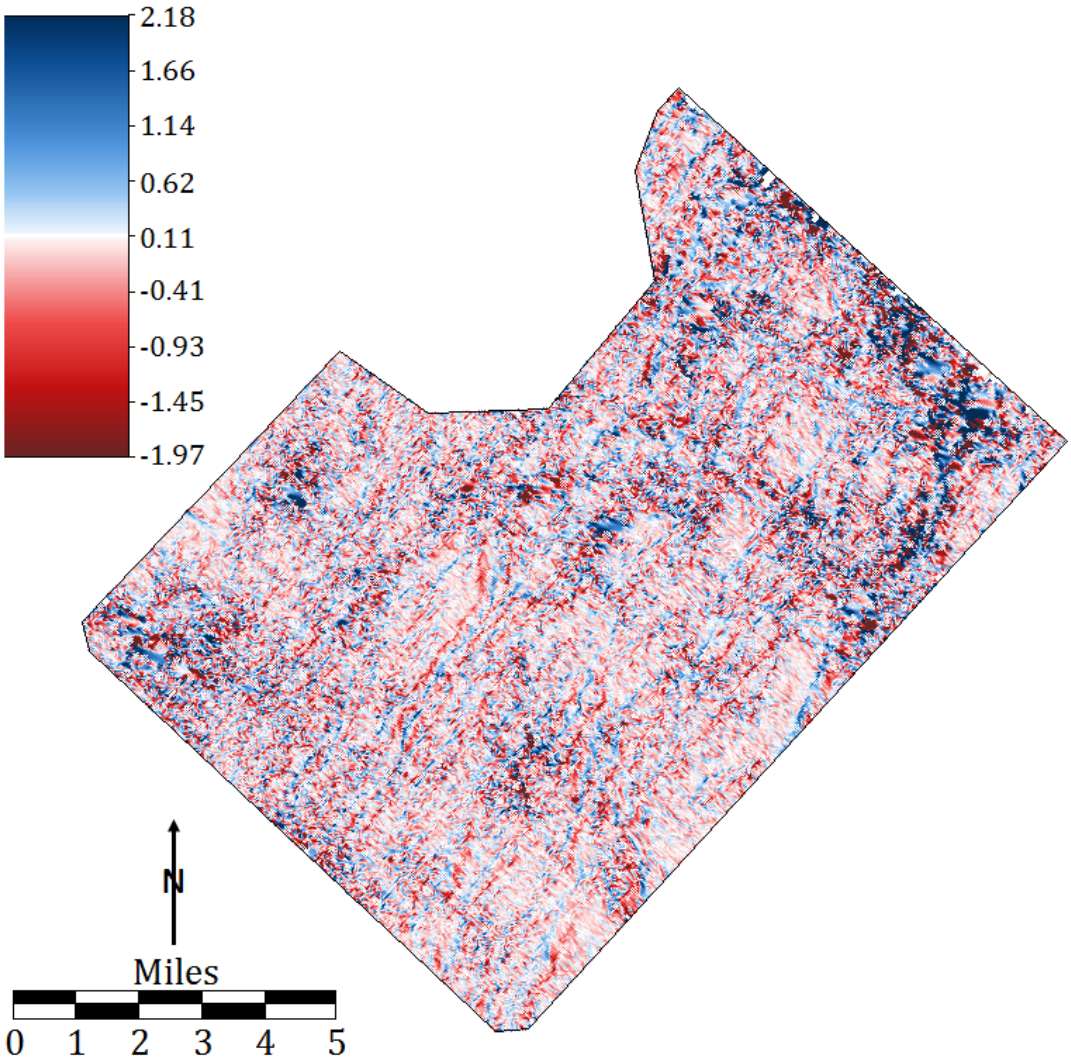

Figure 23: Results of the mean curvature attribute calculated along the lower Marcellus horizon.

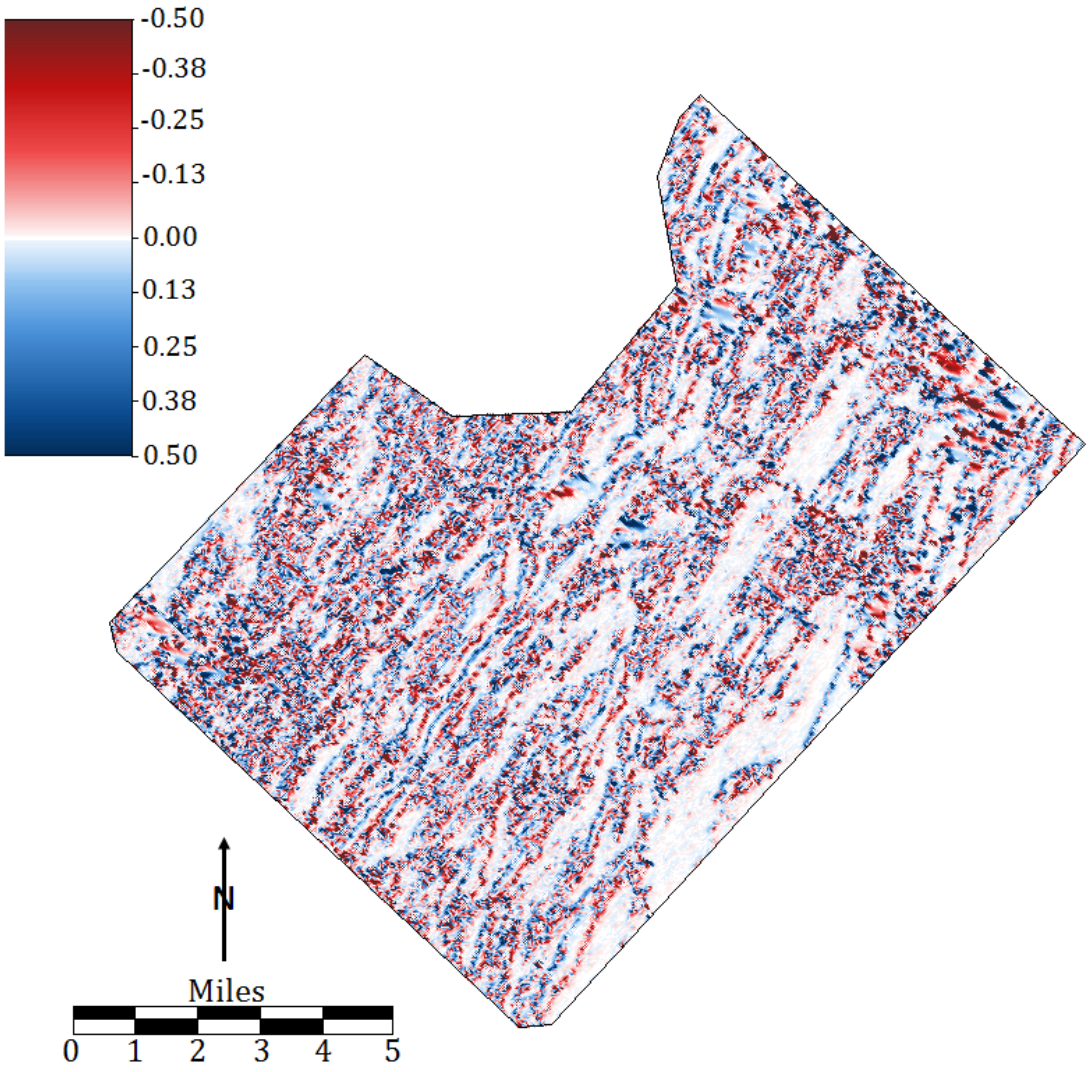

Figure 24: Results of dip curvature attribute calculated along the lower Marcellus horizon.

I mapped the potential fault location within a selected region for each of the attribute calculation to determine which attributes produced the best results. I judged each attribute based on the number of potential faults that could be located within the selected region, these results are in Appendix C. The results of mean curvature and dip curvature had the highest potential fault counts for the horizon attributes within this region. Results of the calculations for dip,

azimuth, maximum curvature, minimum curvature, most positive curvature, most negative curvature, and strike curvature are in Appendix D.

Rose diagrams of the lineament azimuths along the horizon determined from the mean curvature horizon calculation on the Marcellus are in Figure 25. The selection of the mean curvature for this calculation was due to the attributes ability to highlight both the orientation and location of lineaments. While dip curvature provided the best results, mean curvature also provided good results based on the potential fault counts with similar results to those of dip curvature. The azimuth of individual lineaments, measured by hand, were input into the code in Appendix E. The code creates an array of the input azimuths, and adds an azimuth that is 180^{o} more than the measured azimuth. The added azimuths are included for emphasis of orientation. The code then creates rose diagrams using the Matlab function polarhistogram.

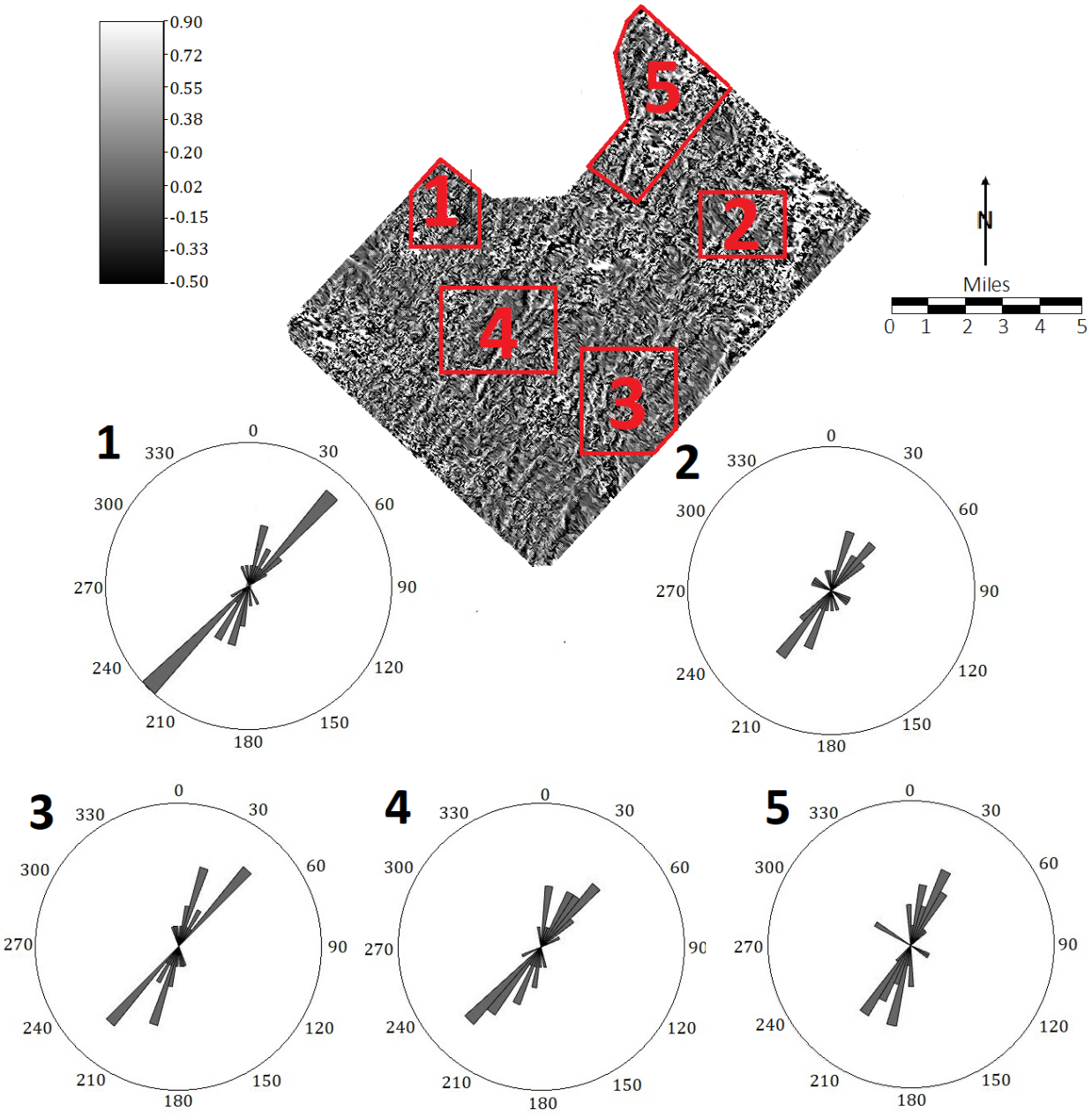

Figure 25: Rose diagrams from lineament azimuth measurements taken by hand, from the results of the mean curvature attribute calculation (above in gray scale) on the lower Marcellus horizon. Results are from the five regions located on the map in red. Code to generate the rose diagrams is in Appendix E.

3.3. Anisotropy

Figure 26, Figure 27, and Figure 28 show the results of azimuthal anistropy mapping of the V_{fast} direction using the azimuthal data from the OVT processing at depths 3900 ft, 4350 ft, and 4545 ft respectively (1189, 1326, and 1568 m). The depths selected represent the shallowest depth, mid- range, and deepest depth of the lower Marcellus. Code used for mapping is in Appendix F. The code reads in OVT anisotropy data, then creates a vector plot using the Matlab function quiver.

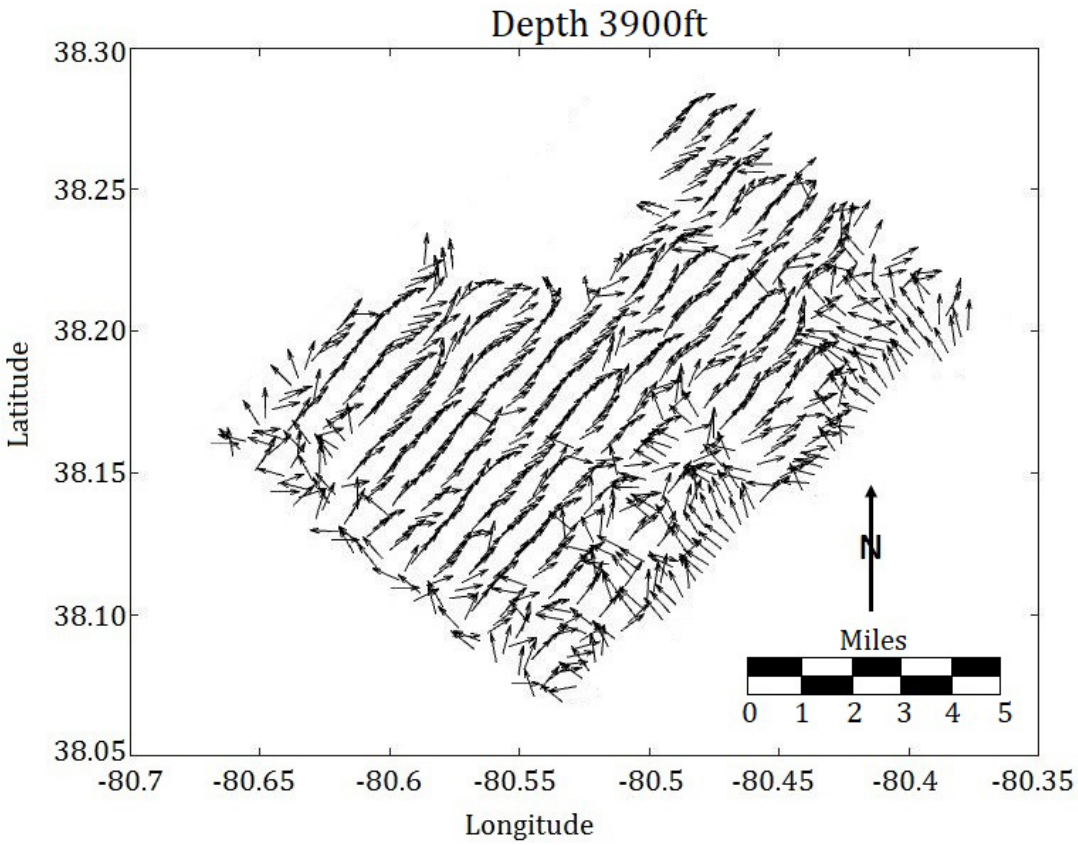

Figure 26: Azimuth of the fast direction results for a horizontal slice at a depth of 3900 ft (1189 m).

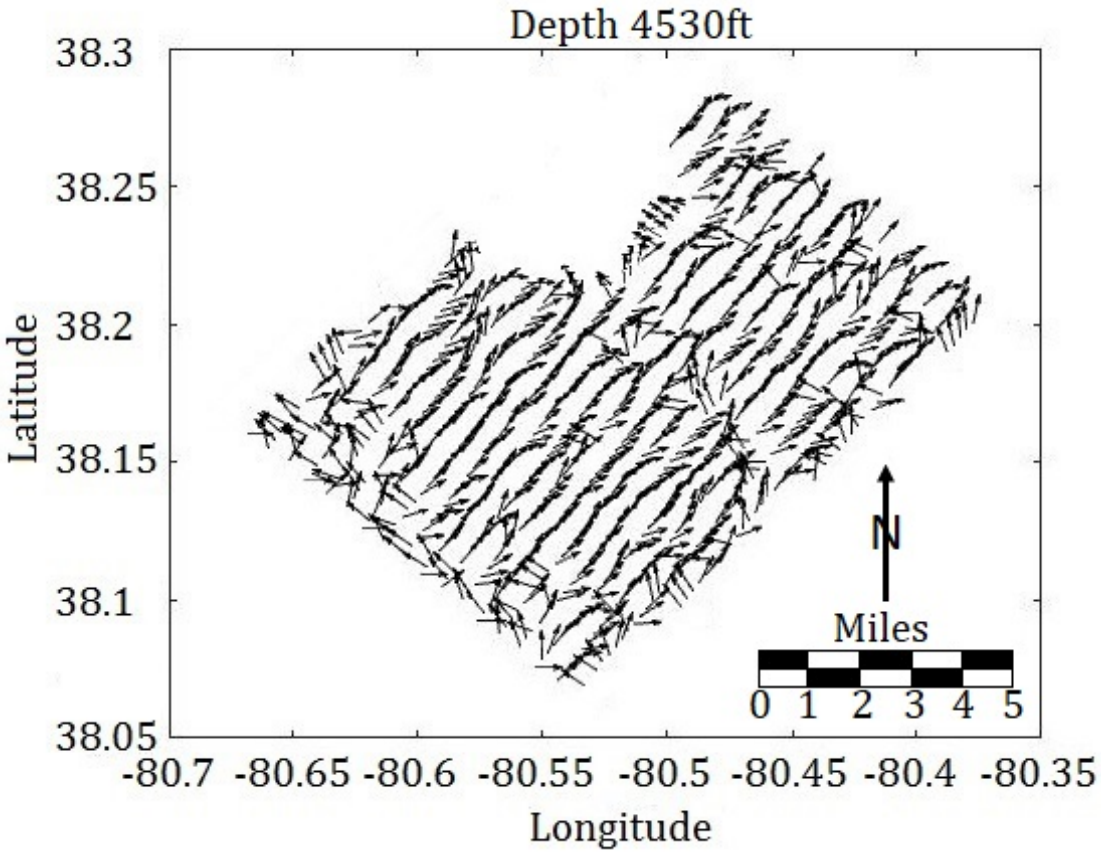

Figure 27: Azimuth of the fast direction results for a horizontal slice at a depth of 4530 ft (1326 m).

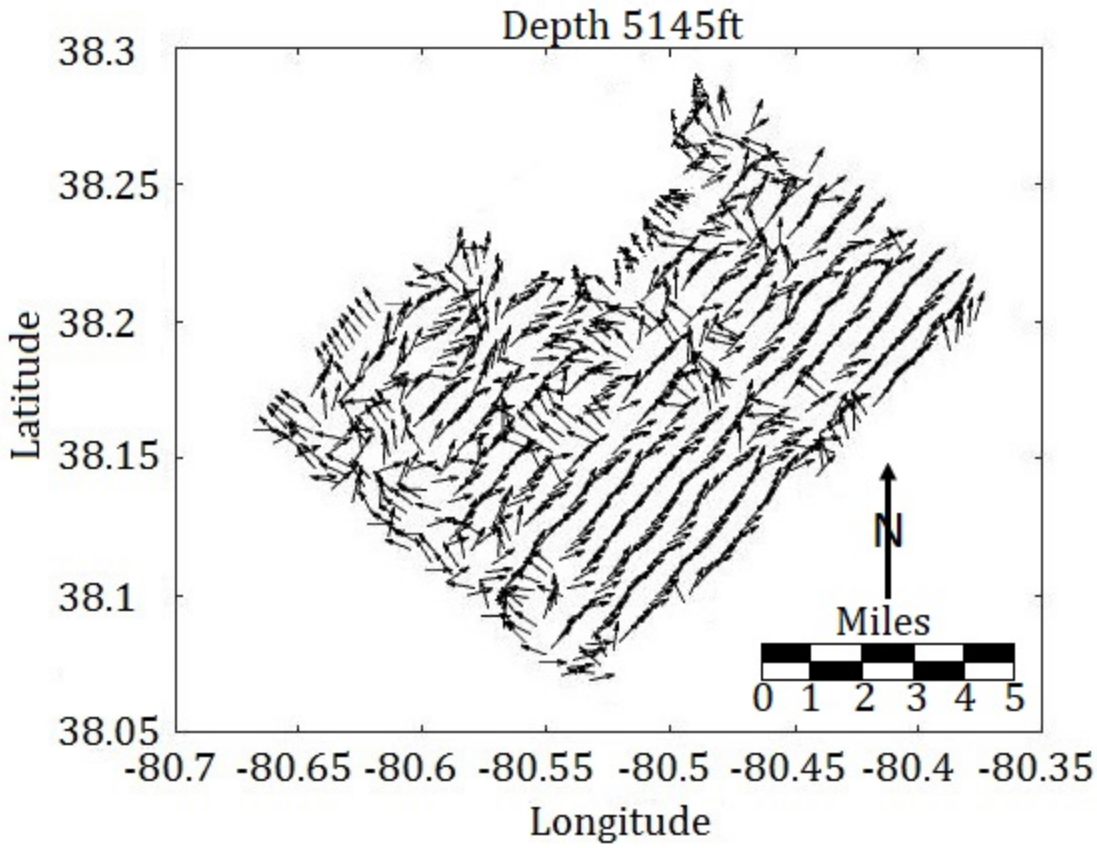

Figure 28: Azimuth of the fast direction results for a horizontal slice at a depth of 5145 ft (1568 m).

In addition to horizontal slices from the OVT azimuthal data, Figure 29 shows rose diagrams created from the azimuthal anisotropy data within the range of the lower Marcellus Formation from 3900 to 5145 ft (1189 to 1568 m). Code to generate the rose diagrams is in Appendix G. The code creates an array of azimuth measurements of the OVT anisotropy data from the zone of 3900 to 5145 ft (1189 to 1568 m), and the added azimuths that 180^{o} more than the measured azimuth for orientation emphasis. The code then using the Matlab function polarhistogram creates rose diagrams at arbitrary selected locations spaced equally across the study area for this project. The code also creates a scatter plot of the locations of the rose diagrams allowing for the creation of a more visually beneficial diagram of the rose diagrams.

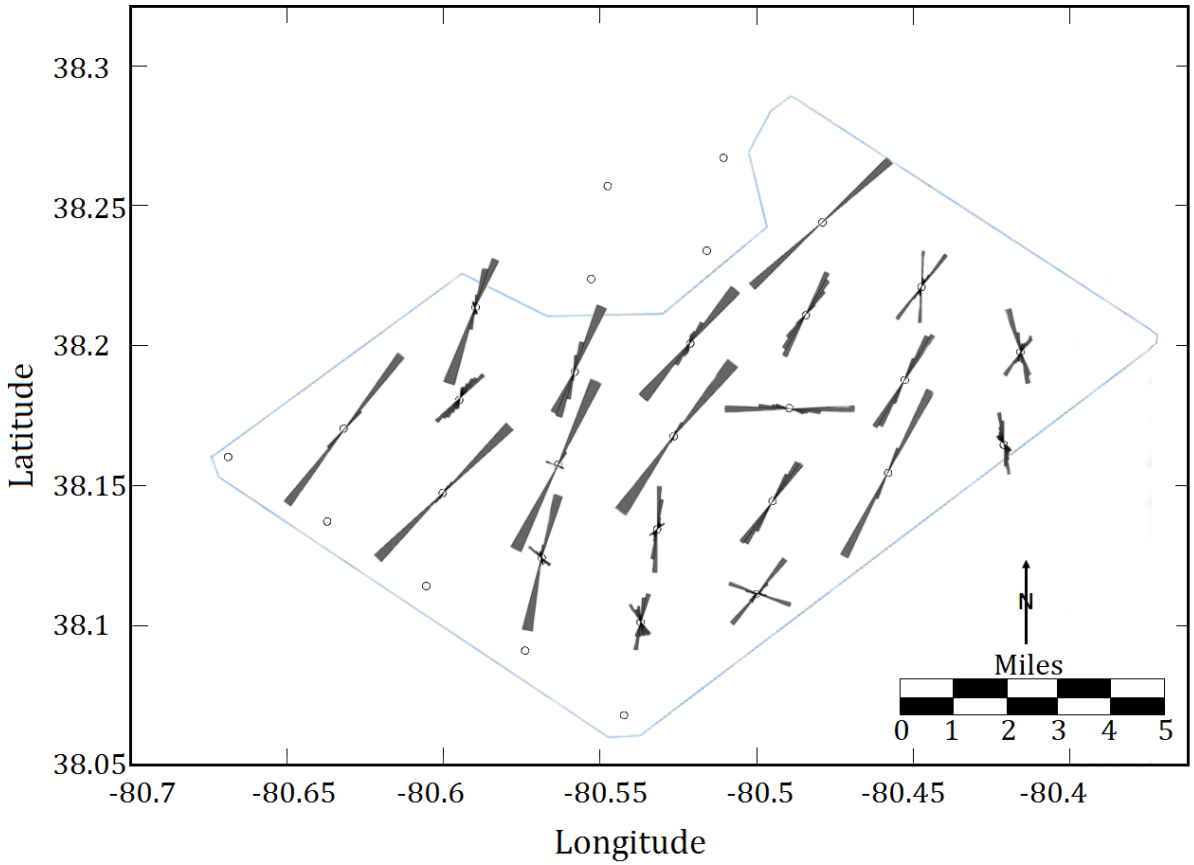

Figure 29: Rose diagrams of the fast direction of the azimuthal anisotropy data within the range of the lower Marcellus, from 3900 to 5145 ft (1189 to 1568 m). Code for generating the rose diagrams is in Appendix G.

4. Discussion

The 4350-ft-depth slices and Marcellus horizon attributes calculated on the data have varied ability to highlight faults. A region was selected for mapping the potential location of faults from the results of each calculation to determine which produced the best results based on the number of potential faults visible within the region. The results of the mapping of these faults are in Appendix B. Of the 4350-ft-depth calculated attributes: dip azimuth, mean curvature, and dip curvature provided the best results for locating faults. Each of these attributes highlights the major faults within the region. The results of dip azimuth are highly effective at emphasizing the orientation of features across the region; the results of this attribute show an orientation of NE-SW of the regional features. Of the curvature attributes, the mean curvature and dip curvature results show the greatest apparent detail of the region. Results of these calculations highlight regional faults, as well as more subtle features and their orientations across the region.

The results of the semblance, dip-steered semblance, minimum curvature, maximum curvature, most positive curvature, and most negative curvature show the regions of major faulting, but are not as effective at highlighting faults as dip azimuth, mean curvature, and dip curvature. In addition to the overall fault trend in the NE-SW direction, two NW-SE trending faults appear in the results of the curvature, semblance, and dip-steered semblance calculations.

Attributes such as median, trace mix, trace mix triangulation, strike curvature and similarity are not as useful; while this group of attribute can locate some faults, they do no produce results capable of determining many fault locations. The Gaussian curvature results show no ability to locate faults in this study.

While the attribute slices have a better ability to map major fault locations, the horizon attributes have the ability to identify smaller faults more specific to the formation of interest.

Similar to the attribute slice calculations, attribute results were judged based on the number of visible potential faults within a selected region. The results of the mapping of these faults within a region are in Appendix C.

Overall, the dip curvature attribute calculation provided the most useful results for the horizon attributes. In addition, the results of the calculations of mean, maximum, minimum, most positive, and most negative curvature on the lower Marcellus horizon showed good results. The result of the dip curvature calculation along the horizon shows the most fault information, including location and orientation, of the horizon attributes. Dip curvature shows a clear orientation of faults in the NE-SW direction.

The rose diagrams created from the results of the mean curvature horizon attribute show similar trends as the rose diagrams created from the azimuth of fast velocity of the zone of the Marcellus. The rose diagrams from region 1 (Figure 25) differ slightly but still have similar orientations. Figure 30 shows the results of the azimuths from the azimuthal anisotropy data, the azimuths from the lineaments taken from the mean curvature attribute calculated on the lower Marcellus horizon, and the azimuths from the microseismic study on the Rupert 3, 4, and 7 wells combined for region 1. The results of the azimuths from the horizon attribute and the microseismic portray similar results of azimuths between N 30^{o} E (S 210^{o} W) and N 60^{o} E (S 240^{o}W), while the azimuths from the velocity anisotropy range from 0^{o} to N 30^{o} E (S 210^{o} W). The general trend of the azimuths from each method still has the general trend of Northeast-Southwest orientation. The azimuth from velocity anisotropy azimuths are from a depth range of 3900 to 5145 ft (1189 to 1568 m) that encompasses the lower Marcellus.

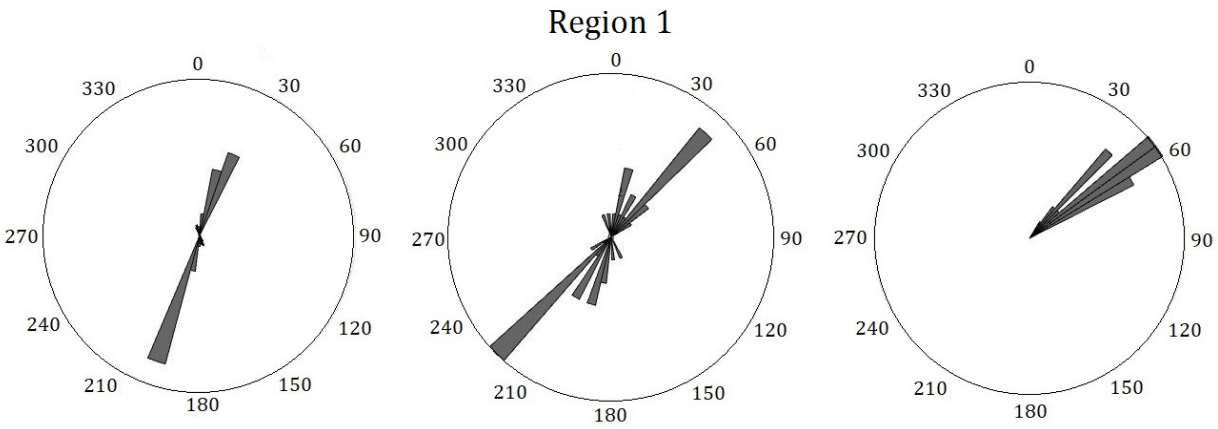

Figure 30: Comparison of the rose diagram generated from velocity anisotropy (left), the results of azimuths taken from the mean curvature calculation completed on the lower Marcellus horizon (middle), and the combined results of the microseismic study on the three wells in the region (right) for region 1 from Figure 25.

The results of the velocity anisotropy and the azimuths from the mean curvature of region 2 (Figure 25) correlate more closely with azimuths averaging around N 30º E (S 210º W). Figure 31 shows a comparison of the results from the velocity anisotropy, and the lineament azimuths from the mean curvature attribute calculation for region 2.

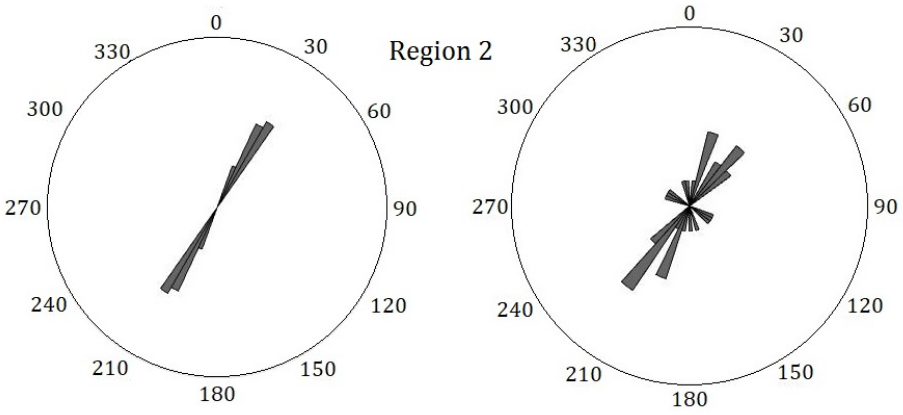

Figure 31: Comparison of the rose diagrams generated from the velocity anisotropy (left) and the results of azimuths taken from the mean curvature calculation completed on the lower Marcellus horizon (right) for region 2 from Figure 25.

Region 3 (Figure 25) has azimuths of mainly N 15º E (S 195º W) and N 45º E (S 225º W), the anisotropy azimuths are N 35º E (S 205º W) and N 105º E (S 285º W). The region 3

results show a similar trend in the NE-SW direction, but do not show the trend that occurs in the NW-SE direction that appears in the velocity azimuth data. Figure 32 shows the comparison of results from the velocity anisotropy azimuths and azimuths taken from the results of the mean curvature attribute calculation for region 3.

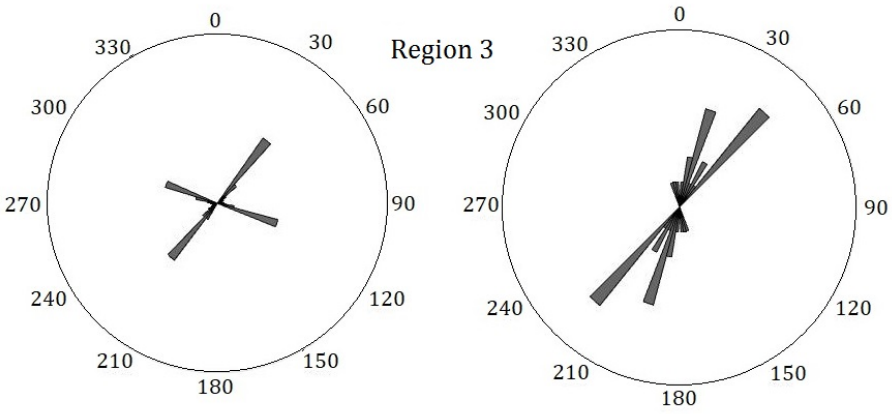

Figure 32: Comparison of the rose diagrams generated from the velocity anisotropy (left) and the results of azimuths taken from the mean curvature calculation completed on the lower Marcellus horizon (right) for region 3 from Figure 25.

Region 4 (Figure 25) has a range of azimuths from 0º to N 45º E (S 225º W), but the velocity azimuth results show a strong trend at approximately N 25º E (S 205º W). Figure 33 shows the results of the rose diagrams generated from the velocity anisotropy, and the azimuths of lineaments taken from the mean curvature attribute calculation.

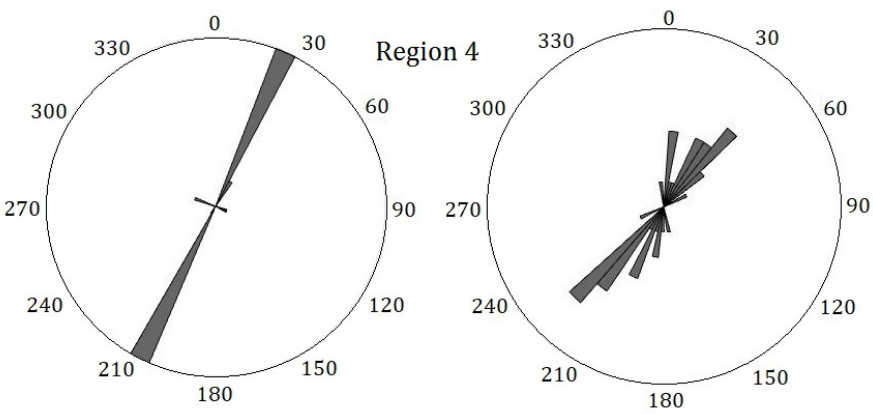

Figure 33: Comparison of the rose diagrams generated from the velocity anisotropy (left) and the results of azimuths taken from the mean curvature calculation completed on the lower Marcellus horizon (right) for region 4 from Figure 25.

Region 5 (Figure 25) has a range of azimuths from 0° to N 30° E (N 210° W), with another smaller trend in the N 300° W (S 120° E) orientation. The velocity azimuth data shows a similar trend in orientation of NE-SW; however, the main azimuth is at N 50° E (S 230° W). Figure 34 shows the comparison of the results from the azimuthal velocity anisotropy data, and the azimuths from lineaments taken from the mean curvature calculation on the lower Marcellus.

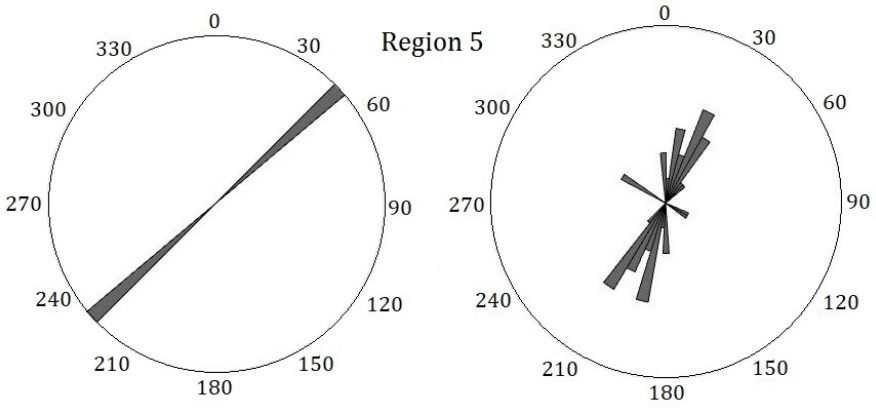

Figure 34: Comparison of the rose diagrams generated from the velocity anisotropy (left) and the results of azimuths taken from the mean curvature calculation completed on the lower Marcellus horizon (right) for region 5 from Figure 25.

The azimuthal velocity anisotropy results do not show clear fault locations, as the attribute calculations are capable of providing. The anisotropy results, do however, show

agreement with the attribute calculations because the azimuthal fast direction of velocity is similar in orientation to the orientation of the faults. The orientations of faults from attribute slices at 3900 ft, 4350 ft, and 5140 ft (1189 m, 1326 m, and 1566.7 m) correlate with the azimuthal fast direction from the anisotropy slices at the same depths. Figure 35 shows the azimuthal fast direction from anisotropy at 4350 ft (1326 m) overlain on mapped faults from the mean curvature attribute calculation also at 4350 ft (1326 m).The orientations of major faults from the mean curvature 4350-ft-depth calculation are in agreement with the orientations of the azimuthal fast direction from the anisotropy analysis.

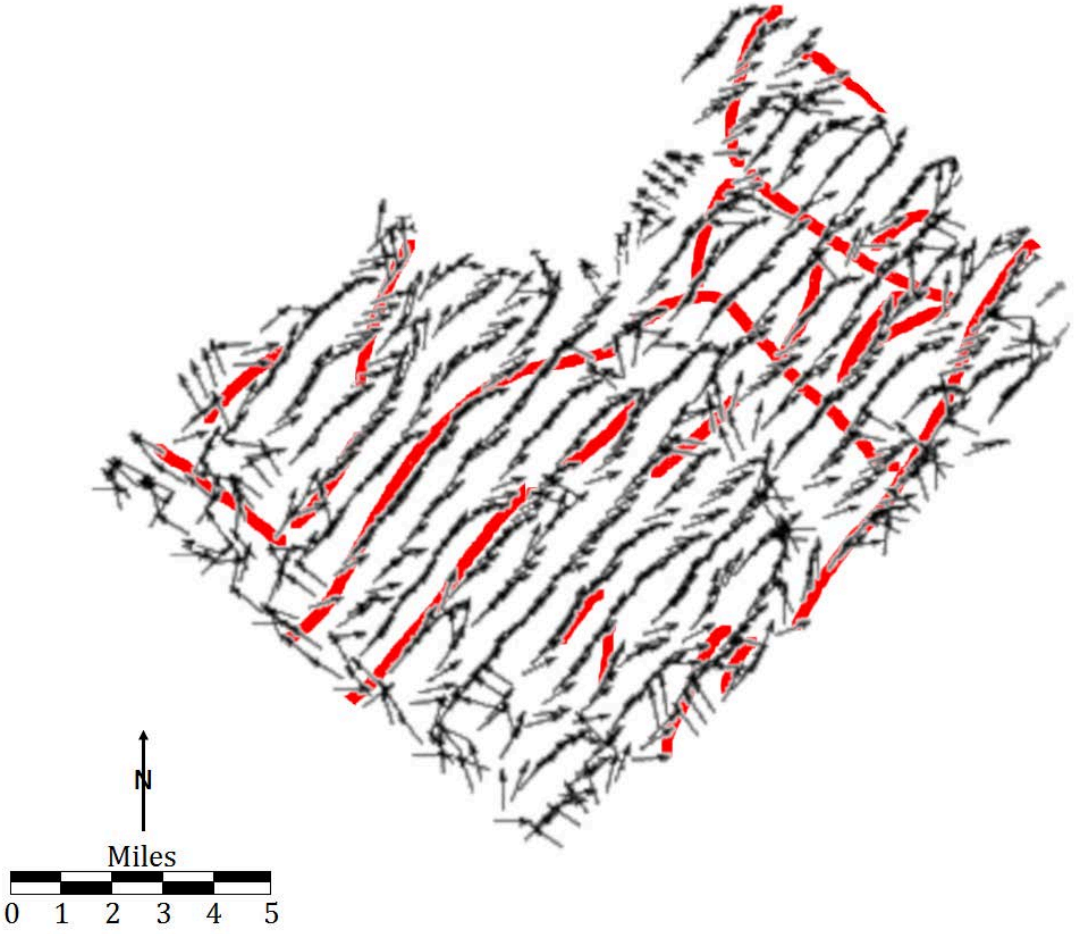

Figure 35: The anisotropy map at 4350 ft (1326 m) overlain on the major faults at 4350 ft (1326 ft). Fault locations were mapped from the results of the mean curvature attribute calculation. Orientations from the faults shown by the results of the mean curvature calculation agree with the azimuthal anisotropy orientation.

5. Conclusions

For the 4350-ft-depth calculated attributes, the dip azimuth, mean curvature, and dip curvature attributes provided the most information of faults and their orientations. These attributes were capable of highlighting the potential location and orientation of faults in the study area. The results of dip azimuth clearly show orientations across the region with an overall trend in the NE-SW direction. The mean curvature results show the major faults, as well as more subtle faults that are not as clear as the results of the other curvature calculations. Dip curvature results show the most fault information, showing the most potential fault locations across the region. The 4350-ft-depth attribute calculations are also capable of highlighting two NW-SE trending faults.

For the attributes calculated directly along the lower Marcellus horizon dip curvature provided the most fault and orientation information. Dip curvature emphasizes the orientation of faults trends within the region, showing faults tend to have a NE-SW orientation. The results also clearly show the most potential fault locations. Mean curvature results on the horizon also show fault information, though not in as much detail as the dip curvature. Dip and mean curvature show the most fault information along the lower Marcellus, and show more formation specific detail of the lower Marcellus than the 4350-ft-depth attributes. The two NW-SE trending faults do not appear as clear on any of the horizon attribute calculations as from the 4350-ft-depth results.

The results of the azimuthal velocity anisotropy rose diagrams and the horizontal slices does not provide results capable of determining fault locations, but do provide overall fault orientation. The anisotropy data results show the orientation of faults in the NE-SW direction

across the study area of this project. The result of these data was able to supplement the result of the attribute calculations by showing agreement with the orientations of faults.

Due to the anisotropy's inability to locate faults independently, attribute calculations are the preferred primary method of fault location. The mean curvature, dip azimuth, and dip curvature attribute calculations provide the overall best results for fault location. The 4350-ft-depth attribute calculations, horizon attribute calculations, and azimuthal velocity anisotropy data all are in agreement of faults trending in the NE-SW direction overall.

6. References Cited

Abousetta, A., M. Abdulla, S. Barni, D. Pandolfi, J. Michel, and B. Roure, 2016, Fracture characterization by seismic anisotropy analysis at Awali anticline structure basin: a case study: Presented at the Abu Dhabi International Petroleum Exhibition & Conference, SPE.

Al Dulaijan, Khaled, 2017, Inversion of azimuthal velocity and amplitude variations for seismic anisotropy: PhD Thesis, University of Calgary.

Al Dulaijan, K. and G. F. Margrave, 2015, Azimuthal velocity analysis of 3D seismic for fractures: altoment-bluebell field: CREWES Research Report, 27, 1-15.

Alalli, Abdulgader, and M. Zoback, 2018, Microseismic evidence for horizontal hydraulic fracturing in the Marcellus Shale: The Leading Edge, **37**, No. 5, 356-361.

Alaudah, Y., and G. AlRegib, 2017, A directional coherence attribute for seismic interpretation: SEG Technical Program Expanded Abstracts 2017, 2102-2106.

Allaby, M., 2008, A Dictionary of Earth Sciences: Oxford University Press.

Bahorich, M., and S. Farmer, 1995, 3-D seismic discontinuity for faults and stratigraphic features: The coherence cube: The Leading Edge, **14**, p. 1021-1098.

Barnes, A. E., 1996, Theory of two-dimensional complex seismic trace analysis: Geophysics, **61**, p. 264-272.

Calvert, A., E. Jenner, R. Jefferson, R. Bloor, N. Adams, R. Ramkhelawan, and C. St. Clair, 2008, Wide azimuthal imaging and azimuthal velocity analysis using offset vector tile prestack migration: First Break, **26**, p. 103-107.

Cardwell, D. H., 1977, Geological history of West Virginia: West Virginia Geological Survey and Economic Survey.

Chapman, M., X. Wu, L. Yang, K. Qian, H. Dai, and X. Li, 2015, Seismic shale characterization research at the Edinburgh Anisotropy Project: CSEG Recorder, **40**, No. 07, 28-30.

Cho, D., C. Coulombe, S. McLaren, K. Johnson, and G. F. Margrave, 2013, Fractured shale description using isotropic seismic analysis: Interpretation, **1**, No. 2, T199-T209.

Cholach P. Y., and D. R. Schmitt, 2003, Intrinsic anisotropy of shales: SEG Technical Program Expanded Abstracts, p. 149-152.

Chopra, S. 2011, Seismic attributes for fracture delineation. Lecture presented at CSEG Distinguished Lecture Tour.

Chopra, S., and K. Marfurt, 2006, Curvature attributes delineate subtleties: E&P, p. 72-73.

Chopra, S., and K. Marfurt, 2008, Seismic attributes for stratigraphic feature characterization: SEG Technical Program Expanded Abstracts 2008, p. 1590-1594.

Chopra, S., K. J. Marfurt, and H. T. Mai, 2009, Using automatically generated 3D rose diagrams for correlation of seismic fracture lineaments with similar lineaments from attributes and well log data: First Break, **27**, 37-42.

Dorn, G. A., and J. P. Dominquez, 2017, Post-stack attribute-based fracture characterization: A case study from the Niobrara shale: First Break, **35**, 85-89.

Englund, K. J., W. H. Gillespie, C. B. Cecil, J. F. Windolph Jr., T. J. Crawford, 1985, Characteristics of the Mississippian-Pennsylvanian boundary and associated coal-bearing rocks in the southern Appalachians: USGS Open File Report.

Enomoto, C. B., J. L. Coleman Jr., J. T. Haynes, S. J. Whitmeyer, R. R. McDowell, J. E. Lewis, T. P. Spear, and C. S. Swezey, 2011, Geology of the Devonian Marcellus Shale – Valley and Ridge Province, Virginia and West Virginia – A field trip guide book for the

American Association of Petroleum Geologists Eastern Section Meeting: U.S. Geological Survey Open-File Report.

Gargouri, M., 2012, Multicomponent 3D seismic interpretation of the Marcellus shale Bradford County, Pennsylvania: M.S. Thesis, University of Houston.

Hardeep, J., F. Qayyum, and H. Huck, 2015, Unconventional seismic attributes for fracture characterization: First Break, **33**, 101-109.

Inks, T. L., T. Engelder, E. Jenner, B. Golob, J. S. Hocum, and D. G. O'Brien, 2015, Marcellus fracture characterization using P-wave azimuthal velocity attribute: Comparison with production and outcrop data: Interpretation, **3**, No. 3, SU1-SU15.

Jones, G. and R. Roden, 2012, Fracture detection interpretation beyond conventional seismic approaches: Presented at Eastern Section Meeting, AAPG.

Kington, J. 2015, Semblance, coherence, and other discontinuity attributes: The Leading Edge, **34**, 12, 1510-1512.

Koenderink, J. J., and A. J. van Doorn, 1992, Surface shape and curvature scales: Image and Vision Computing, **10**, 8, p. 557-564.

Koesoemadinata, A., G. El-Kaseeh, N. Banik, J. Dai, M. Egan, and A. Gonzalez, 2011, Seismic reservoir characterization in Marcellus shale: 2011 Annual International Meeting, SEG, Expanded Abstracts, 3700-3704.

Marfurt, K. J., R. L. Kirlin, S. L. Farmer, and M. S. Bahorich, 1998, 3-D seismic attributes using a semblance based coherency algorithm: Geophysics, **63**, No. 4, 1150-1165.

Milici, R. C., and C. S. Swezey, 2006, Assessment of Appalachian Basin oil and gas resources: Devonian shale – middle and upper Paleozoic total petroleum system: U.S. Geological Survey Open-File Report.

Otto, B. A., 2013, Characterization of Devonian black shale depositional environments and diagenetic/catagenetic processing using nitrogen isotopes and other geochemical proxies: Ohio shale, eastern Kentucky: M.S. Thesis, University of Tulsa.

Osholake, T., J. Y. Wang, and T. Ertekin, 2011, Factors affecting hydraulically fractured well performances in the Marcellus shale gas reservoirs: 2011 North American Unconventional Gas Conference and Exhibition, SPE.

Pazzaglia, F. J., 2006, Excursions in geology and history: field trips in Middle Atlantic States: Geological Society of America.

Pinnacle, 2012, Fracture mapping results for the Rupert No. 3H ST2, 4H, and 7H ST3: Internal report for Bluescape Resources.

Pyrak-Nolte, L. J., 2007, Fracture anisotropy: The role of fracture-stiffness gradients: The Leading Edge, **26**, 9, 1124-1127.

Quantum Reservoir Impact, LLC., 2014, Review of BRC wells and production tests: Internal report for Bluescape Resources.

Roberts, A. 2001, Curvature attributes and their application to 3D interpreted horizons: First Break, **19**, 85-100.

Roden, R., T. Smith, and D. Sacrey, 2015, Geological pattern recognition from seismic attributes: Principal component analysis and self-organizing maps: Interpretation, **3**, No. 4, SAE59-SAE89.

Seisware, 2018, Seisware Help: (Version 10.0) [Program documentation].

Shin, Y., 2016, Reservoir modeling with multiple geological scenarios for deformation of reservoir structure and evolution of reservoir properties: Ph.D. Dissertation, Stanford University.

Soeder, D. J., C. B. Enomoto, and J. A. Chermak, 2014, The Devonian Marcellus Shale and Millboro Shale: Field Guides 2014, 35, P. 129-160.

Stevenson, M., 2015, The Marcellus shale: erosional boundary and production analysis, southern West Virginia, U.S.A.: M.S. Thesis, East Carolina University.

Stewart, Mike, 2013, Bluescape and Occidental Oil and Gas Mountaineer 3D: Internal report to Bluescape and Occidental.

Subrahmanyan, D., and P. H. Rao, 2008, Seismic attributes – a review: 7th Annual Conference and Exposition on Petroleum Geophysics.

Taner, M. T., F. Koehler, and R. E. Sheriff, 1979, Complex seismic trace analysis: Geophysics, **44**, No. 6, p. 1041-1063.

Tingdahl, K. M., and P. F. M. De Groot, 2003, Post-stack dip- and azimuth processing: Journal of Seismic Exploration, **12**, No. 2, 113-126.

Valler, V., J. Morante-Gout, G. Mikkelsen, J. Fruehn, and E. Jenner, 2012, Offset vector tile anisotropic tomography and PreSDM of the Hild OBC: EAGE Conference and Exhibition Incorporating SPE, EAGE.

Vermeer, G. J. O., 2002, 3-D seismic survey design: SEG, USA.

Walker, A. M., and J. Wookey, 2012, MSAT – a new toolkit for the analysis of elastic and seismic anisotropy: Computers & Geoscience, **49**, p.81-90.

Yue, L., W. Xiaowei, L. Fei, and Z. Yulian, 2016, Application of OVT processing to 3D seismic data in western China: SPG/SEG Beijing International Geophysical Conference 2016, p. 353-355.

Zagorski, W., G. Wrightstone, and D. Bowman, 2012, The Appalachian Basin Marcellus gas plays: Its history of development, geological controls on production, and future potential

as a world-class reservoir: Shale Reservoirs: Giant Resources for the 21st Century, AAPG Memoir 97, AAPG, p. 172-200.

7. Appendix A: Result of attribute calculations at a depth of 4350 ft (1326 m)

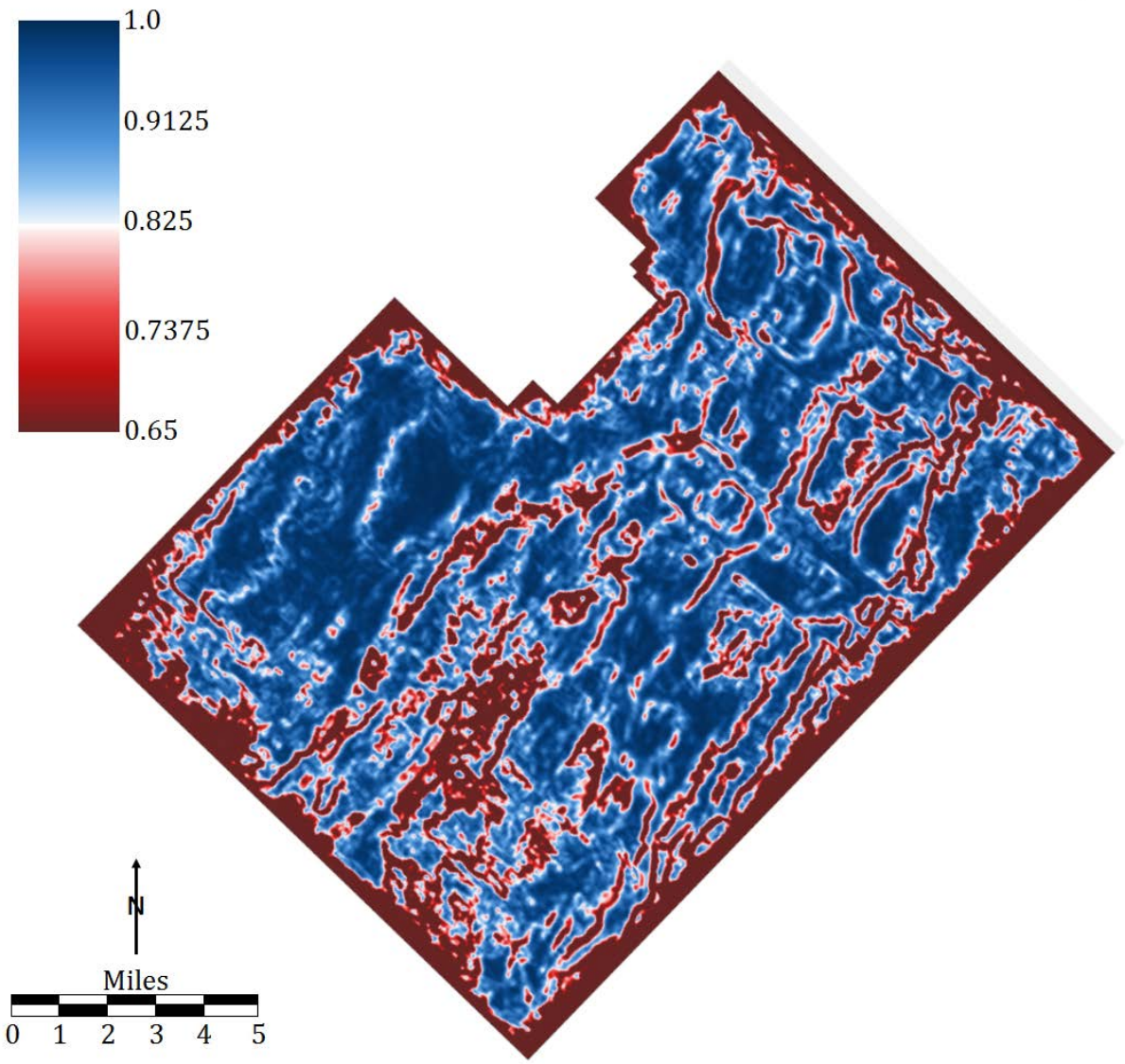

Figure 36: Results of the semblance attribute calculation at a depth of 4350 ft (1326 m).

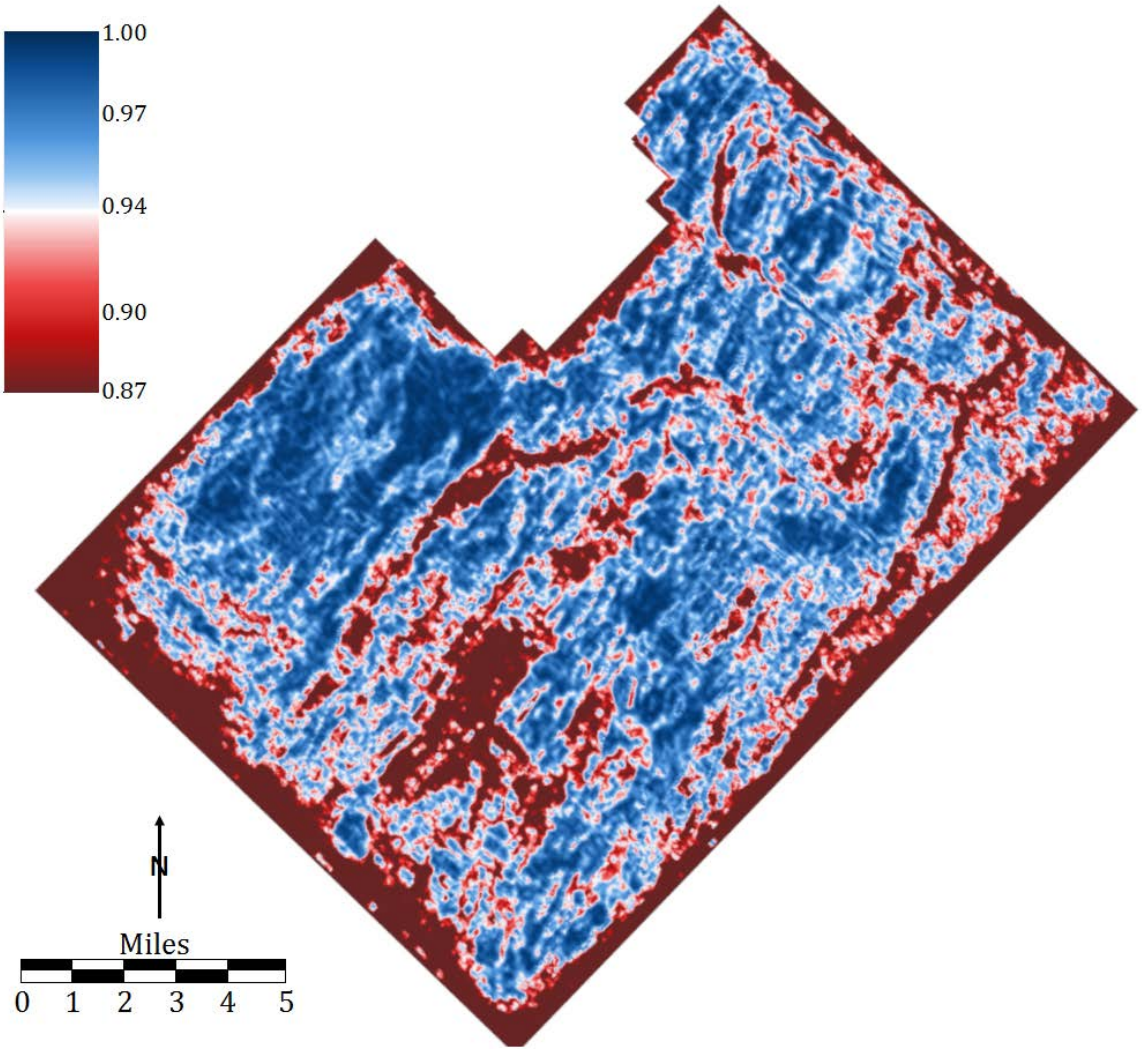

Figure 37: Results of the dip-steered semblance attribute calculation at a depth of 4350 ft (1326 m).

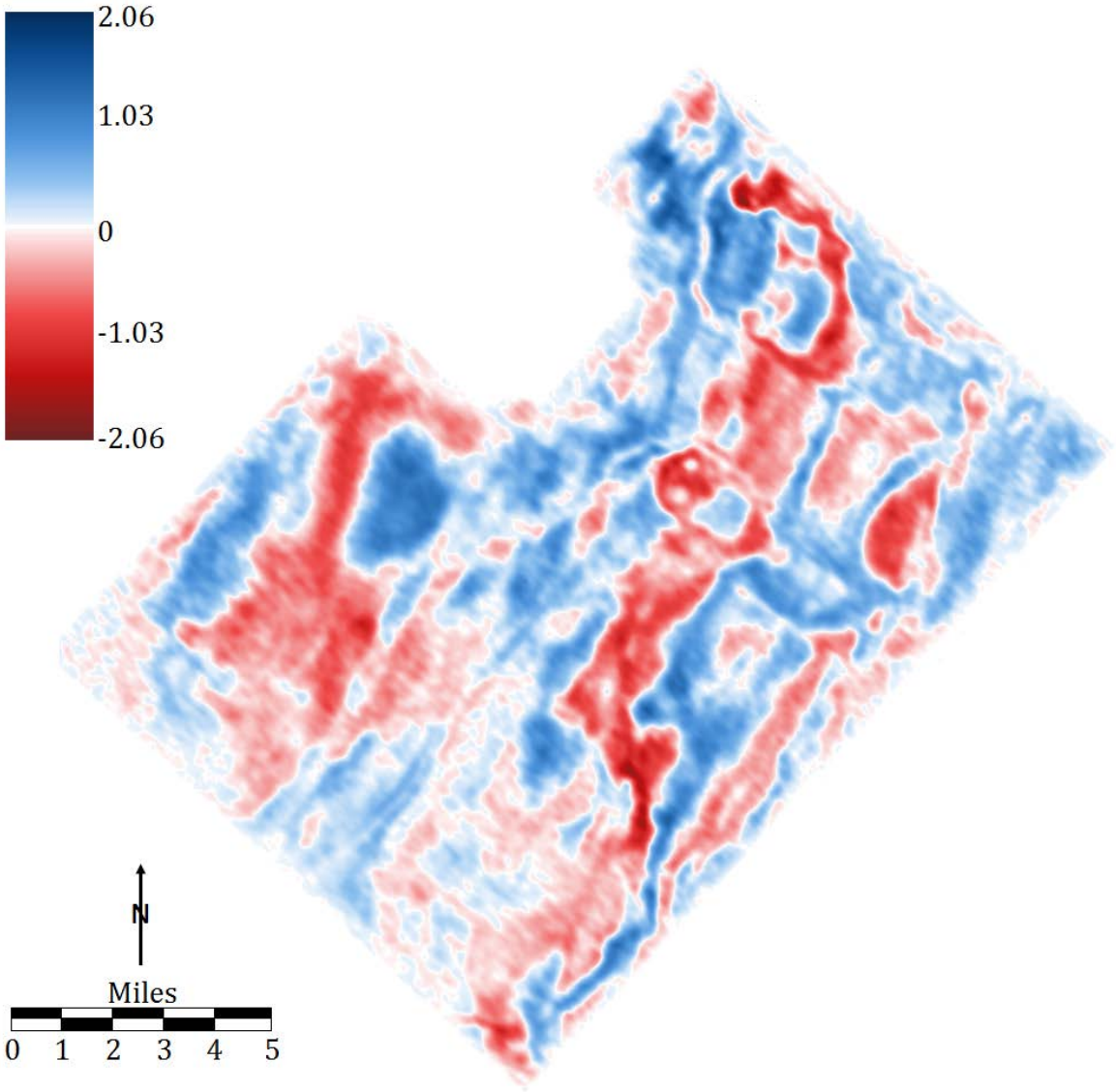

Figure 38: Results of the trace mix attribute calculation at a depth of 4350 ft (1326 m).

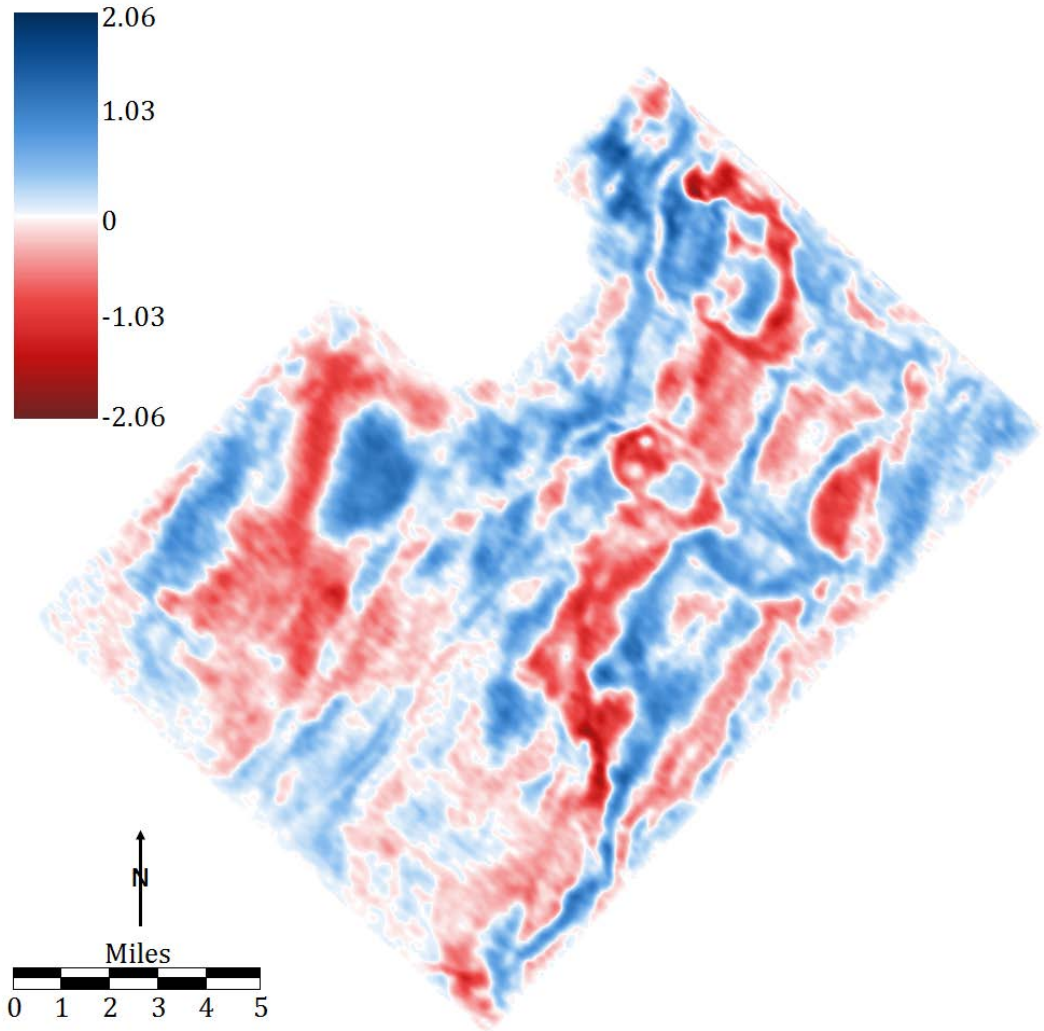

Figure 39: Results of the trace mix triangulation attribute calculation at a depth of 4350 ft (1326 m).

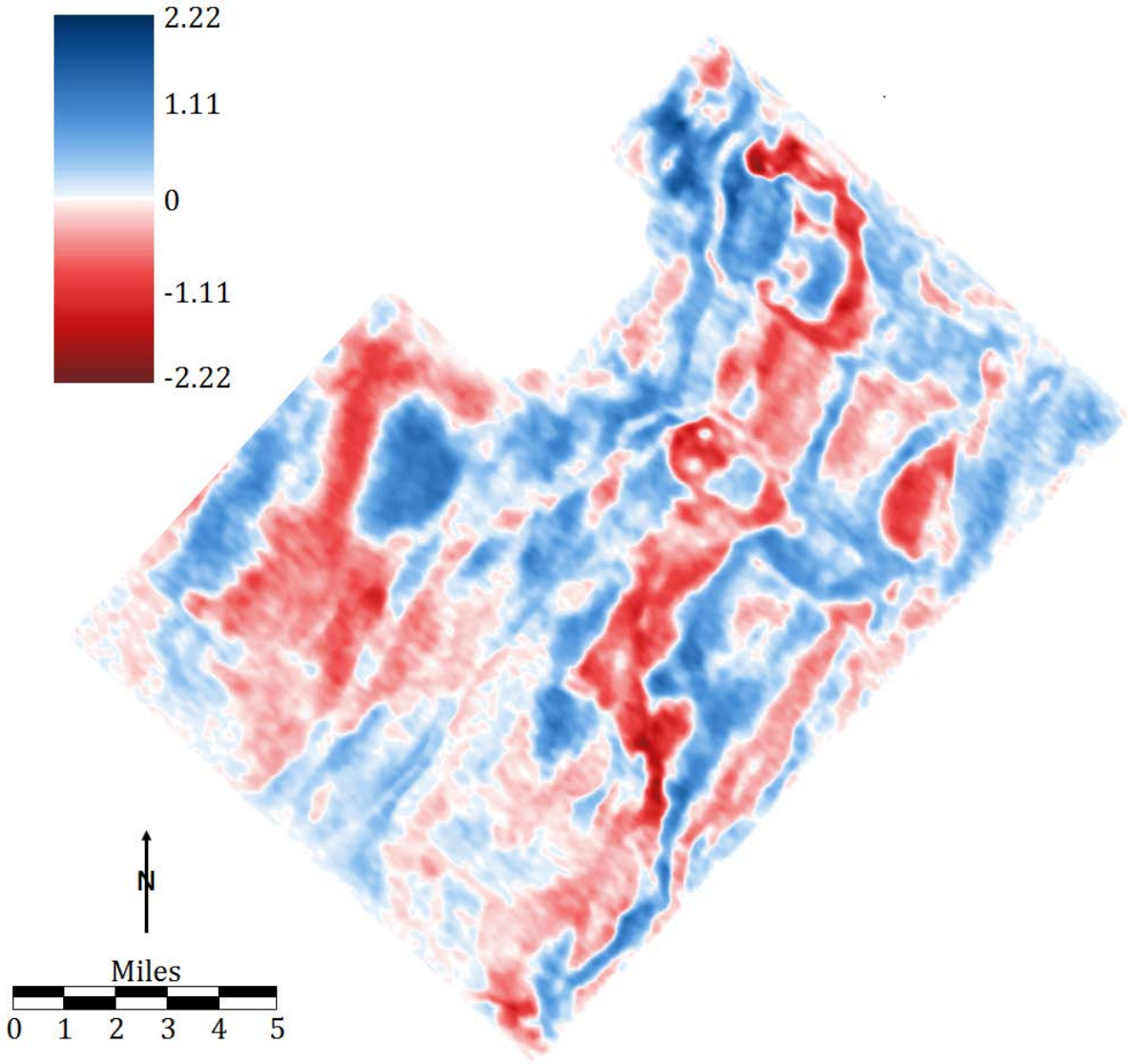

Figure 40: Results of the median attribute calculation at a depth of 4350 ft (1326 m).

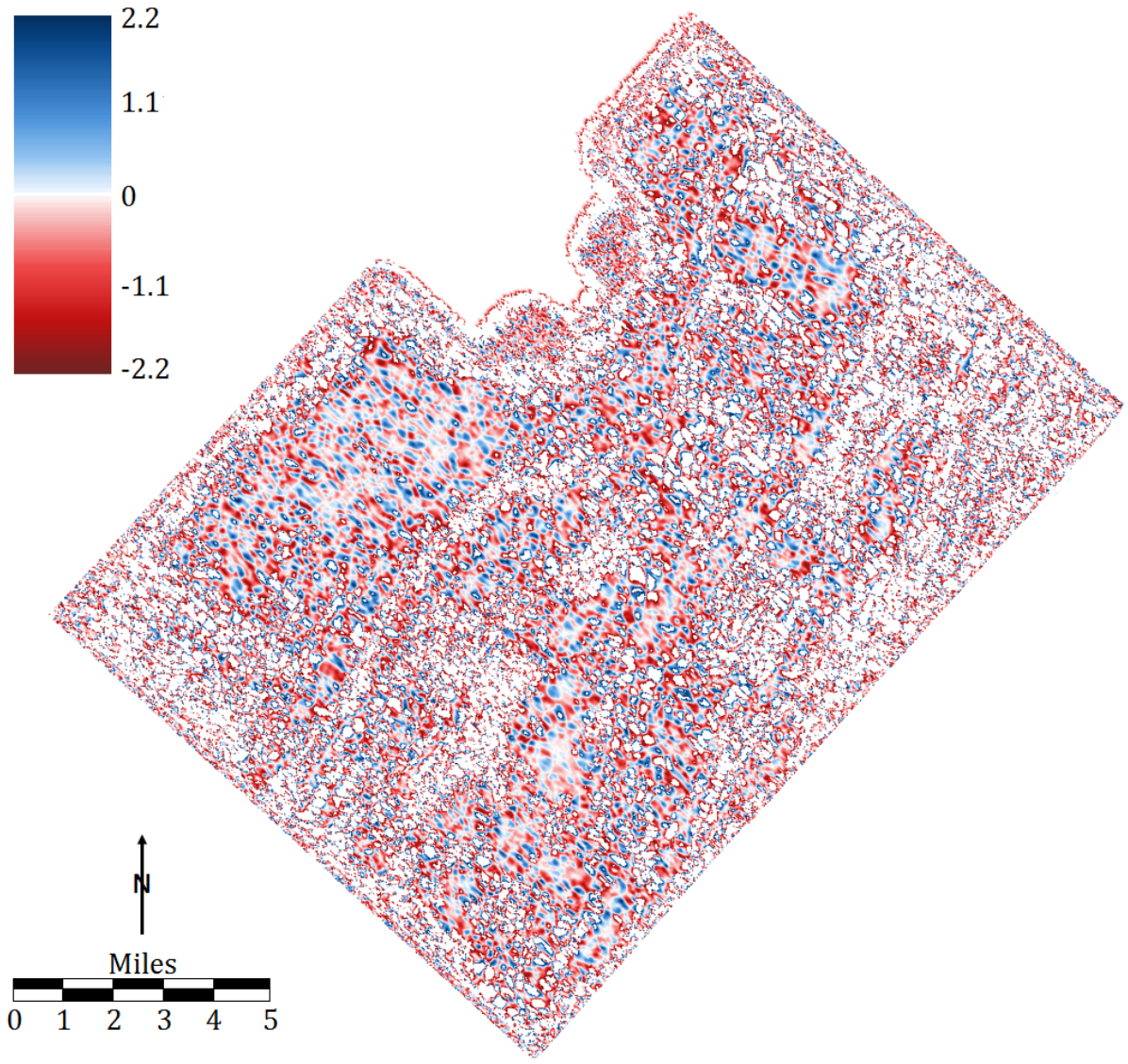

Figure 41: Results of the Gaussian curvature attribute calculation at a depth of 4350 ft (1325 m).

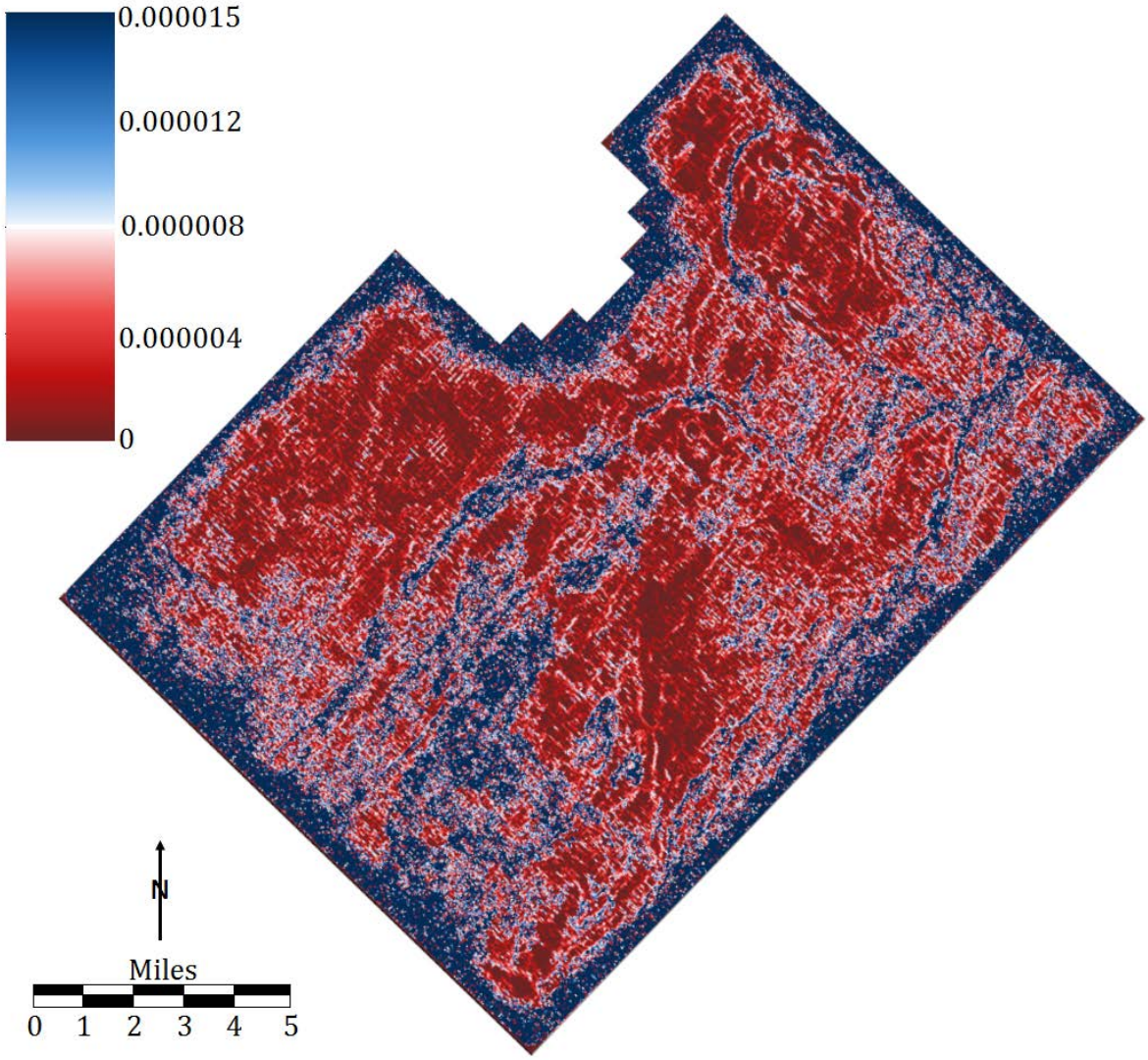

Figure 42: Results of the maximum curvature attribute calculation at a depth of 4350 ft (1326 m).

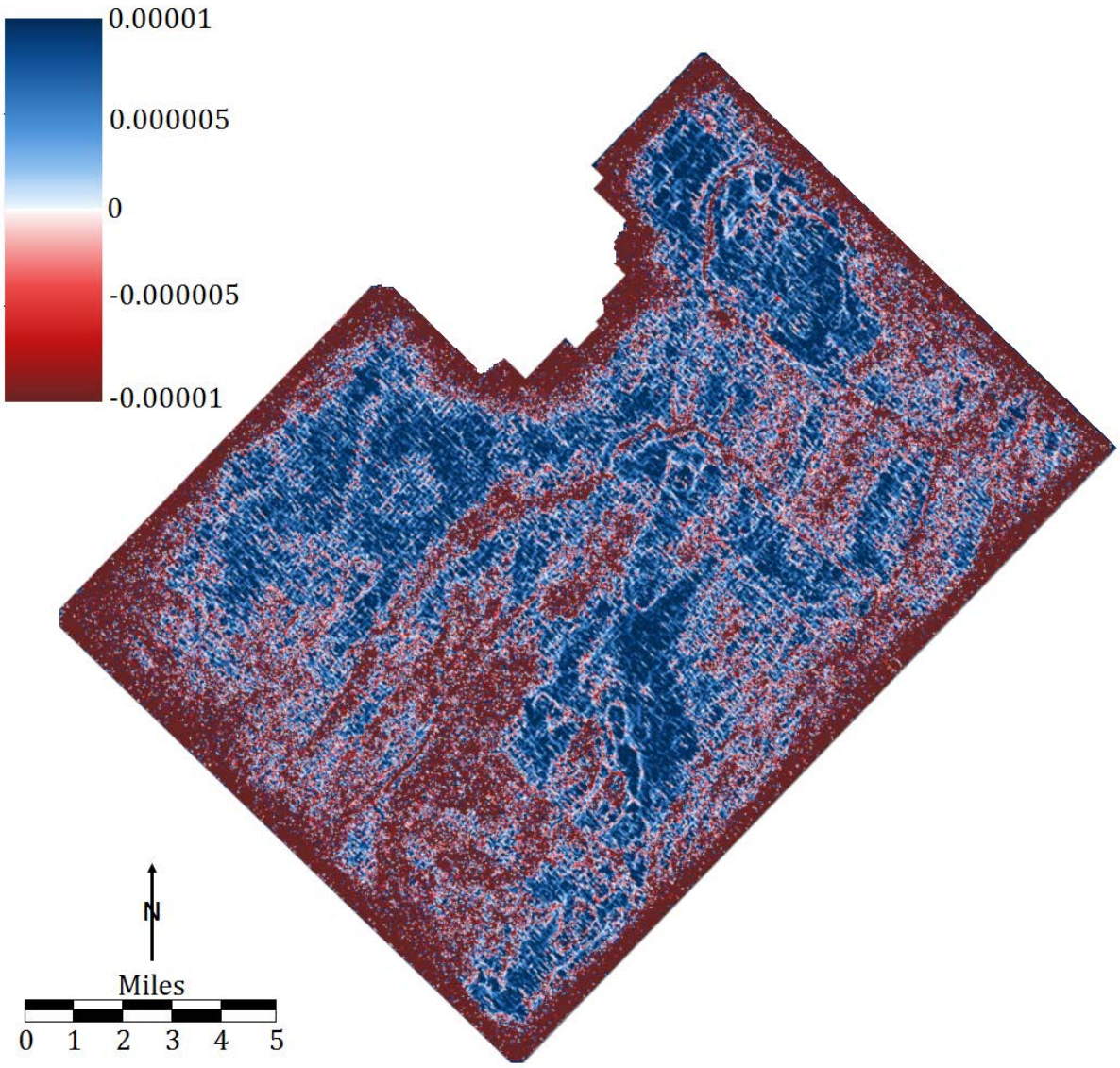

Figure 43: Results of the minimum curvature attribute calculation at a depth of 4350 ft (1326 m).

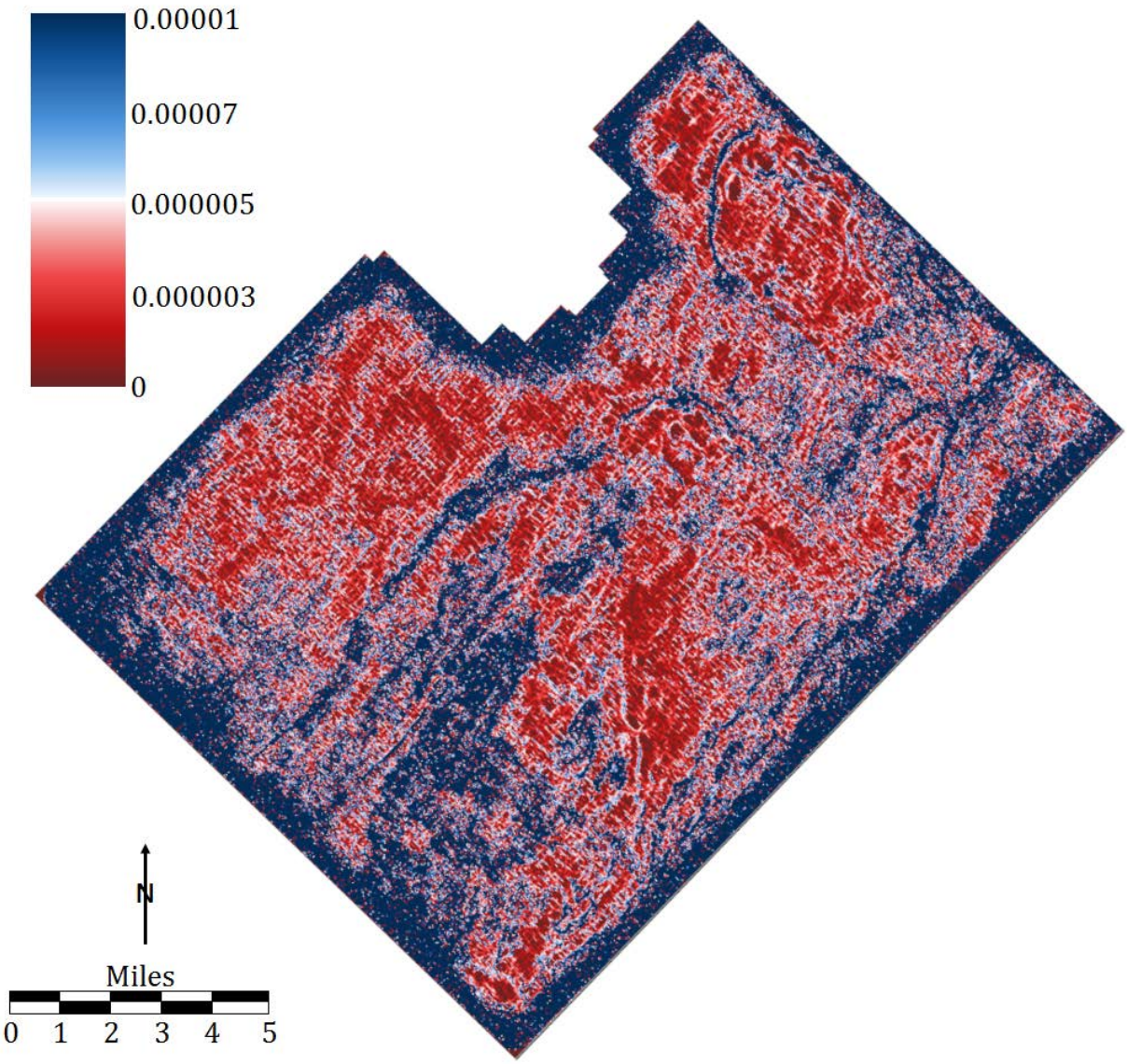

Figure 44: Results of the most positive curvature attribute calculation at a depth of 4350 ft (1326 m).

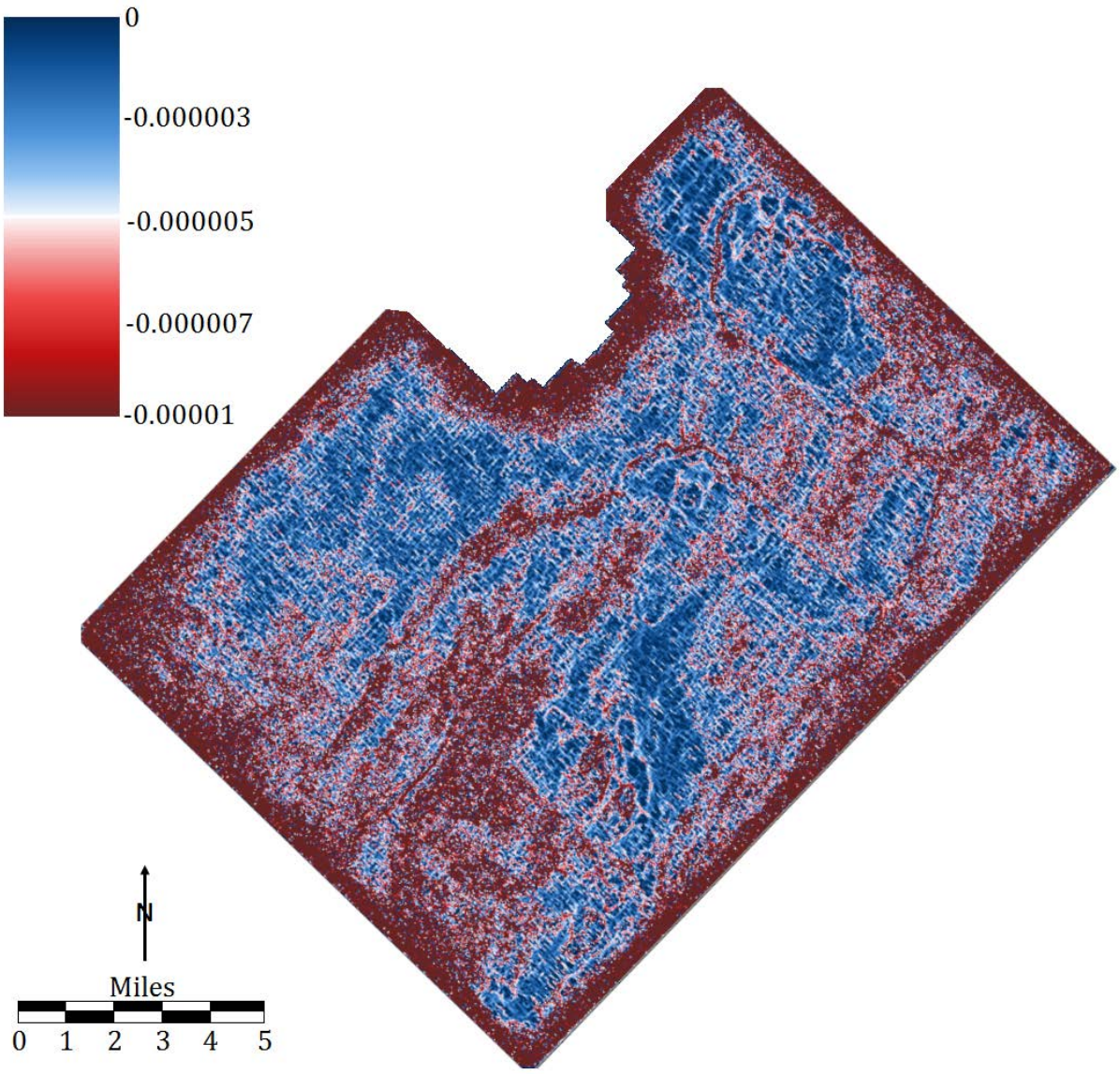

Figure 45: Results of the most negative attribute calculation at a depth of 4350 ft (1326 m).

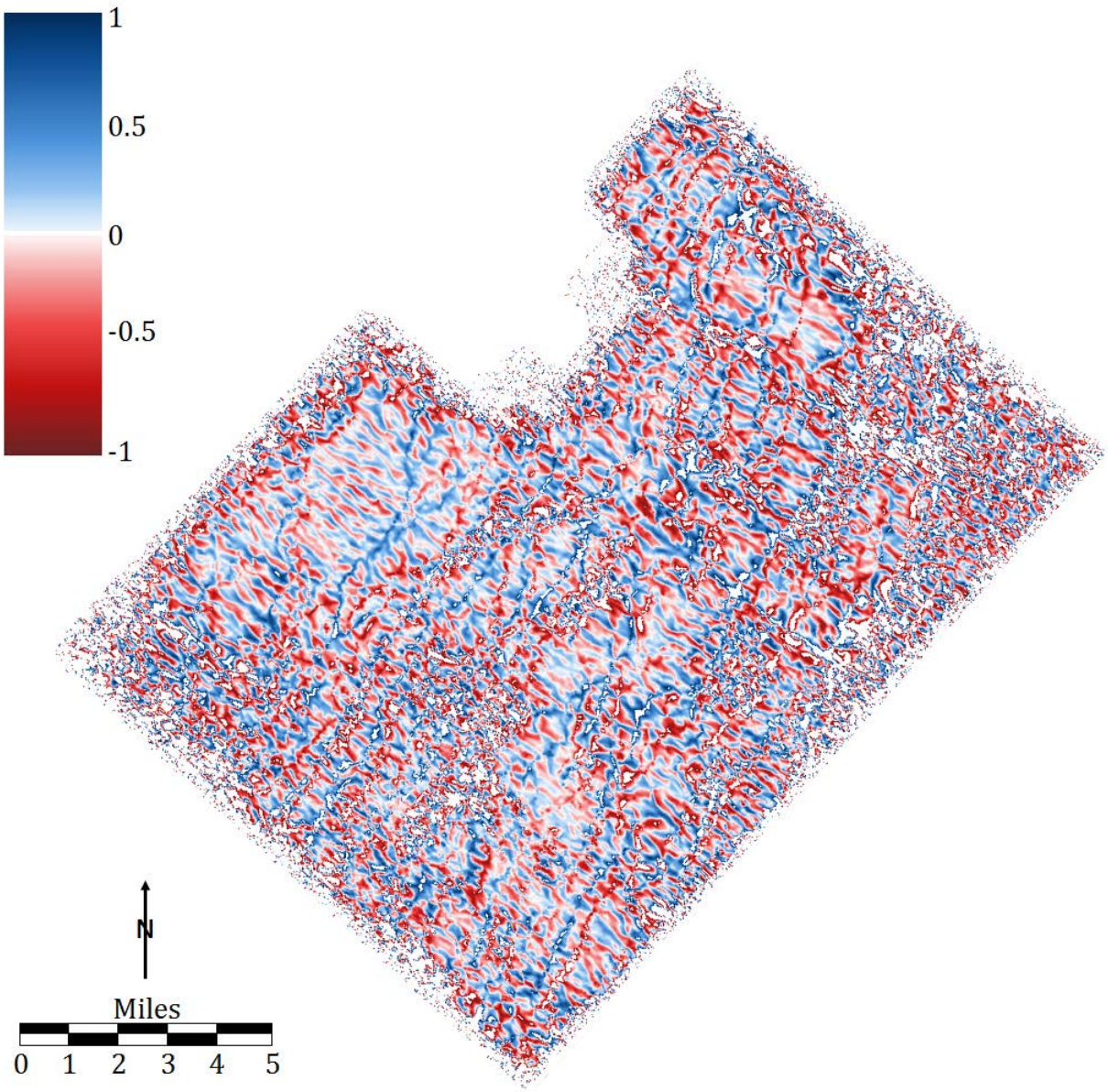

Figure 46: Results of the strike curvature attribute calculation at a depth of 4350 ft (1326 m).

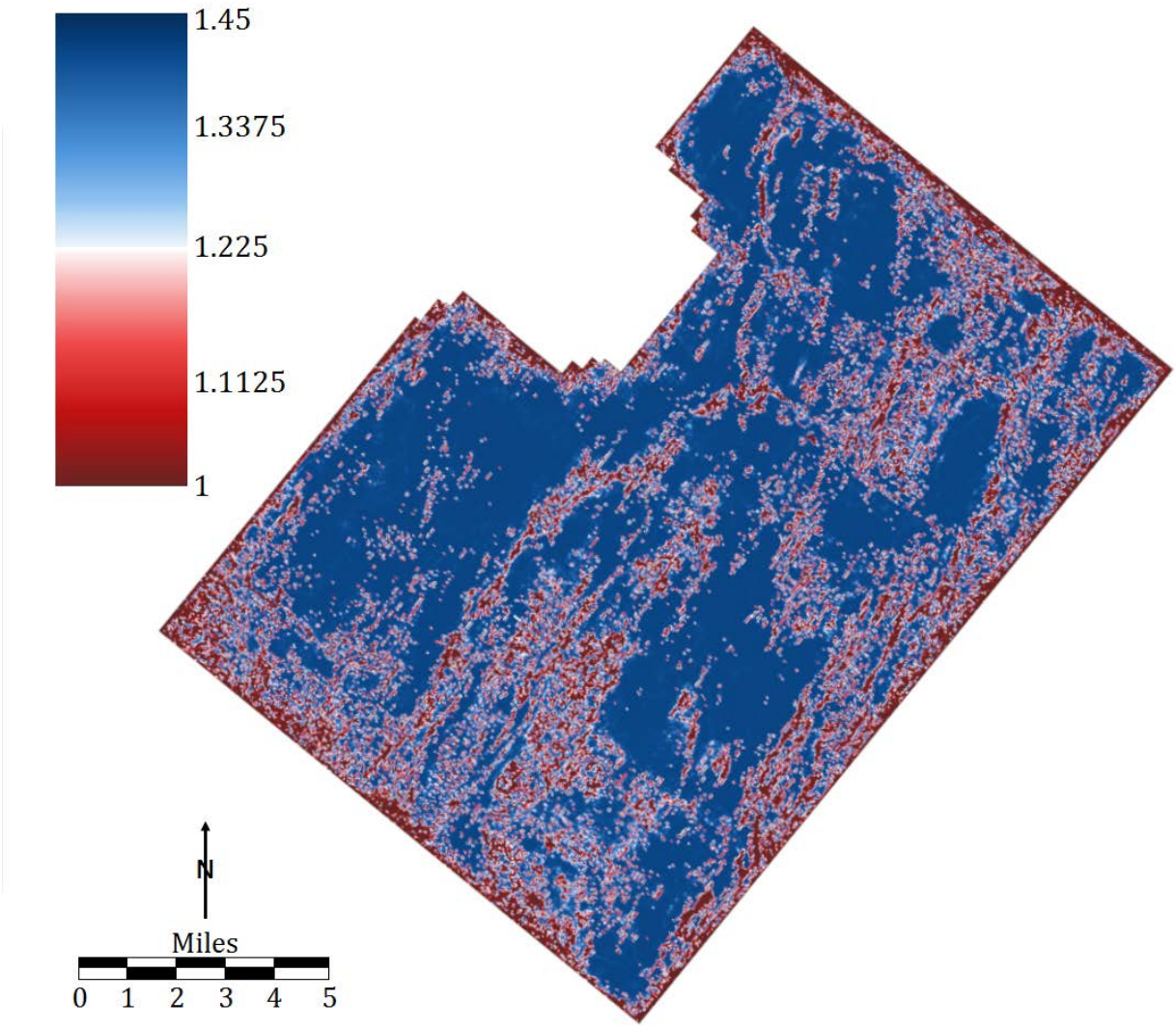

Figure 47: Results of the similarity attribute calculation at a depth of 4350 ft (1326 m).

8. Appendix B: Table of potential fault locations over a region for the 4350-ft-depth attribute calculations

Table IV: Potential fault locations over a region for each 4350-ft-depth attribute calculation used to determine which attribute results provide the clearest potential faults. Potential fault locations vary based on each attributes ability to highlight discontinuities.

Attribute Name	Attribute Results	Fault Count
Semblance	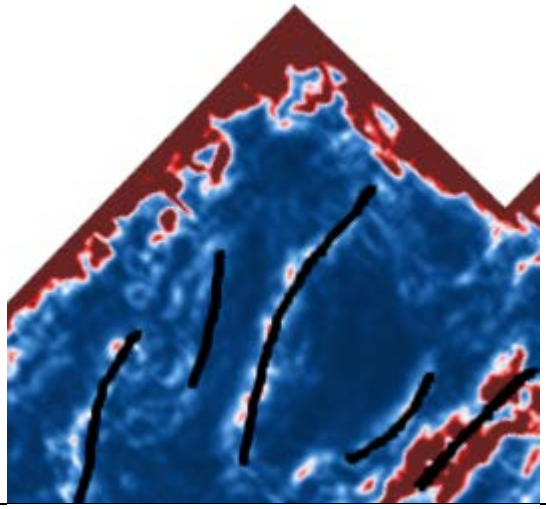	5
Dip-Steered Semblance	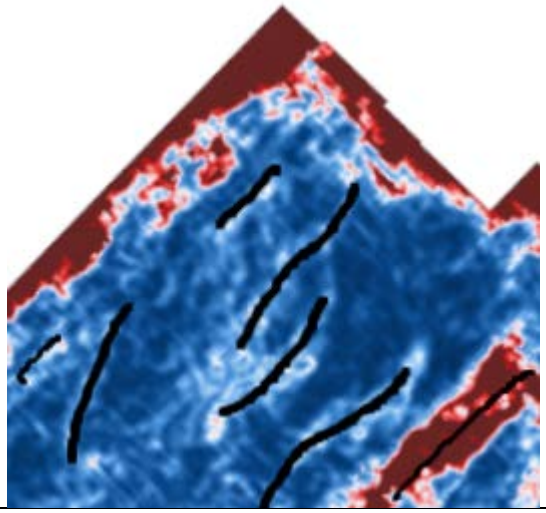	6

Trace Mix	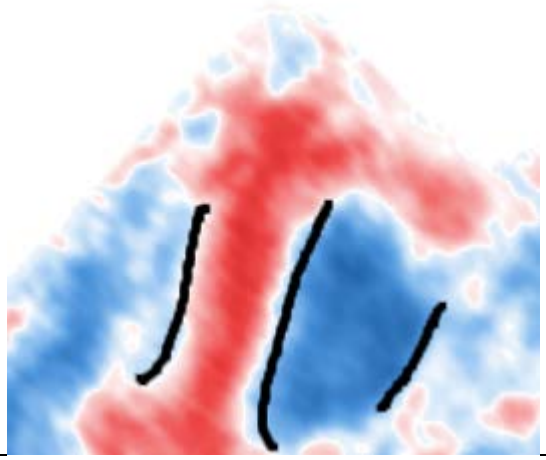	3
Trace Mix Triangulation	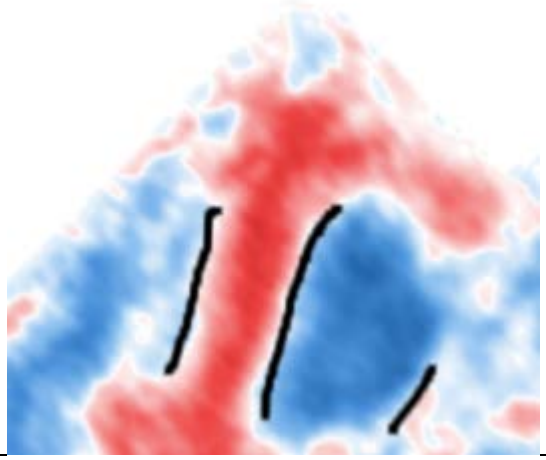	3
Median	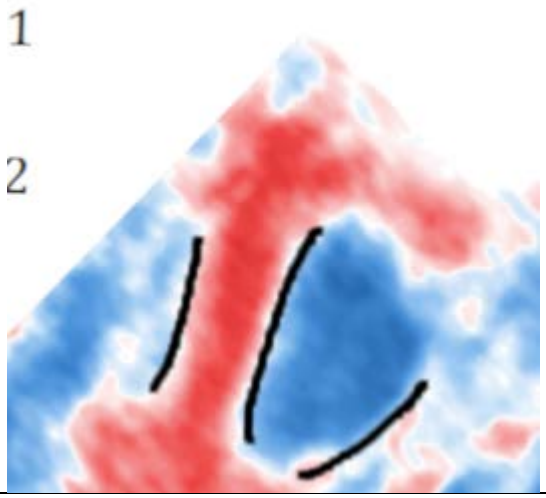	3

Dip Azimuth	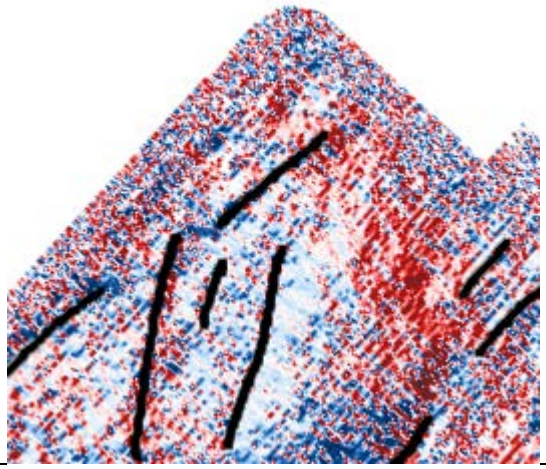	8
Mean Curvature	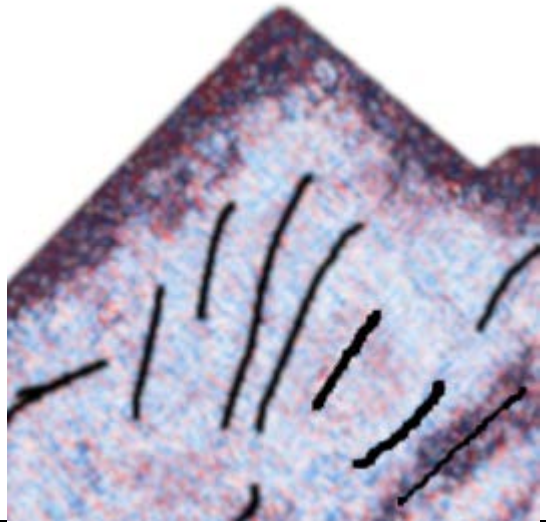	10
Gaussian Curvature	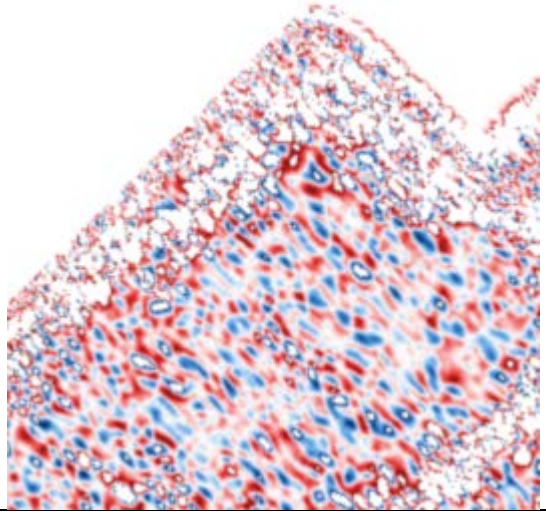	0

Maximum Curvature	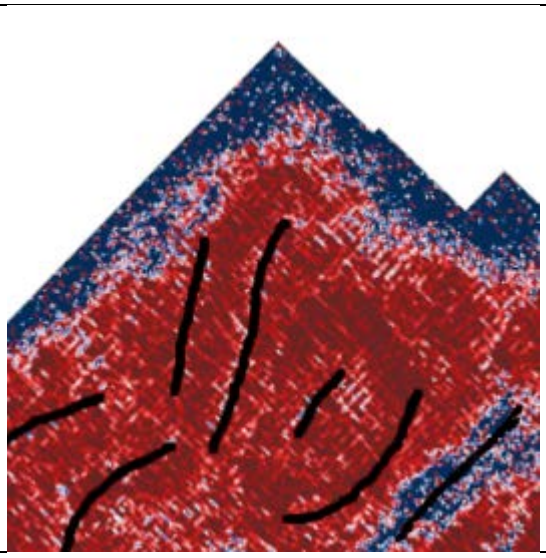	7
Minimum Curvature	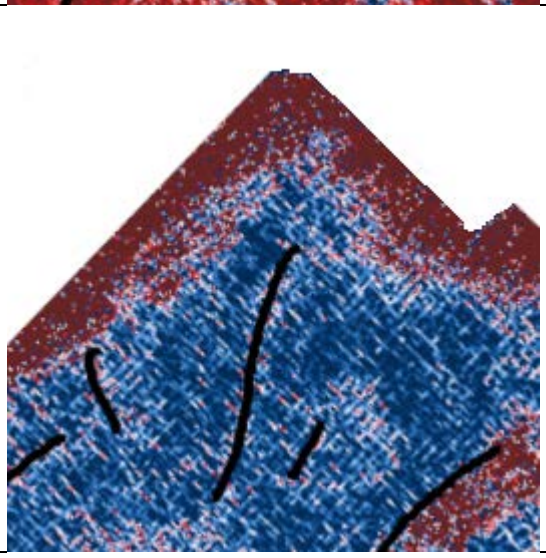	5
Most Positive Curvature		7

Most Negative Curvature	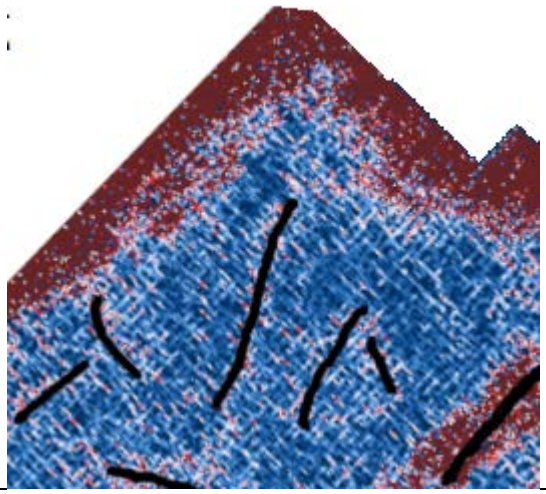	7
Dip Curvature	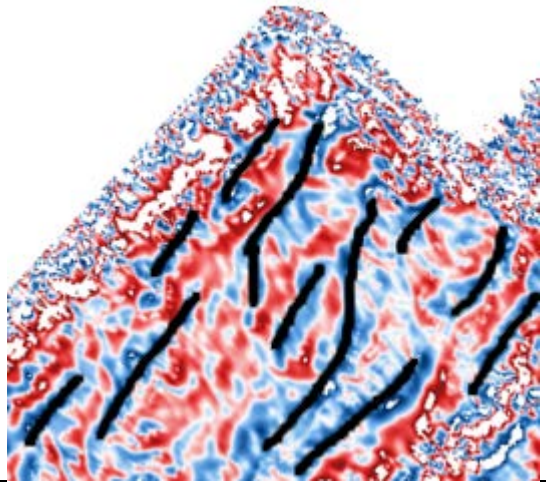	11
Strike Curvature	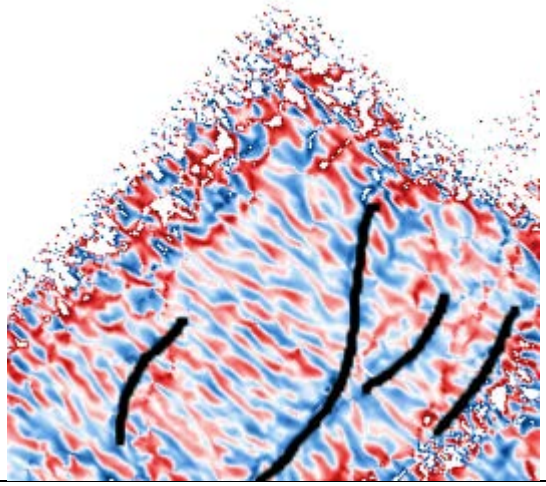	4

Similarity	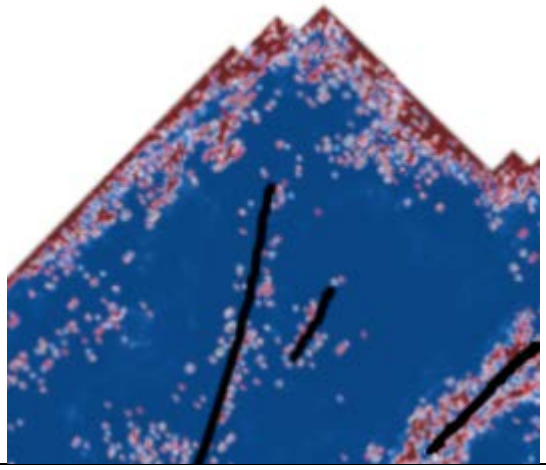	3

9. Appendix C: Table of potential fault locations over a region for the horizon attribute calculations

Table V: Potential fault locations over a region for each horizon attribute calculation used to determine which attribute results provide the clearest potential faults. Potential fault locations vary due to different methods of calculation and their ability to highlight discontinuities.

Attribute Calculation	Results	Fault Count
Azimuth	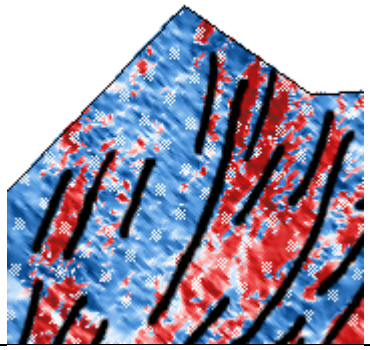	14
Dip	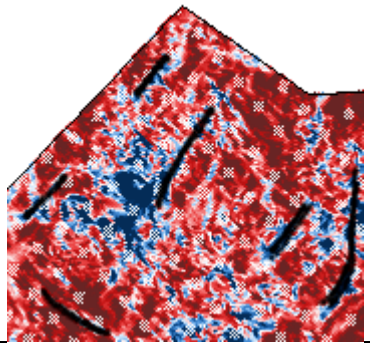	6
Mean Curvature	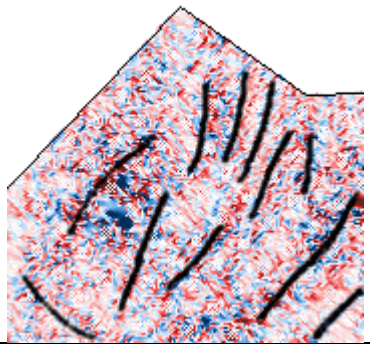	11

Gaussian Curvature	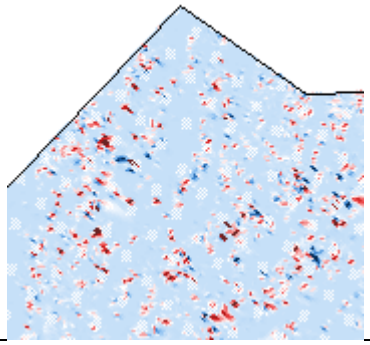	0
Maximum Curvature	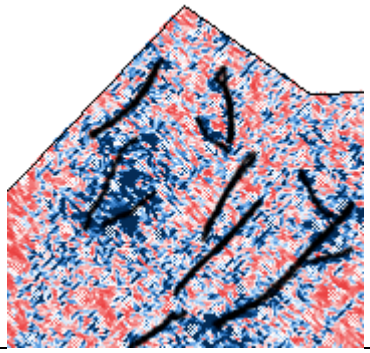	11
Minimum Curvature	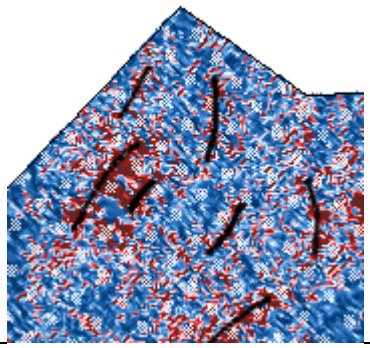	7
Most Positive Curvature	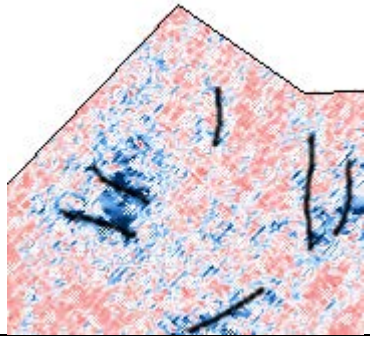	6

Most Negative Curvature	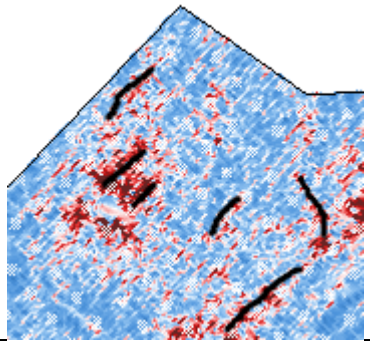	6
Dip Curvature	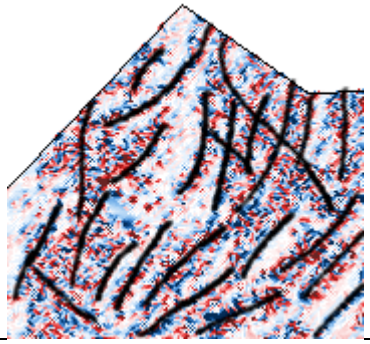	24
Strike Curvature	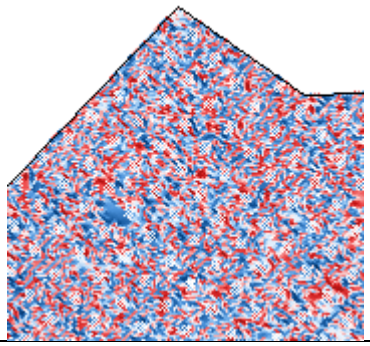	0

10. Appendix D: Results of geologic horizon attribute calculations

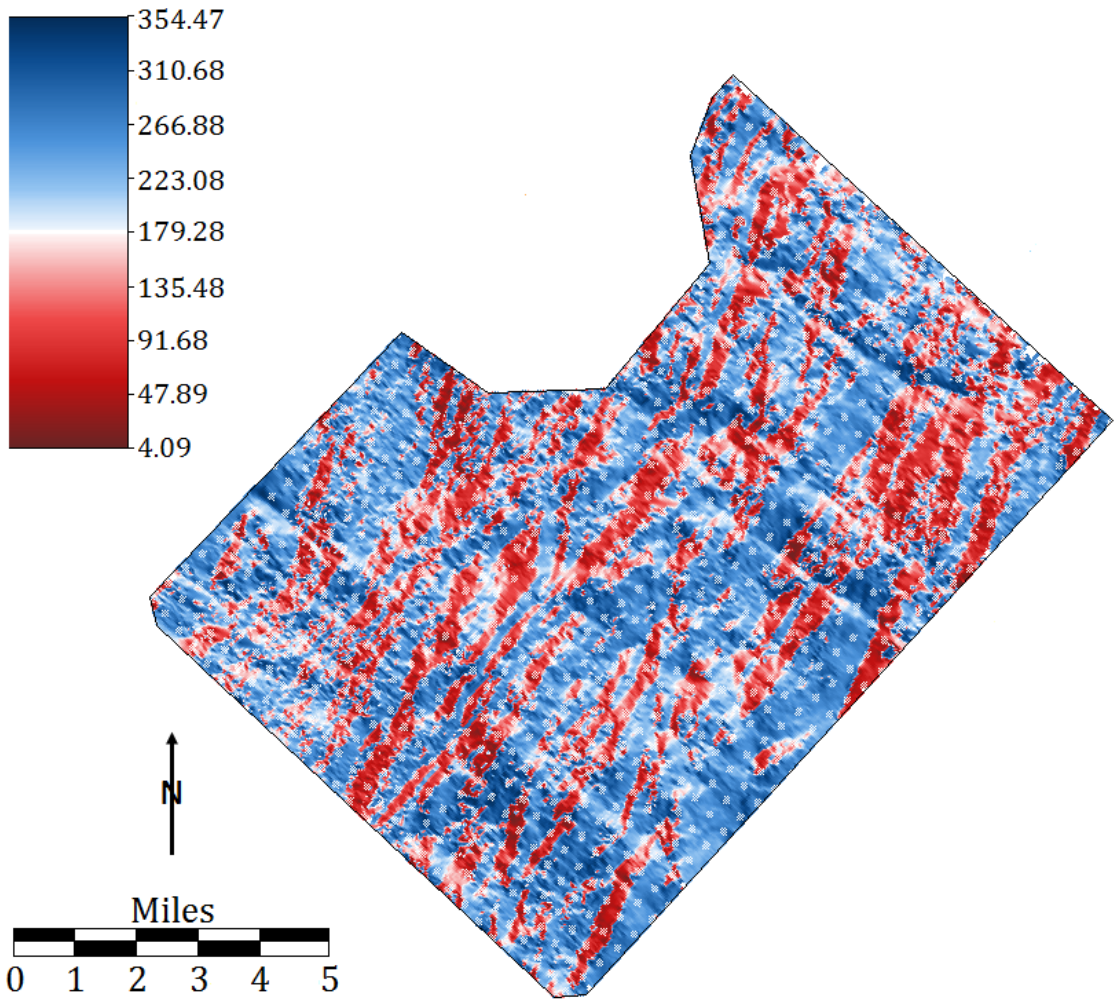

Figure 48: Results of the azimuth attribute calculation completed on the lower Marcellus horizon.

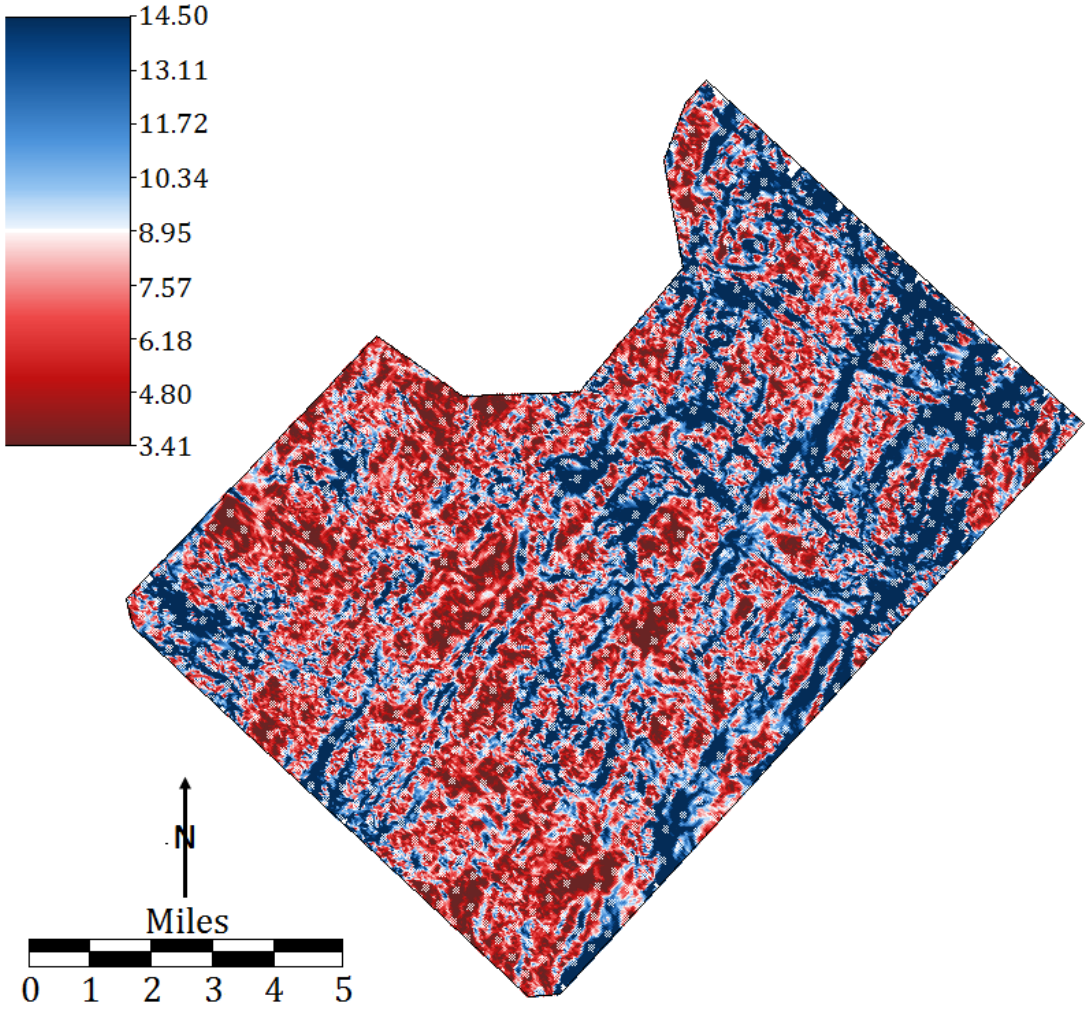

Figure 49: Results of the dip attribute calculation completed on the lower Marcellus horizon.

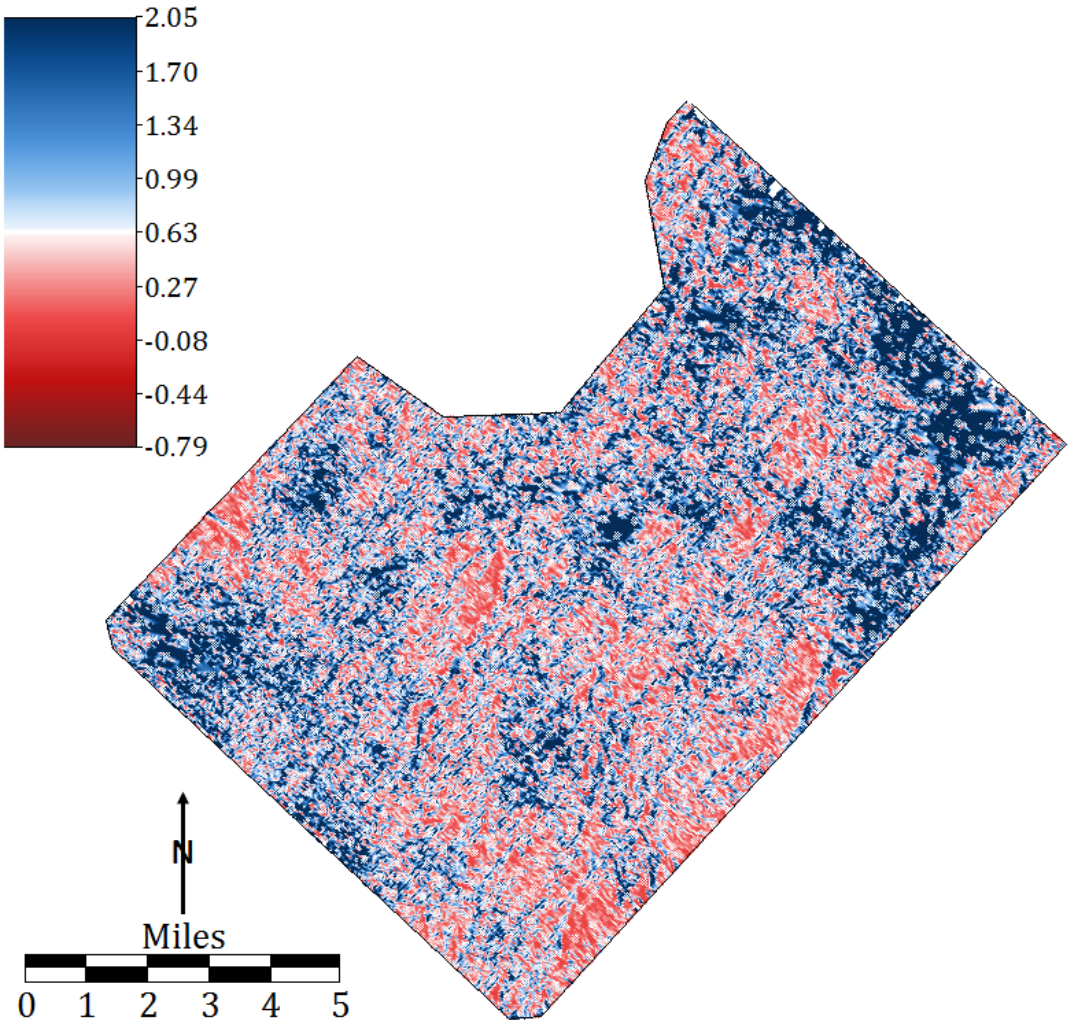

Figure 50: Results of the maximum curvature attribute calculation completed on the lower Marcellus horizon.

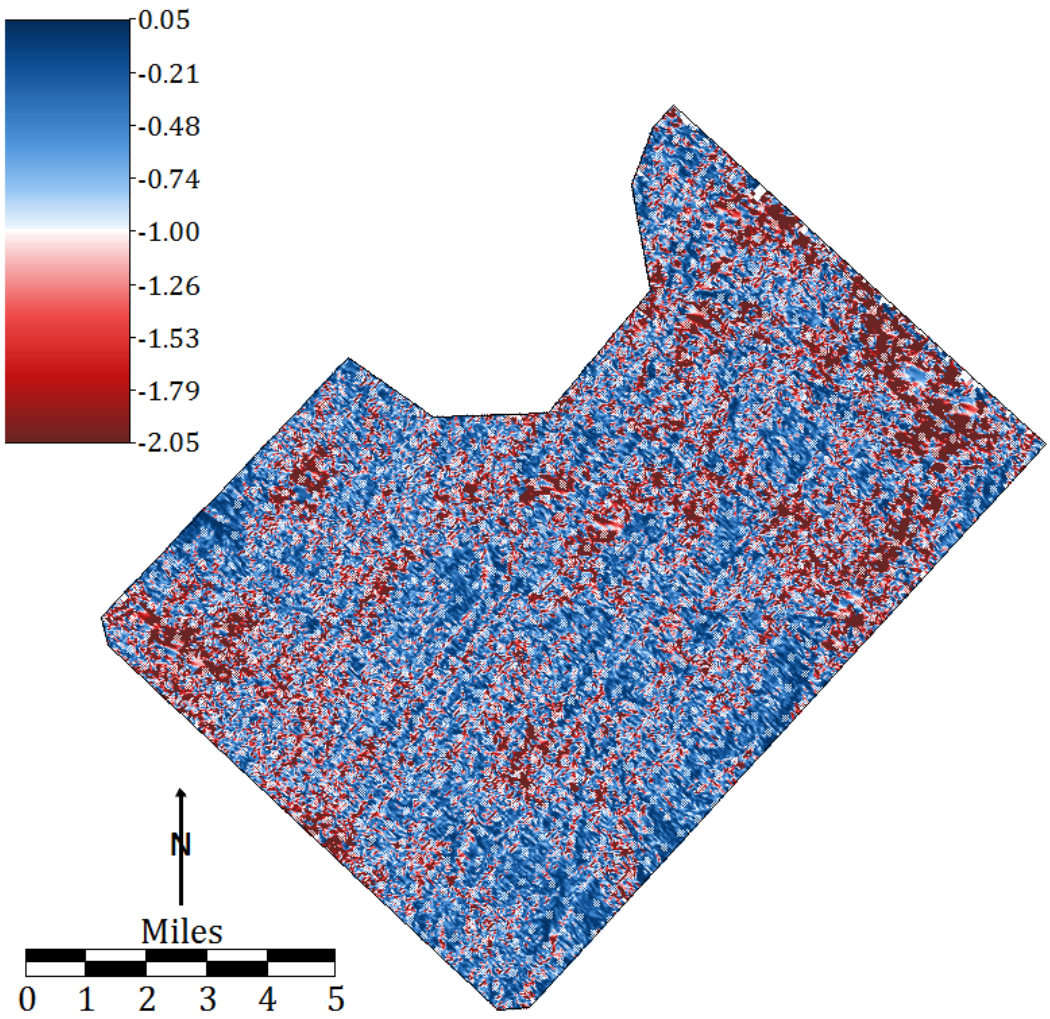

Figure 51: Results of the minimum curvature attribute calculation completed on the lower Marcellus horizon.

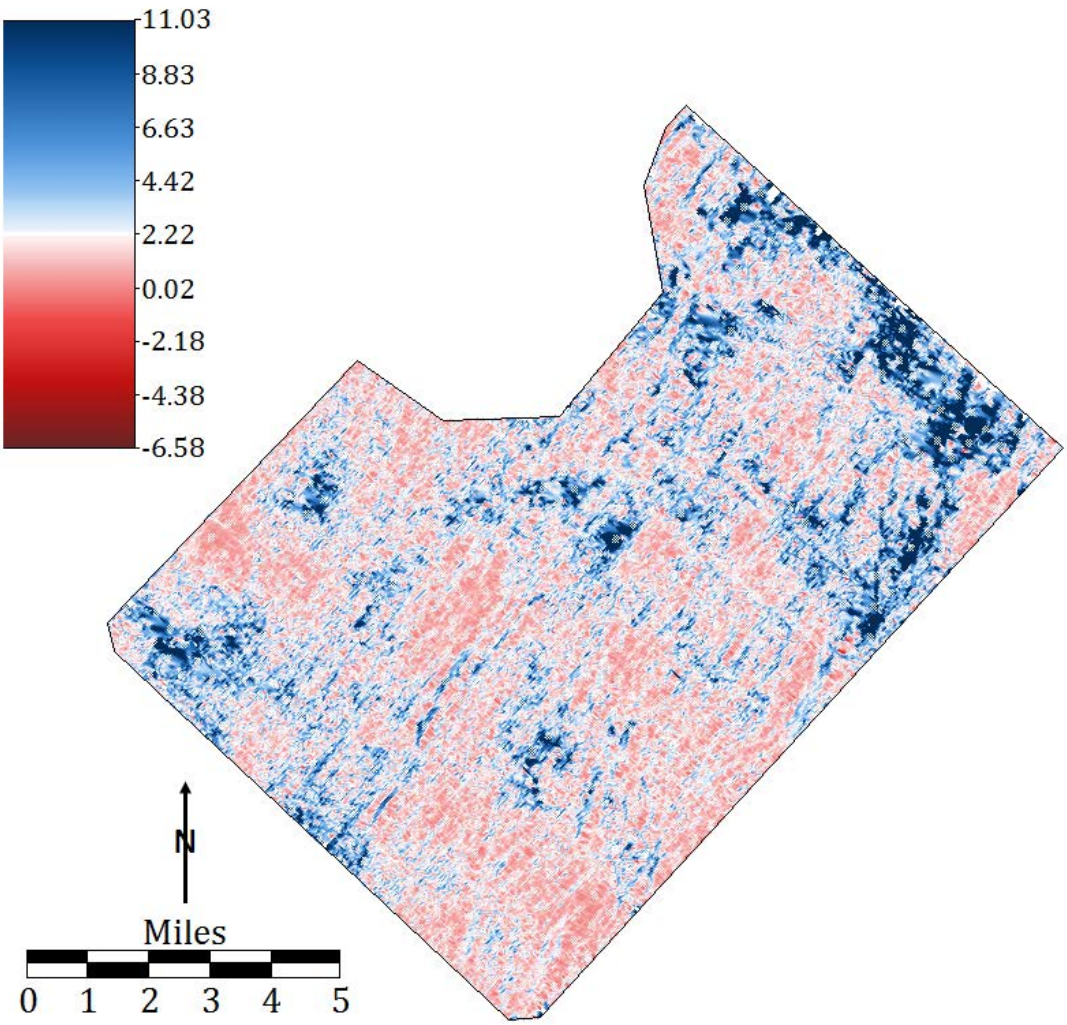

Figure 52: Results of the most positive attribute calculation completed on the lower Marcellus horizon.

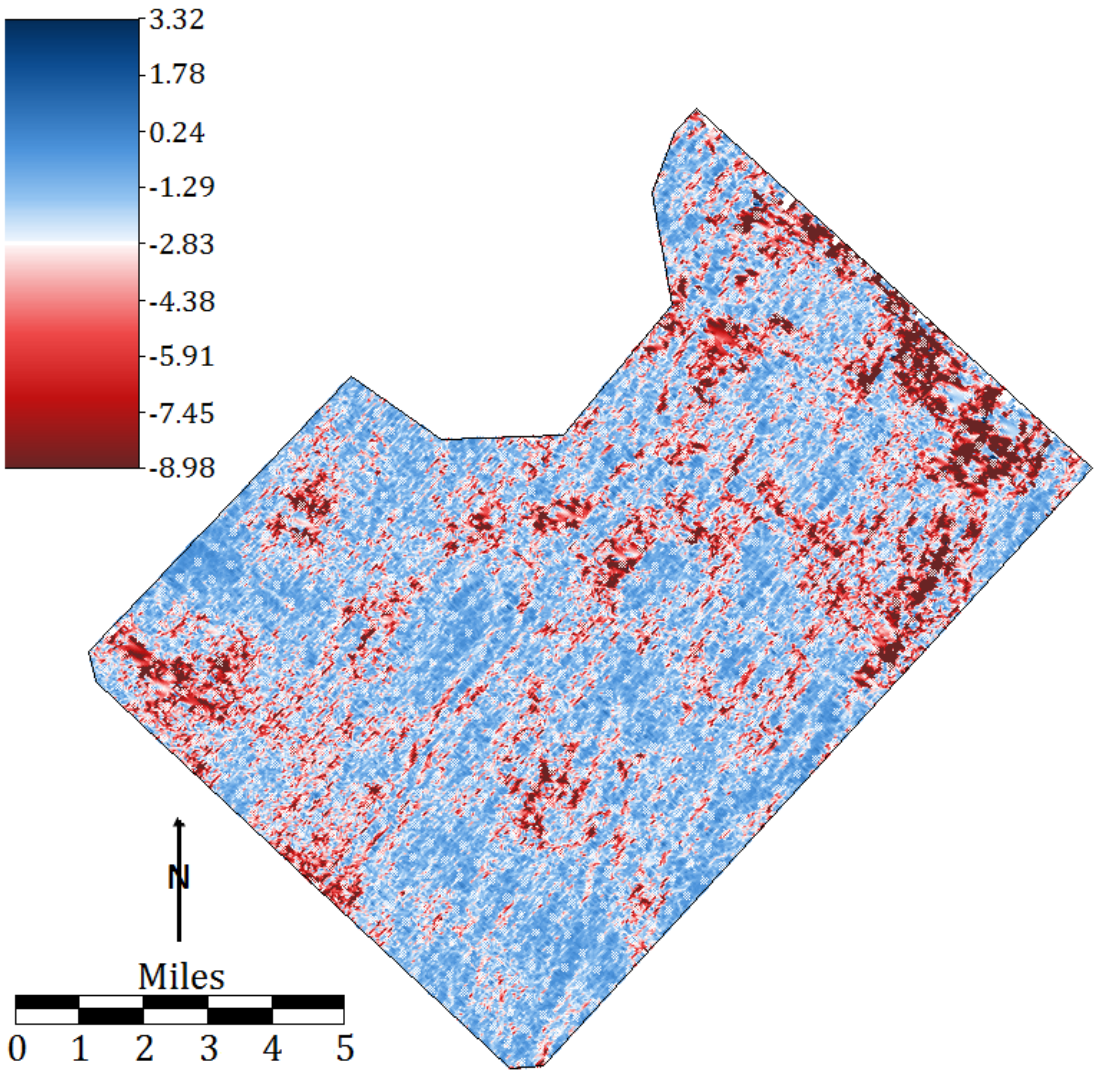

Figure 53: Results of the most negative attribute calculation completed on the lower Marcellus horizon.

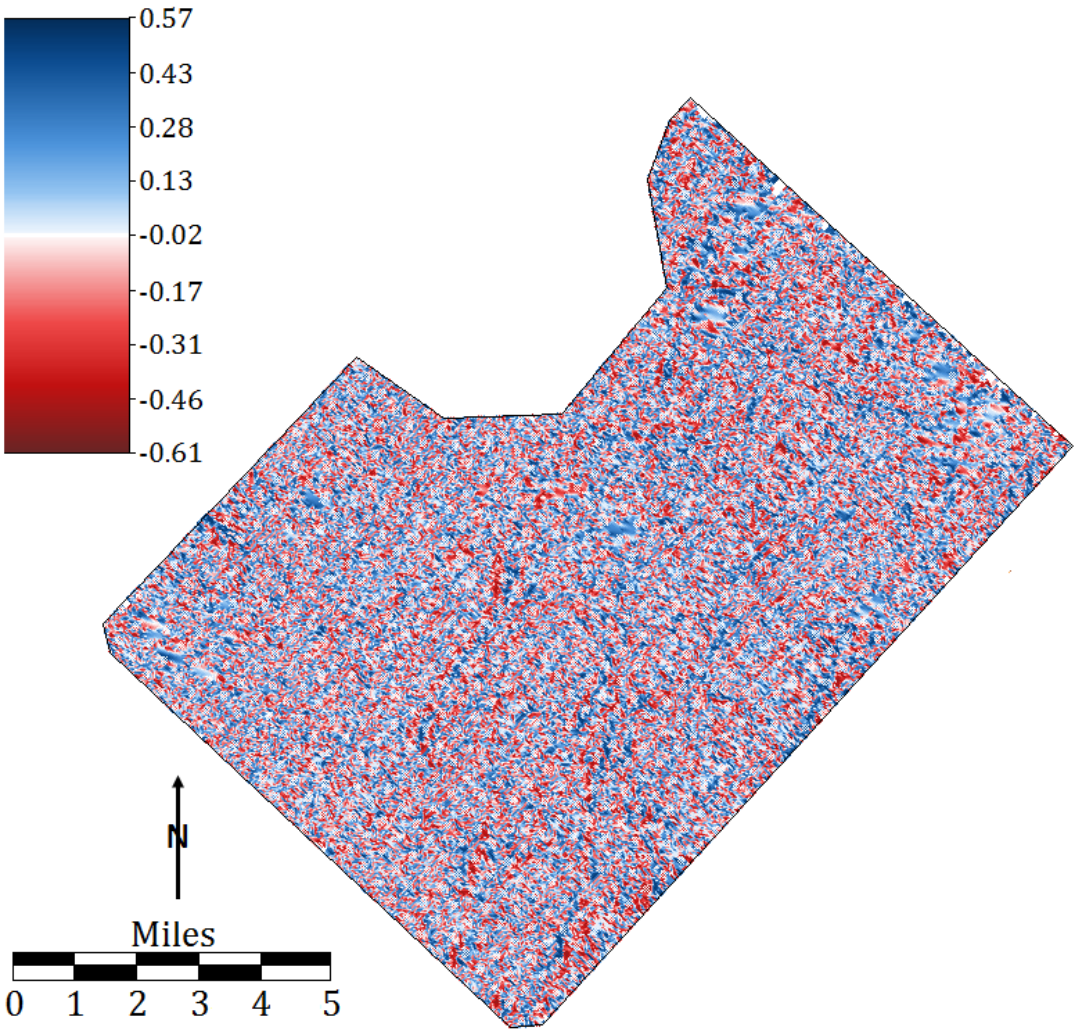

Figure 54: Results of the strike curvature attribute calculation completed on the lower Marcellus horizon.

11. Appendix E: Matlab code for generating rose diagrams from lineaments

```
close all; clc; clear;

% measures near the MWV wells
f1=[-110;-119;-101;-66;-136;-87;-123;-133;-130;-131;-104;-135;-148;-105;-
131;-100;-137;-137;-121];
% measures near PCSF wells
f2=[-128;-103;-137;-129;-109;-123;-131;-129;-139;-111;-76;-21;-111;-87;-38;-
31];
% Lower middle region
f3=[-131;-134;-106;-118;-110;-129;-101;-130;-131;-114;-75;-133;-106;-104;-
107;-95;-77;-119;-84];
% Central region
f4=[-117;-133;-99;-121;-126;-138;-127;-97;-117;-129;-131;-96;-105;-138;-133;-
154;-126;-114;-81];
% Northern corner
f5=[-116;-103;-114;-111;-105;-127;-29;-31;-95;-101;-106;-124;-117;-115;-88;-
89;-126;-124;-135];

[g,h]=size(f1);
for i=g+1:g+g
    f1(i,1)=f1(i-g,1)+180;
end

[g1,h1]=size(f2);
for i=g1+1:g1+g1
    f2(i,1)=f2(i-g1,1)+180;
end

[g2,h2]=size(f3);
for i=g2+1:g2+g2
    f3(i,1)=f3(i-g2,1)+180;
end

[g3,h3]=size(f4);
for i=g3+1:g3+g3
    f4(i,1)=f4(i-g3,1)+180;
end

[g4,h4]=size(f5);
for i=g4+1:g4+g4
    f5(i,1)=f5(i-g4,1)+180;
end

[m,n]=size(f1);
for i=1:m   % Convert region 1 angle measure to radians
    f1_v2(i,1)=(f1(i,1)*pi)/180;
end

[m1,n1]=size(f2);
for i=1:m1  % Convert region 2 angle measures to radians
    f2_v2(i,1)=(f2(i,1)*pi)/180;
```

```
end

[m2,n2]=size(f3);
for i=1:m2  % Convert region 3 angle measures to radians
    f3_v2(i,1)=(f3(i,1)*pi)/180;
end

[m3,n3]=size(f4);
for i=1:m3  % Convert region 4 angle measures to radians
    f4_v2(i,1)=(f4(i,1)*pi)/180;
end

[m4,n4]=size(f5);
for i=1:m4  % Convert region 5 angle measures to radians
    f5_v2(i,1)=(f5(i,1)*pi)/180;
end

% Create an angle plot of region 1
figure(1);
polarhistogram(f1_v2,45,'FaceColor','black');
pax=gca; rticklabels({}); pax.RLim=[-inf 7]; grid off;
pax.ThetaZeroLocation='top';
pax.ThetaDir='clockwise'

% Create an angle plot of region 2
figure(2);
polarhistogram(f2_v2,45,'FaceColor','black');
pax=gca; rticklabels({}); pax.RLim=[-inf 7]; grid off;
pax.ThetaZeroLocation='top';
pax.ThetaDir='clockwise'

% Create an angle plot of region 3
figure(3);
polarhistogram(f3_v2,45,'FaceColor','black');
pax=gca; rticklabels({}); pax.RLim=[-inf 7]; grid off;
pax.ThetaZeroLocation='top';
pax.ThetaDir='clockwise'

% Create an angle plot of region 4
figure(4);
polarhistogram(f4_v2,45,'FaceColor','black');
pax=gca; rticklabels({}); pax.RLim=[-inf 7]; grid off;
pax.ThetaZeroLocation='top';
pax.ThetaDir='clockwise'

% Create an angle plot of region 5
figure(5);
polarhistogram(f5_v2,45,'FaceColor','black');
pax=gca; rticklabels({}); pax.RLim=[-inf 7]; grid off;
pax.ThetaZeroLocation='top';
pax.ThetaDir='clockwise';
pax.RLim=[-inf 7];
grid off;
```

12. Appendix F: Matlab code for generating azimuthal anisotropy maps

```
close all;
clc; clear;

%% Define azimuth file

    azim='azim2.MIG.0.sgy' % Vfast Azimuth depth

% Read in the azimuth file using crewes readsgy.m
[trcd_azim,segyr2,sampint2,fmtcode2,txtfmt2,bytorder2,txthdr2,binhdr2,exthdr2
,...
    trchdr2,bindef2,trcdef2]=readsegy(azim,[],0,[],[],5,[],[],[],[],[]);

%% Read in trace coordinate data
locs=dlmread('azim_locs.txt');

%% plot the velocity field
% plots velocity vectors as arrows at location (x,y) with components (u,v)
% quiver(x,y,u,v)
v=trcd_azim(835,1:250:267120)';
x=locs(1:250:267120,6);
y=locs(1:250:267120,5);

i=1;
[j,k]=size(u);
u1=zeros(j,1);
v1=zeros(j,1);

% Convert all azimuths to positive angles
reg=zeros(j,1);
for i=1:j
    if v(i,1)<0
        reg(i,1)=360+v(i,1);
    else
        reg(i,1)=v(i,1);
    end
end

for i=1:j   % Convert from azimuth
    if reg(i,1)<= 90
        reg(i,1)=90-reg(i,1);
    elseif reg(i,1) > 90 && reg(i,1) <= 180
        reg(i,1)=360-(reg(i,1)-90);
    elseif reg(i,1) < 180 && reg(i,1) <= 270
        reg(i,1)=180+(90-reg(i,1));
    else
        reg(i,1)=(360-reg(i,1))+90;
    end
end


for i=1:j
```

```
    u3(i,1)=cosd(reg(i,1)); % Convert to Cartesian coordinates
    v3(i,1)=sind(reg(i,1));
end


figure(1)
quiver(x,y,u3,v3)
xlabel('Longitude')
ylabel('Latitude')
```

13. Appendix G: Matlab code for generating rose diagrams from Vfast azimuthal data

```
clc; clear;
close all;
%% Add needed files into the path
addpath('E:/Mountaineer_3D/20130305_Mountaineer_AZIM_PSDM Volumes')
addpath(genpath('E:/other'))    % for the files imported to seisware
addpath(genpath('E:/crewes'))   % Add the crewes MATLAB Toolbox

%% Prompt user for velocity file, and determine corresponding azimuth file
azim='azim2.MIG.0.sgy' % Azimuth depth

%% Read in the segy files using crewes readsgy.m
[trcd_azim,segyr2,sampint2,fmtcode2,txtfmt2,bytorder2,txthdr2,binhdr2,exthdr2
,...
    trchdr2,bindef2,trcdef2]=readsegy(azim,[],0,[],[],5,[],[],[],[],[]);
%% Read in the azimuth data and create an array with the azimuth values to
generate rose diagrams at selected locations in the study area within the
range of the Marcellus

step=9000;
% Import range of Marcellus, at every step value    (Samples in Marcellus,
selected locations)
m1=trcd_azim(206:1:343,1:step:267120);
[sz1,sz2]=size(m1); % find the size of the m1 array

% Create an array with the same location data space, but added space for
Marcellus data (samples in Marcellus x2, selected locations)
m3=zeros(sz1+sz1,sz2);

% Fill first part of empty m3 array with the values of m1 (samples in
marcellus x2, selected locations)
for i=1:sz1
    for j=1:sz2
        m3(i,j)=m1(i,j);
    end
end

% Fill the second half of empty m3 array with the opposite values of m1
(Samples in marcellusx2, selected locations)
for i=sz1+1:sz1+sz1
    for j=1:sz2
        m3(i,j)=m1(i-sz1,j)+180;
    end
end

[s1,s2]=size(m3);
m4=zeros(s1,s2);

for i=1:sz1+sz1
    for j=1:sz2
            m4(i,j)=(m3(i,j)*pi)/180;     % Convert to radians
    end
end
```

```
for i=1:s2
    figure(i);
    polarhistogram(m4(:,i),45,'FaceColor','black');
    pax=gca; pax.ThetaZeroLocation='top'; pax.ThetaDir='clockwise';
    pax.RLim=[-inf 100];grid off; rticklabels({});
    title([i]);
end

%% Read in coordinate data and plot locations of the generated rose diagrams
locs=dlmread('azim_locs.txt');
lat=locs(1:step:267120,5);
long=locs(1:step:267120,6);
figure(s2+1);
scatter(long,lat,'black');
xlabel('Longitude');ylabel('Latitude');
```

SIGNATURE PAGE

This is to certify that the thesis prepared by Megan Valdez entitled Fault mapping in 3D seismic reflection data using seismic attributes and velocity: example from West Virginia has been examined and approved for acceptance by the Department of Geophysical Engineering, Montana Technological University, on this 12th day of April 2019.

Marvin Speece, PhD, Professor and Department Head
Department of Geophysical Engineering
Chair, Examination Committee

Xiaobing Zhou, PhD, Professor
Department of Geophysical Engineering
Member, Examination Committee

Scott Rosenthal, P.E., Associate Professor and Department Head
Department of Mining Engineering
Member, Examination Committee